Feasibility Study and Design of Soft-Catcher for Damaged Concrete Debris

Ву

Kwee Siang ONG

in partial fulfilment of the requirements for the degree of

Master of Science

in Civil Engineering

at the Delft University of Technology, to be defended publicly on September 27, 2017 at 10:45 AM.

Chairman: Prof. Dr. Ir. L.J. Sluys

Thesis committee: Dr. Ir. J. Weerheijm, TU Delft

Ir. L.J.M. Houben, TU Delft

Ir. M. Bakker, TNO

This thesis is confidential and cannot be made public until September 27, 2017.

An electronic version of this thesis is available at http://repository.tudelft.nl/.



Preface

This report is written and compiled in fulfilment of obtaining 40 ECs under CIE5060-09 MSc Thesis Project. The research work was entirely carried out under the supervision of Structural Mechanics Section in Faculty of Civil Engineering and Geosciences at Delft University of Technology.

The research topic was proposed as part of the overall efforts to bridge the knowledge gaps in predicting explosive effects arising from an internal explosion of ammunition magazine. This is of particular interest to me as my previous work experiences largely involve areas of protective structures design. My involvement in this thesis work, which mainly focuses on impact mechanics and penetration problems, will eventually enhance my technical knowledge and competencies.

I will like to express my sincere gratitude to the members of my thesis assessment committee, Prof. Dr. Ir. L.J Sluys (TU Delft), Dr. Ir. J. Weerheijm (TU Delft/TNO), Ir. L.J.M. Houben (TU Delft) and Ir. M. Bakker (TNO) for their meticulous efforts and valuable advices in guiding me during the course of the research.

Kwee Siang ONG

Delft, September 2017



Contents

Preface		2
Contents.		3
Abstract .		6
1. Intro	oduction	7
1.1	Layout of Report	8
2. Rese	earch Aim and Methodology	9
3. Liter	rature Review	12
3.1	Soft-Catcher Materials	12
3.2	Penetration of Debris into Cellular Materials	13
3.3	Rankine-Hugoniot Relationship	14
3.4	Shock Wave Models	17
3.4.1	Rigid-Perfectly Plastic- Locking (R-P-P-L) Model	17
3.4.2	2 Elastic-Perfectly Plastic-Rigid (E-P-P-R) Model	19
3.4.3	Power Law Shock Model	21
3.4.4	Rigid-Power Law Hardening (R-PLH) Model	23
4. Mod	lified R-PLH Model	30
4.1	Shape Coefficients, Frictional Resistance and Initial Elasticity	30
4.2	Proposed Modifications to R-PLH Model	32
4.3	Analytical Predictions	39
4.3.1	Impact Scenario of Large Wall Debris	40
4.3.2	2 Predictions based on R-PLH Model	41
4.3.3	Predictions based on Modified R-PLH Model	46
4.3.4	4 Concluding Remarks	50

5	Numer	rical Simulation	52
	5.1 Va	alidations of Material Models	52
	5.1.1	MAT_63: CRUSHABLE FOAM	53
	5.1.2	MAT_18: POWER LAW PLASTICITY	58
	5.1.3	Concluding Remarks	59
	5.2 Nu	ımerical Modelling	60
	5.2.1	General Modelling Information	60
	5.2.2	Formulation of Contact Type	61
	5.3 Me	odel of 20m Target Length – Validations of 1D Analytical Models	62
	5.3.1	Velocity-Time History of Impactor	63
	5.3.2	Effective Stress-Time History of Target	65
	5.3.3	Volumetric Strain-Time History of Target	69
	5.3.4	Plastic Shock Wave Propagation	72
	5.3.5	Effects of Different Impact Velocities	76
	5.3.6	Concluding Remarks	82
	5.4 1D	Numerical Model of 2 m Target Length - Design of Soft-Catcher	83
	5.4.1	Velocity-Time History of Impactor	83
	5.4.2	Effective Stress-Time History of Target	84
	5.4.3	Volumetric Strain-Time History of Target	85
	5.4.4	Plastic Shock Wave Propagation	86
	5.4.5	Impact Velocities of 50m/s and 100m/s	87
	5.4.6	Debris Damage Level vs Target's Impact Resistance	88
	5.4.7	Penetration Distance of Debris	89
	5.4.8	End Boundary Support Reaction	92
	5.4.9	Further Mesh Sensitivity Study	93

	5.4.10	Concluding Remarks	96
	5.5 2D	Numerical Model of Soft-Catcher	97
	5.5.1	2D Model – With Tensile and Shear Resistances	97
	5.5.1.1	Tie-Break Contacts	100
	5.5.1.2	Velocity-Time History of Wall Debris	101
	5.5.1.3	Material Stresses of Soft-Catcher	102
	5.5.1.4	Material Strains of Soft-Catcher	108
	5.5.1.5	Support Reactions at Boundaries	111
	5.5.2	Sensitivity Study of Shear and Tensile Failure Stress	113
	5.5.3	Concluding Remarks	116
	5.6 De	sign Consideration for Soft-catcher	117
6	Conclu	sion and Recommendation	121
B	ibliograph	y	125

Abstract

The main thrust to initiate this research work emerges from the need to enhance prediction capabilities in explosive safety of ammunition magazine. The Klotz Group (KG), a committee that comprises international subject matter experts on explosive safety, has strong interest in investigating debris throw hazard arising from internal explosion of ammunition magazine structure. Debris launch information, such as mass distribution, is vital for hazard assessment and to calibrate numerical models that simulate concrete structure breakup. The current technique to collect explosively-damaged debris after test execution does not yield representative test data on the launch condition. Thus, this research work explores the use of structural polymeric foam, Rohacell 110WF, as the benchmark material to effectively soft-catch concrete debris at close distance from the test structure. Ensuring no additional damage to debris during the soft-catching process and ability to terminate the debris motion within stipulated distance are two principal considerations in this research study.

Various one-dimensional (1D) shock wave models that analytically predict crushing responses of cellular material are briefly reviewed. From which one particular approach, known as rigid-power law hardening (R-PLH) model has been selected. Modifications to the existing R-PLH model are then proposed to incorporate effects of nose shape geometry of debris, frictional resistance and initial elasticity. Analytical predictions of a representative impactor-target scenario, using both R-PLH Model and Modified R-PLH Model, are performed with various impact velocities. In general, Modified R-PLH Model exhibits reductions in shock-induced stresses and strains, as compared to R-PLH Model. This is primarily due to decrease in particle velocity jump across shock wave front as the Modified R-PLH Model considers non-zero particle velocity in the uncrushed region. Consequently, the Modified R-PLH Model predicts slower deceleration of debris motion. The Modified R-PLH Model eventually establishes the preliminary design length of the soft-catcher.

High-fidelity modelling and simulation tool, LS-DYNA, is utilised to perform numerical analyses. Two different debris velocity time response regimes that relate to plastic and elastic wave propagations are identified in the debris velocity-time history curves. 1D numerical analyses with 20m target length have well-validated the Modified R-PLH Model. Good agreement of debris velocities, shock-induced stresses and strains are observed within the higher velocity time response regime. Subsequently, the 1D numerical model are redeveloped using desired soft-catcher length of 2m to compare and highlight the implications of rigid backing at boundary end. Following then, numerical models are created in two-dimensional (2D) space domain, to study on how the tensile and shear failure stresses of soft-catcher can influence the debris penetration phenomenon. Key differences in various material responses between the 2D and 1D model are brought into attention. In addition, sensitivity studies on increasing the shear and tensile resistances are carried out. Lastly, charts are plotted to facilitate design of soft-catcher with different debris launch velocities.

1. Introduction

Ammunition storage magazines are always subjected to a potential risk of accidental explosion, in which effects can be devastating to the surrounding environment. In the event of such confined explosion within a reinforced concrete magazine, the main causes of human lethality are primarily due to blast pressure and debris (e.g. concrete, reinforcement and primary ammunition fragments) throws. Other explosive effects of internal explosion that include fireball, radiation and ground shock are usually of less significance. In situation where explosive charge weight is low, the main contribution to human injuries and fatalities is debris throw, as the breakup of structural walls and roof will likely to attenuate most of the blast pressure. This phenomenon is reversed when the charge weight is high.

Mitigation against explosive effects such as air-blast and debris throw hazards arising from accidental explosion of ammunition storage facility has always been a key focus in research development of explosive safety. The study of shock wave propagation and its consequential effects on human in an open field environment are relatively well-established phenomenon with current state of art technology. These effects can be reasonably predicted with advanced numerical simulation tools and existing reference charts. Conversely, the development of numerical capabilities to accurately predict debris throw can be further enhanced. During 2007 and 2008, TNO Defence, Security and Safety and Fraunhofer Ernst-Mach-Institute (EMI) had jointly developed the Klotz Group (KG) Software, which is based on KG Engineering Tool (Van Doormaal, 2006) and the source function theorem formulation of the debris distribution [1]. This semi-empirical software tool calculates debris distances from potential explosive site and predicts the energy of the individual debris along its ballistic path which will be useful for risk analysis in an accidental explosion of ammunition storage magazine. In recent years, additional features to account for the effect of sloped terrain, barricades, debris cloud (on small debris), modelling of surrounding buildings and generating the number of hits have been incorporated to improve its prediction capability. Nevertheless, there are some limitations present in the software which include the inabilities to predict the breakup of structures and model the debris bounce and breakup upon impact with ground. This drives the direction of this Master thesis research proposal.

To illustrate the knowledge gap in a more holistic perspective and appreciate how the proposed research can benefit future research development, it is essential to look into the entire debris throw event arising from the initial breakup of concrete components to the final at-ground resting condition. This process can be simplified into five stages as shown in Figure 1-1 [2], namely (a) internal blast loading, (b) structural response and breakup, (c) debris launch, (d) debris trajectory and (e) post ground impact.

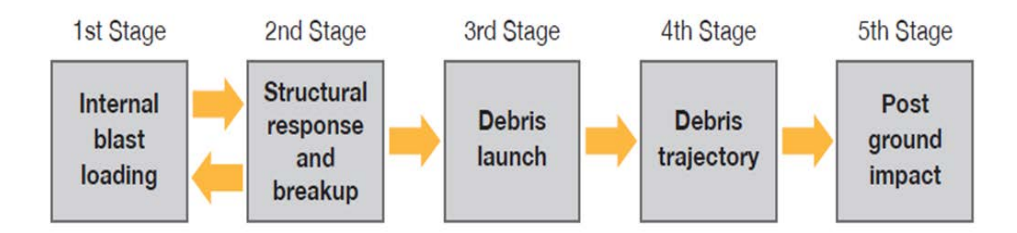


Figure 1-1: Five stages of debris development process

For the 1st Stage, advanced numerical tools are available to model and predict internal blast loading and blast-structure interaction, which can be validated by explosive test results. In the 2nd Stage, the breakup phenomenon of concrete structure subjected to internal blast loading can also be modelled and simulated by numerical tools. Debris launch information such as launch velocities and launch angles can all be generated by the numerical simulation, but details of the break-up process resulting in the debris mass distribution cannot be predicted accurately yet. The size of debris generated by the numerical simulation will depend e.g. on the applied material model, the computational technique and the sizes of element mesh used to model the structure. Therefore, in order to achieve high fidelity for the numerical prediction of the debris breakup and throw process, representative test data will need to be collected and used to calibrate the numerical model. The debris collected from the usual approach of post-test retrieval from the ground (at-resting condition) will not be representative to calibrate numerical models for initial break-up and launch condition. The explosively-damaged debris with different residual strength may subject to further breakup into smaller masses during its ballistic path due to collision of other debris, air resistances, and especially due to impact with ground surface. Trajectory of debris under 4th Stage can subsequently be evaluated with various aerodynamic coefficients, using the debris launch information obtained from the numerical simulation in 3rd Stage. Post ground impact at 5th Stage generally refers to the situation where explosively-damaged concrete debris (with residual strength) are subjected to further breakup and ricochet upon impact with the ground. Since 2012, Protective Technology Research Centre in NTU (Singapore) has been conducting series of debris-shooting tests to characterize the breakup phenomenon of debris upon ground impacts. However, the regularly shaped concrete specimens used in these tests were subjected to statically-induced damage. This was to account for strength reduction of debris due to initial breakup by blast pressure. However, this may not provide accurate findings of the breakup phenomenon, as compared to actual explosively-damaged concrete debris that are of irregular shapes and sizes. And so, the information in regards to shapes and size distribution of actual explosively-damaged concrete debris will be valuable in calibrating initial launch conditions of debris obtained from numerical analysis. Furthermore, this explosivelydamaged concrete debris will also provide accurate test specimens for the debris-shooting tests to obtain more meaningful observations on the post ground impact.

1.1 Layout of Report

The structures of this thesis report are as follows; Chapter 2 illustrates the research methodology and work-flow leading to the final deliverable. Chapter 3 briefly reviews the important mechanical properties for the material selected as the soft-catcher. It also discusses related researchers' work on impact mechanics and shock-wave theories related to cellular materials. Chapter 4 proposed modifications to an existing analytical model in order to include effects from material elastic properties and the nose geometry of debris. To validate the modified analytical model, 1D numerical modelling and analyses were performed and discussed in Chapter 5. This chapter extends the numerical analysis into a 2D space domain to highlight the noticeable differences in material responses, as compared to 1D analytical and numerical models. Sensitivity studies of shear and tensile resistances within the soft-catcher to influence the penetration phenomenon are also performed. Finally, Chapter 6 concludes the entire research work and recommends possible areas of focus for future efforts in this research domain.

2. Research Aim and Methodology

In order to physically collect explosively-damaged concrete debris and obtain its initial launch information (i.e. mass distribution, shape, velocities) upon the initial breakup phenomenon, the proposed research work shall aim to perform feasibility studies of interaction between concrete debris and soft-catcher system, based on an appropriate material selected for the design of the debris-soft catcher system. The execution of the explosive trials will not be part of this Master thesis work, in view of the short time frame allowed to complete this research work. Nevertheless, the experimental results obtained from the explosive trials shall eventually provide the following:

- (1) Test data to calibrate numerical models in simulating concrete's initial breakup process.
- (2) Test specimens for debris-shooting tests to characterize post ground impact phenomenon.

The following Figure 2-1 illustrates how the experimental test data can be beneficial to the research development in debris throw process.

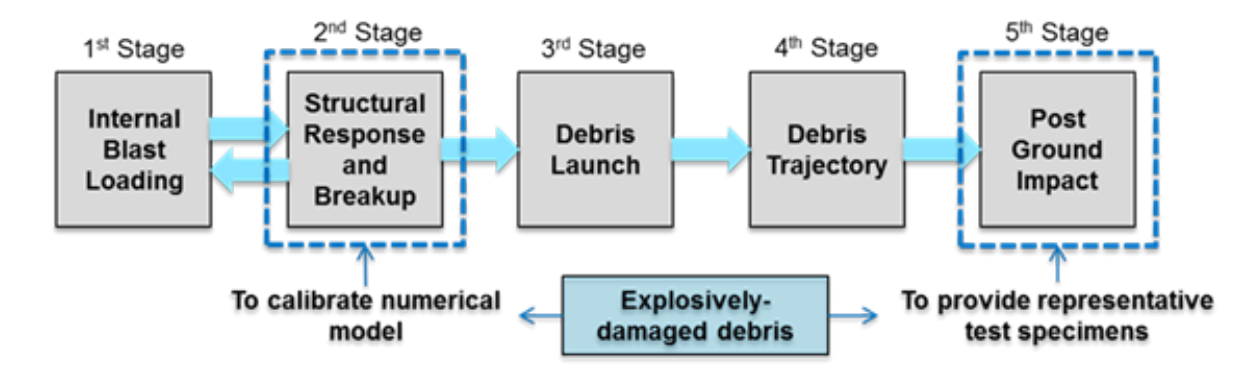


Figure 2-1: Contribution of research to current knowledge gap

Getting information such as debris launch velocity, sizes and damage level is a prerequisite before exploring feasible soft-catch solutions. KG has previously conducted explosive trials to study the breakup of KASUN structure; an above-ground ammunition storage magazine. The KASUN, which is considered as the reference structure in this research study, has an internal cubicle dimension of 2 m by 2 m by 2 m, with wall and roof thickness of 0.15 m. In 2005, a series of clamped reinforced concrete slab tests were carried out in Ballistic Laboratory of TNO to study the breakup of one-way slabs under explosive loading [3]. A steel-composite explosion box was used to clamp the slab specimens, as illustrated in Figure 2-2. The loading densities tested range from 0.5 kg/m³ to 4 kg/m³. As it is deem viable to reuse the explosion box for the future soft-catcher test, the dimension of this explosion box is taken into consideration when sizing up the soft-catcher.

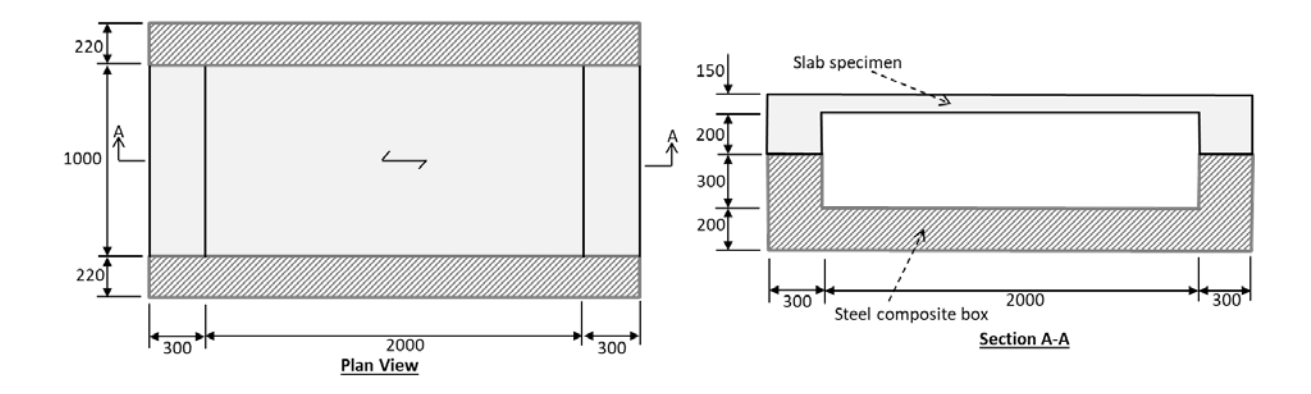


Figure 2-2: Plan and section view of clamp RC slab test setup [3]

This research primarily focuses on the study of physics of the interaction between the explosively-damaged concrete debris and the response of the debris-catcher system. It is of importance to obtain reliable predictions of the soft-catcher system response, such that the aim of ensuring no additional damage of debris can be achieved. Therefore, the ability to determine impact resistance acting upon the concrete debris and the final penetration distance of debris will be crucial. Specific research questions that are addressed include:

- What is the design length of soft-catcher?
- What are the impact stresses on the debris compared with the design strength of applied concrete and residual strength of damaged debris?
- What are the magnitudes of reaction forces at boundary supports of soft-catcher?

The main scopes of the research works include reviewing the mechanical properties of the selected materials and its related impact mechanics theories. This is then followed by discussing existing one-dimensional analytical models that predict shock-induced material responses. Subsequent efforts will then be focused on improving prediction accuracies of the existing analytical model. Numerical modelling and simulation using high-fidelity finite element algorithm will be performed to validate these analytical model predictions, before moving on into two-dimensional numerical analyses. Relevant outputs will be consolidated for future detailed design of soft-catcher system. The various tasks leading to the completion of research work are illustrated in Figure 2-3:

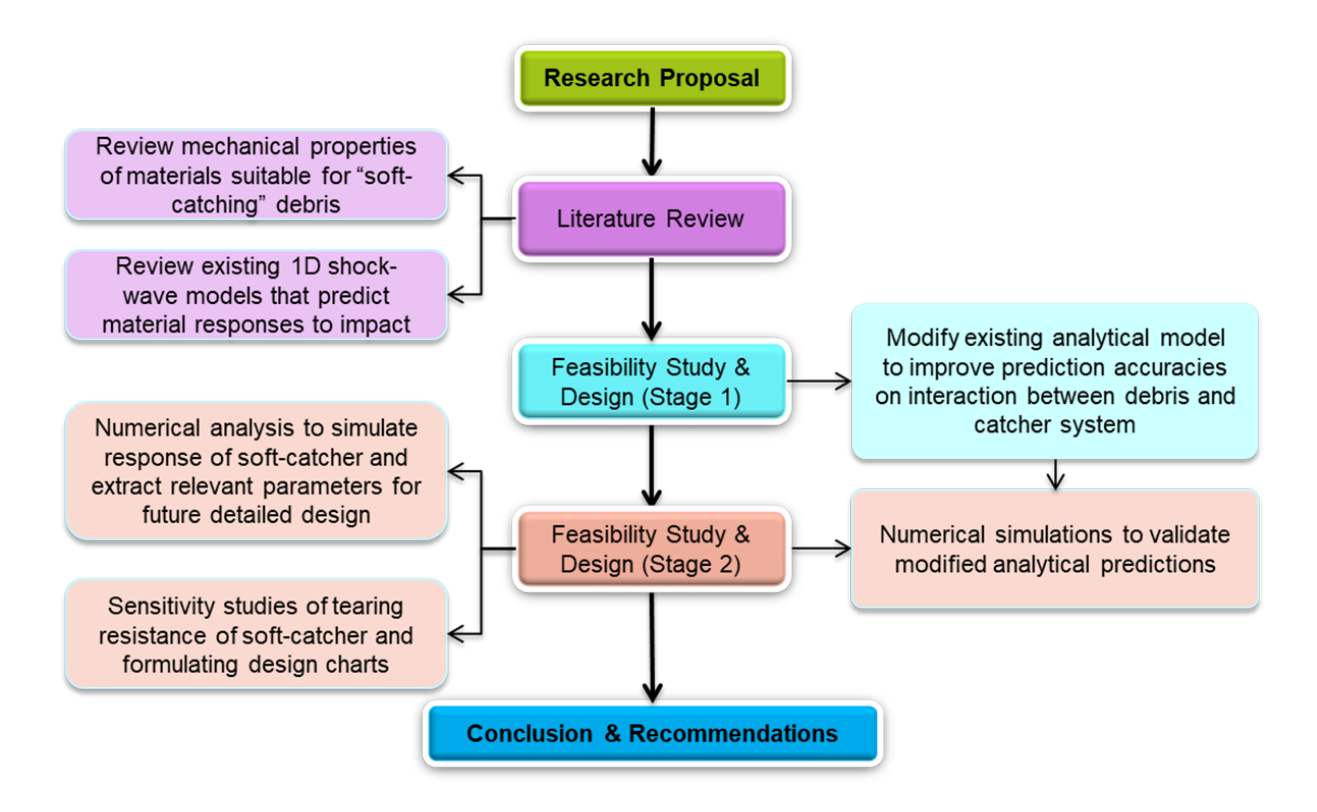


Figure 2-3: Work flow diagram for the proposed research

3. Literature Review

3.1 Soft-Catcher Materials

The type of material to be considered for the soft-catcher must fulfil two main features; to allow penetration of debris without inducing additional damages to the debris, and to effectively decelerate and stop the debris within a pre-defined distance (e.g. thickness of the soft-catcher system). Considering that the kinetic energy from the debris is the highest when moving at initial impact velocity, it is essential for the soft-catcher to indent and tear apart easily at the first instance of impact with the debris and allow penetration. The penetration resistance from the soft-catcher must not be greater than the residual strength of the explosively-damaged debris, in order to avoid further disintegration of debris during the penetration process. It is also necessary to avoid perforation of the soft-catcher, which may subject debris to further disintegration due to impact with ground.

Cellular solid materials such as polymeric foams are commonly used as impact energy absorbers in various engineering application, in which its crushing resistance is a key design parameter to consider. The typical quasi-static compressive stress-strain curve of a cellular material can be simplified into three distinct regimes; linear elasticity stage, plateau stress stage and densification stage.

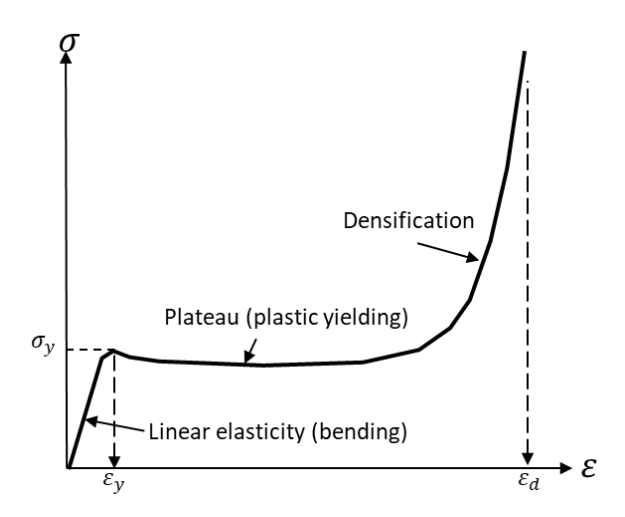


Figure 3-1- Typical compressive stress-strain curve for elasto-plastic foam

The elastic limit, also referring to the onset of plateau regime, usually occurs at low strain (i.e. crush strain ε_y) and stress (crush stress σ_y) values. The plateau stress regime indicates the initiation of cell walls collapse as the new deformation mechanism, before ending at critical strain ε_{cd} . This critical strain ε_{cd} implies the onset of densification. The densification regime, which occurs when collapsed cell walls get in contact with one another, results in steep increases in stress value with marginal increase in compressive strain. The complete densification strain ε_d corresponds to the state when the cellular material is completely compacted. Empirical data has shown that the complete densification strain ε_D can be expressed in the following equation according to [4]. ρ^* refers to initial foam density while ρ_s refers to the density of the constituent material. One may expect that the limiting strain for

densification shall equate to the porosity of the foam $\left(1 - \frac{\rho^*}{\rho_s}\right)$. However, in reality, extensive experiments had evidently shown that the limiting strain is in fact lower.

$$\varepsilon_D = 1 + 1.4 \left(\frac{\rho^*}{\rho_s} \right) \tag{3.1}$$

Polymeric foams with elastoplastic stress-strain behaviour have several characteristics that are aligned reasonably well with the soft-catcher's performance criteria. These include; a low yield stress and strain which allows ease of penetration at first instance of impact with debris, high crushability to decelerate debris during penetration and the long, relatively stable plateau stress characteristic that allow large deformation at almost constant stress provides good energy absorption. Because of these material characteristics, these types of foams will be considered as the soft-catcher for the feasibility study.

3.2 Penetration of Debris into Cellular Materials

Considering debris as a rigid body, impacting at normal direction to the cellular material and assuming no instability of this cellular material during the impact process, the motion of the debris with crushing of the cellular material can be governed by the Newton's second law as follows;

$$M\frac{dv}{dt} = -F_R \tag{3.2}$$

Where M is the mass of the debris and F_R is the overall resistance force of the cellular material in the axial direction of the debris motion. Note that the above equation is of the same form as compared to the Poncelet Equation for rigid-body penetration problem. The resistance force F_R to debris penetration generally comprises the plastic crushing force of the cellular material, dynamic force (i.e. due to shock enhancement), tearing force (i.e. tensile and shearing fractures during penetration in cellular material) and the frictional force between the debris and the cellular material.

Extensive research works had concluded that stress enhancement and localization of cell crushing in the region between the impactor (i.e. debris) and the shock wave front are two prominent characteristics of shock compression in cellular solids [5] [6] [7]. When the impact velocity is high enough, plastic shock wave front will be induced by the impact to propagate ahead of the debris. The shock wave front refers to the planar interface separating crushed and uncrushed cells under dynamic compression. In this respect, the debris-penetration problem will assume that the shock wave is propagating at a subsonic speed (i.e. velocity of wave front lower than the linear sound velocity of stress wave in the material). This implies that an elastic precursor wave will propagate ahead of the plastic shock wave, at the speed of the linear sound velocity. The linear sound velocity of stress wave for typical foam materials is in the range of about 600-800 m/s [8].

Various researchers investigated and modelled shock wave propagation in cellular material mainly in three approaches; shock wave model, mass-spring model and finite element simulation. In this feasibility study, relevant one-dimensional shock wave models are examined to evaluate stress enhancement of cellular material. Reid and Peng [5] first

proposed a one-dimensional shock wave model to predict the crushing strength enhancement in wood specimens, under the assumption of rigid-perfectly plastic-locking (R-P-P-L) idealization for the material's stress-strain response. This model retained the two main features of the stress-strain curve of wood, namely; crushing stress and a locking strain. The locking strain in this model is more often referred as the complete densification strain. Realizing that the initial elastic property of cellular material may influence its response, Lopatnikov et al. [9] had employed similar shock wave theory to develop an elastic-perfectly plastic-rigid (E-P-P-R) model to investigate deformation of aluminum foams under projectile and target tests. This E-P-P-R model considered three parameters that include the elastic modulus, plateau stress and the maximum strain limit as the locking strain. Zheng et al. [10] subsequently used a rigid-linear hardening plastic-locking (R-LHP-L) idealization to account for the effect of hardening at plateau regime. A Shock-Mode model for high velocity impact and a Transitional-Mode model for a moderate velocity impact were developed. The R-LHP-L model uses three parameters; yielding stress, plastic hardening modulus and the locking strain. Note that the material models discussed thus far had assumed a single but different strain value as the locking strain to represent the densification regime.

Most of the cellular materials exhibit strain hardening during densification regime. Therefore, the use of locking strain for densification regime will not provide accurate predictions of stress changes at shock wave front. This is especially so when the stress changes can be sensitive to the particle velocity and strain jumps at the shock wave front [11]. Indeed, Zheng et al. [10] discovered that an increase of impact velocity will result a corresponding increase in densification strain in honeycombs. Harrigan et al. [12] used an elastic-perfectly plastichardening (E-P-P-H) idealization to account for both initial elasticity and strain hardening beyond onset of densification. However, his approach was not able to generalize into a closed-form solution. The use of power-law equation to describe the hardening regime, in replacement of the locking strain assumption in the R-P-P-L idealization was proposed by Pattofatto et al. [11]. His approach evaluates shock strains and stresses in the crushing region based on constant impact velocity scenario, which implies that the shock strain and stress are not time-dependent. Zheng et al. [13] then proposed a rigid-power law hardening (R-PLH) idealization to improve prediction accuracy. Closed form or semi-closed form general solutions of the physical quantities across the wave front were derived with three main parameters involved; yield stress, strength index and strain hardening index.

The subsequent sections highlight the analytical computations from some of these shock wave models and propose modifications to existing R-PLH model, in the interest of providing more accurate predictions for the debris penetration problem.

3.3 Rankine-Hugoniot Relationship

Consider the following schematic illustration of the shock wave propagating through a onedimensional cellular material as shown in Figure 3-2.

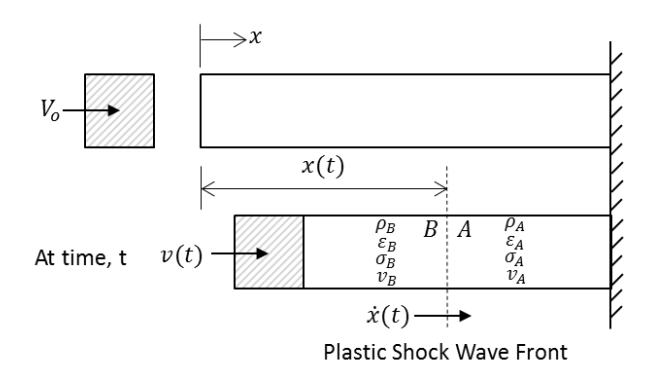


Figure 3-2- Shock wave propagation in one-dimensional cellular material

As mentioned in the earlier section, the velocity regime considered in the debris penetration problem is such that an elastic precursor wave will propagate ahead of the plastic shock wave. The presence of the elastic wave suggests that there will be a pre-stressed zone (i.e. region A) before significant jump in density. The plastic shock wave propagation results in crushing of material in region B. As such, there are discontinuities in physical quantities of the cellular material across the shock wave front, which obeys the Rankine-Hugoniot relationship. As identified in Figure 3-2, these physical quantities refer to the material density, strain, stress and particle velocity. For the above schematic diagram of the impact scenario, the jump of physical quantities can be defined by the following relation, where Q refers to various physical quantities.

$$[Q] = Q_B - Q_A \tag{3.3}$$

This generalized equation will primarily be considered for different idealization models as discussed subsequently. The theory described herein is based on steady state wave propagation, in which changes in material properties due to shock jump conditions are time-independent. This means that the jump conditions are derived on assumption that the projectile penetration and shock wave front propagation are at steady state condition.

Based on a Lagrangian frame, the Rankine-Hugoniot jump conditions can be derived using mass and momentum laws across the shock front. v_s refers to the absolute velocity of shock wave front, while \dot{x} refers to the velocity of wave front relative to the particle velocity, v_A ahead of the wave front. v_B refers to the particle velocity in the post-shock region. The mass conservation across the wave front is shown as follows.

$$\rho_B(v_S - v_B) = \rho_A(v_S - v_A) \tag{3.4}$$

Expand the expression and re-write to obtain the velocity jump [v],

$$\rho_B v_S + \rho_A v_A - \rho_A v_S - \rho_B v_A = \rho_B v_B - \rho_B v_A$$

$$\rho_B (v_B - v_A) = (v_S - v_A)(\rho_B - \rho_A)$$

$$(v_B - v_A) = \frac{(v_S - v_A)(\rho_B - \rho_A)}{\rho_B}$$

$$(v_B - v_A) = (v_S - v_A) \left(1 - \frac{\rho_A}{\rho_B} \right)$$
$$[v] = \dot{x} \left(1 - \frac{\rho_A}{\rho_B} \right) \tag{3.5}$$

Because it is assumed that the cross-sectional area of the material remain constant during crushing process, the relation between material local strain and corresponding density can be defined as follows, where ρ_o refers to the initial density and ρ_i refers to the current density:

$$\rho_i = \frac{\rho_o}{1 - \varepsilon_i} \tag{3.6}$$

Considering the case when the crushing strain (i.e. elastic limit strain) is typically small value for cellular material, the current density in region A affected by the precursor elastic wave can be approximately equal to the initial density (i.e. $\rho_A \approx \rho_o$). Therefore, the jump in material strain $[\varepsilon]$ can be expressed in terms of density:

$$[\varepsilon] = \varepsilon_B - \varepsilon_A = \left(1 - \frac{\rho_o}{\rho_B}\right) - \left(1 - \frac{\rho_o}{\rho_A}\right)$$
$$[\varepsilon] = \left(1 - \frac{\rho_A}{\rho_B}\right) \tag{3.7}$$

It follows that the velocity jump is related to the strain jump as shown below:

$$[v] = \dot{x}[\varepsilon] \tag{3.8}$$

The momentum conservation across the shock wave front can be written as follows:

$$\sigma_{R} - \sigma_{A} = \rho_{R}(v_{s} - v_{R})v_{R} - \rho_{A}(v_{s} - v_{A})v_{A}$$
(3.9)

From the mass conservation equation, we can substitute $\rho_B = \rho_A \frac{(v_s - v_A)}{(v_s - v_B)}$ into the momentum conservation equation, which will give us the following expression for the stress jump.

$$\sigma_{B} - \sigma_{A} = \rho_{A} \frac{v_{S} - v_{A}}{v_{S} - v_{B}} (v_{S} - v_{B}) v_{B} - \rho_{A} (v_{S} - v_{A}) v_{A}$$

$$\sigma_{B} - \sigma_{A} = \rho_{A} v_{S} v_{B} - \rho_{A} v_{A} v_{B} - \rho_{A} v_{S} v_{A} + \rho_{A} v_{A}^{2}$$

$$\sigma_{B} - \sigma_{A} = \rho_{A} (v_{S} - v_{A}) (v_{B} - v_{A})$$

$$[\sigma] = \rho_{A} \dot{x} [v]$$
(3.10)

From $[v] = \dot{x}[\varepsilon]$ and $\rho_A \approx \rho_o$, the stress jump can be re-written as:

$$[\sigma] = \frac{\rho_o[v]^2}{[\varepsilon]} \tag{3.11}$$

Finally, the relative shock speed and the velocity jump can be expressed as:

$$\dot{x} = \sqrt{\frac{1}{\rho_o} \frac{[\sigma]}{[\varepsilon]}} \tag{3.12}$$

$$[v] = \sqrt{\frac{1}{\rho_o} [\sigma][\varepsilon]}$$
 (3.13)

Note that the above formulations of the jump conditions are applicable to all shock wave models discussed in the upcoming section.

3.4 Shock Wave Models

This section focuses on four idealization models and discusses their respective approach and assumptions. In particular, the rigid-power law hardening (R-PLH) model will be elaborated in greater details, as this model will form the basis for formulating the modified analytical model in Chapter 5. Note that all these analytical models were formulated with respect to quasi-static constitutive relationship of the cellular materials.

3.4.1 Rigid-Perfectly Plastic-Locking (R-P-P-L) Model

Figure 3-3 shows the stress-strain idealization plot for the R-P-P-L material model.

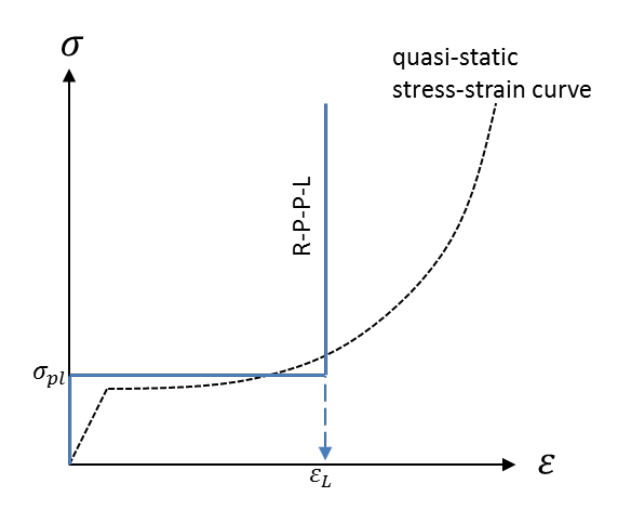


Figure 3-3: Stress-strain idealization plot for R-P-P-L model

Two model parameters are important in defining this idealization approach; the plateau stress σ_{pl} and the locking strain ε_L . The definition of the locking strain value adopted in this model has not been consistent among researchers. Tan et al. in [6] and [14] had defined this locking value as the strain corresponding to the onset of densification, while Lopatnikov et al. in [8] had used the densification strain (i.e. corresponds to the maximum strain) as the locking value. Chen et al. in [15] had based on the densification strain value recommended from [4] to compute analytical predictions of projectile penetration into metal foam using R-P-P-L

model. Nevertheless, Li et al. in [16] had presented some clarifications over the definition of the locking strain, which essentially relate to the onset to densification. With reference to Avalle et al. in [17], Li et al. in [16] had further improved the evaluation of the onset to densification strain using energy absorption efficiency method. Based on [16], the energy absorption efficiency parameter $\eta(\epsilon)$ can be evaluated from the quasi-static stress-strain curve of a cellular material using the following expression:

$$\eta(\varepsilon) = \frac{1}{\sigma(\varepsilon)} \int_0^{\varepsilon} \sigma(\varepsilon) \, d\varepsilon \tag{3.14}$$

The onset to densification strain ε_{cd} can then be determined as the strain value corresponding to the maximum point in the efficiency-strain curve (i.e. $\frac{d\eta(\varepsilon)}{d\varepsilon} = 0$). Figure 3-4 shows an illustration of how the densification strain can be determined.

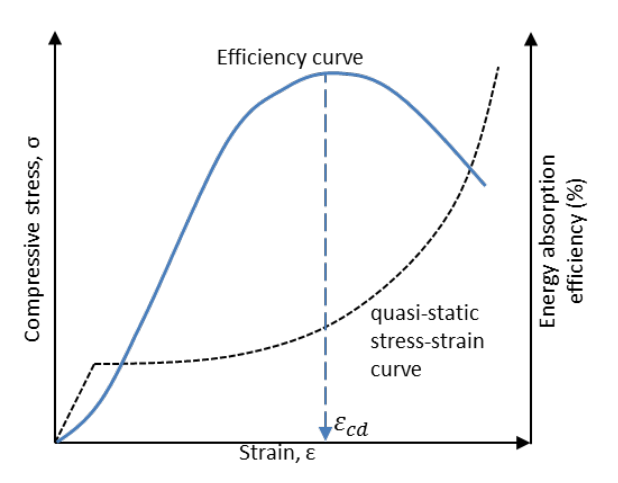


Figure 3-4: Quasi-static stress-strain curve and efficiency-strain curve for a typical foam material

The plateau stress is defined as the average stress that occurs between elastic yield strain and onset to densification strain, which can be determined by:

$$\sigma_{pl} = \frac{\int_{\varepsilon_y}^{\varepsilon_{cd}} \sigma(\varepsilon) \, d\varepsilon}{\varepsilon_{cd} - \varepsilon_y} \tag{3.15}$$

Table 3-1 presents the parameters used for the model. The pre-shock and post-shock region is equivalent to the region A and B respectively, as previously identified in Section 3.3. Considering that the initial elastic response of the cellular material is not taken into account, the material ahead of the shock wave front is instantaneously loaded up to the plateau stress σ_{pl} by the precursor elastic wave. The corresponding strain ε_A in the same region remained at zero. The particle velocity at the post-shock region follows the impact velocity V_o , while the particle velocity at pre-shock region is assumed to be zero. The material strain in the post-shock region is assumed to reach a particular strain-locking value ε_L .

Model Parameters	Post-Shock Region	Pre-Shock Region
Stress	σ_B	σ_{pl}
Strain	$arepsilon_L$	0
Particle Velocity	V_o	0

Table 3-1: Parameters assumed for R-P-P-L model

With reference to the Rankine-Hugoniot condition on stress jump (i.e. Eq. (3.11)), the stress jump $[\sigma]$ can be obtained as follows:

$$[\sigma] = \frac{\rho_o V_o^2}{\varepsilon_L} \tag{3.16}$$

The dynamically-enhanced material stress within the crushed region can be expressed as follows:

$$\sigma_B = \sigma_{pl} + \frac{\rho_o V_o^2}{\varepsilon_L} \tag{3.17}$$

3.4.2 Elastic-Perfectly Plastic-Rigid (E-P-P-R) Model

Figure 3-5 shows the stress-strain idealization plot for the E-P-P-R material model.

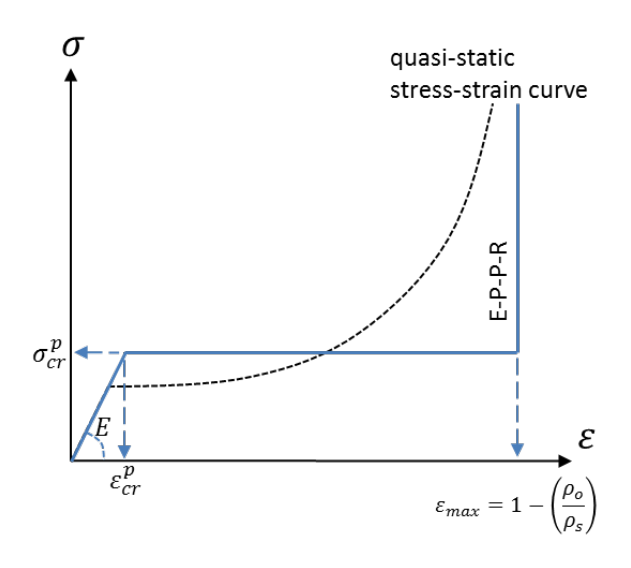


Figure 3-5: Stress-strain idealization plot for E-P-P-R model

This model uses three key parameters; critical stress σ_{cr}^p , elastic modulus E and locking strain ε_{max} . As mentioned earlier, the locking strain in this model is defined by the maximum strain limit as illustrated in Figure 3-5. Both the critical stress σ_{cr}^p and critical strain ε_{cr}^p delineate the onset to the quasi-plateau regime. The approach to determine these stress and strain parameters is similar to the R-P-P-L model, i.e. based on energy absorption method.

The total energy absorbed per unit volume of the cellular material, based on the quasi-static stress-strain curve, can be firstly determined as follows:

$$U_{max}^{qs} = \int_0^{\varepsilon_{max}} \sigma(\varepsilon) d\varepsilon \tag{3.18}$$

This is then followed by computing the critical stress σ_{cr}^p by assuming that the energy absorption within the E-P-P-R model and the quasi-static stress-strain curve is equivalent. Hence, this entails the following expression:

$$\frac{\left(\sigma_{cr}^{p}\right)^{2}}{2E} - \varepsilon_{max}\sigma_{cr}^{p} + U_{max}^{qs} = 0$$
(3.19)

Lopatnikov et al. in [8] had presented impact response of cellular materials under different velocity regimes. Specifically, he focused on Regime 2 and 3. Regime 1 and 4 refer to the supersonic and quasi-static regime respectively. Regime 2 occurs when the impact velocity is higher than the elastic wave speeds of all amplitudes in the foam material, which implies that only plastic shock wave is induced in this regime. Due to absence of precursor elastic wave, the cellular material ahead of the shock wave will be undisturbed. Therefore, it is inferred that following assumption in Table 3-2 will be considered for Regime 2:

Model Parameters	Post-Shock Region	Pre-Shock Region
Stress	$\sigma_{\!\scriptscriptstyle B}$	0
Strain	$arepsilon_{max}$	0
Particle Velocity	V_o	0

Table 3-2: Parameters assumed for Regime 2 in E-P-P-R model

Again, with reference to the Rankine-Hugoniot condition on stress jump (i.e. Eq. (3.11)), the stress jump $[\sigma]$ can be obtained as follows:

$$[\sigma] = \frac{\rho_o V_o^2}{\varepsilon_{max}} \tag{3.20}$$

The dynamically-enhanced material stress within the crushed region is:

$$\sigma_B = \frac{\rho_o V_o^2}{\varepsilon_{max}} \tag{3.21}$$

Regime 3 occurs when the impact velocity is lower than the linear sound velocity of stress wave in the cellular material, such that an elastic precursor wave will propagate ahead of the plastic shock wave. This precursor elastic wave will induce jump in material stress and strain from zero to critical stress σ_{cr}^p and critical strain ε_{cr}^p respectively. Considering linear acoustic relationship, the particle velocity v_A can be expressed as follows:

$$v_A = \frac{\sigma_{cr}^p}{\rho_o c_1} = \varepsilon_{cr}^p c_1 \tag{3.22}$$

The linear sound velocity c_1 of cellular material, which represents the effective velocity of sound wave of material in its elastic regime, can be determined using the following expression.

$$c_1 = \sqrt{\frac{E}{\rho_o}} \tag{3.23}$$

Based on the above discussion of material state affected by the precursor elastic wave, Table 3-3 presents the assumption of parameters considered for Regime 3:

Model Parameters	Post-Shock Region	Pre-Shock Region
Stress	$\sigma_{\!\scriptscriptstyle B}$	σ^p_{cr}
Strain	$arepsilon_{max}$	$arepsilon_{cr}^p$
Particle Velocity	V_o	$arepsilon_{cr}^p c_1$

Table 3-3: Parameters assumed for Regime 3 in E-P-P-R model

The stress jump $[\sigma]$ can be obtained as follows:

$$[\sigma] = \frac{\rho_o (V_o - \varepsilon_{cr}^p c_1)^2}{\varepsilon_{max} - \varepsilon_{cr}^p}$$
(3.24)

The dynamically-enhanced material stress within the crushed region is:

$$\sigma_B = \sigma_{cr}^p + \frac{\rho_o \left(V_o - \varepsilon_{cr}^p c_1 \right)^2}{\varepsilon_{max} - \varepsilon_{cr}^p}$$
(3.25)

It is worth to note that this E-P-P-R model does not consider the effect of wave reflection due to finite thickness of cellular materials.

3.4.3 Power Law Shock Model

Figure 3-6 shows the stress-strain idealization plot for the power law shock model.

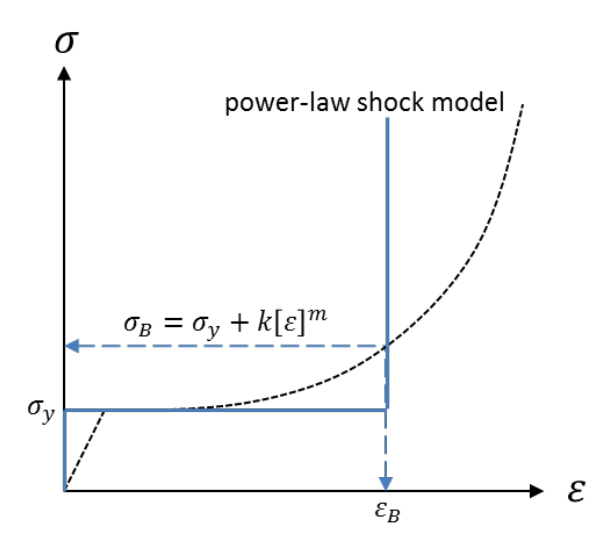


Figure 3-6: Stress-strain idealization for power law shock model

The power law shock model is an improvement to the R-P-P-L model, by allowing the changes in crushing strain that corresponds to the initial impact velocity. Unlike R-P-P-L model where the material strain in the post-shock region is locked at certain pre-fixed strain value, power law shock model evaluates the shock stress and crushing strain depending on the initial impact velocity. The strain hardening regime of the constitutive curve is described by the initial yield stress σ_y , the power m and the coefficient K as shown below.

$$\sigma = \sigma_{v} + K\varepsilon^{m} \tag{3.26}$$

Similar to R-P-P-L model, power law shock model does not account for initial elasticity and hence, the material strain ε_A in the pre-shock region is zero. Nevertheless, the material ahead of the shock wave front is loaded up to the yielding stress σ_y by the precursor elastic wave. This model also assumed zero velocity for the particle within the pre-shock region. Therefore, by equating the expressions of the stress jump from the Rankine-Hugoniot relationship and the power law equation, the material locking strain in the post-shock region can be evaluated as shown below:

$$K\varepsilon_B^m = \frac{\rho_o V_o^2}{\varepsilon_B} \tag{3.27}$$

$$K\varepsilon_B^m = \frac{\rho_o V_o^2}{\varepsilon_B}$$

$$\varepsilon_B = \left(\frac{\rho_o V_o^2}{K}\right)^{\frac{1}{m+1}}$$
(3.27)

Table 3-4 presents the parameters used for the power law shock model.

Model Parameters	Post-Shock Region	Pre-Shock Region
Stress	σ_B	$\sigma_{\!\scriptscriptstyle \mathcal{Y}}$
Strain	$\varepsilon_B = \left(\frac{\rho_o V_o^2}{k}\right)^{\frac{1}{m+1}}$	0
Particle Velocity	V_o	0

Table 3-4: Parameters assumed for power law shock model

Therefore with the assumed parameters, the stress jump $[\sigma]$ can be obtained as follows:

$$[\sigma] = \frac{\rho_o V_o^2}{\varepsilon_R} \tag{3.29}$$

The dynamically-enhanced material stress within the crushed region is:

$$\sigma_B = \sigma_y + \frac{\rho_o V_o^2}{\varepsilon_B} \tag{3.30}$$

3.4.4 Rigid-Power Law Hardening (R-PLH) Model

For the previously discussed shock wave models, the stress enhancement (i.e. combining the plastic crushing force and dynamic effects) within the crushed region are generally time-independent. This is primarily attributed by the assumption of constant velocity and strain jump across the shock wave front, as specified in the dynamic force term. In R-P-P-L and E-P-P-R model, the shock strain in the crushed region is defined by the pre-fixed locking strain value, while in the Power Law Shock Model, the locking strain is determined based on the initial impact velocity. The particle velocity jumps in all these analytical models are assumed to be constant in time-domain as well. However in reality, inertia energy is lost through crushing of cellular material which will result decreases in particle velocity and strain jump over time.

Figure 3-7 shows the stress-strain idealization plot for the R-PLH model, which was developed based on continuum-based shock wave theory. This approach combines the shock wave theory, together with the constitutive model that describes the non-linear strain hardening response of the cellular material.

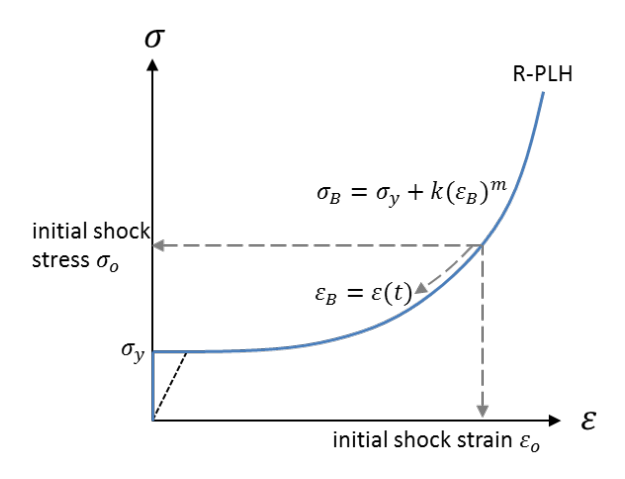


Figure 3-7: Stress-strain idealization plot for R-PLH model

The initial elastic property of cellular material is not accounted for in this model, considering that it is not possible to derive a closed-form solution and the complexities involved when assessing moderate impact velocity [13]. In Zheng et al. [13], two different impact scenarios were considered; striker-rod impact and rod-target impact. Only the solution for the striker-rod impact scenario will be discussed here, given that this particular scenario is more applicable to our debris penetration problem. The striker-rod impact scenario is illustrated in Figure 3-2.

The position of the plastic shock wave front as a function of time is firstly evaluated. This is done so by considering the time derivatives of both velocity and strain jump across shock wave front, as well as computing the total mass acceleration of rigid impactor and crushed material behind the shock wave front. Similar to the previous models, an elastic precursor wave propagates instantaneously ahead of the plastic shock wave. This model considers both the particle velocity and material strain at pre-shock region to be zero, while the material in the same region to be stressed up to yield stress σ_y . As such, with the jump conditions specified below, the velocity jump equation in the earlier section can be re-written as follows:

$$[v] = v_B(t) = v_B \qquad [\sigma] = \sigma(\varepsilon) - \sigma_y \qquad [\varepsilon] = \varepsilon_B(t) = \varepsilon_B$$

$$v_B = \sqrt{\frac{1}{\rho_o} (\sigma(\varepsilon) - \sigma_y) \varepsilon_B} \qquad (3.31)$$

The time derivatives of the velocity and strain jump can be obtained accordingly.

$$\frac{d}{dt}(v_B) = \frac{\frac{1}{2} \left(\sigma'(\varepsilon) + \frac{\sigma(\varepsilon) - \sigma_y}{\varepsilon_B}\right) \dot{\varepsilon}}{\rho_o \sqrt{\frac{1}{\rho_o} \left(\frac{\sigma(\varepsilon) - \sigma_y}{\varepsilon_B}\right)}}$$
(3.32)

The above expression can be further simplified with shock wave velocity \dot{x} and the average between the slopes of tangent line (i.e. first derivative of the stress $\sigma(\varepsilon)$) and the Rayleigh line (i.e. line that join the two stress states $(0, \sigma_y)$ and $(\varepsilon_B, \sigma_B)$. Figure 3-8 illustrates the Rayleigh line that describes the constitutive states of the material under the influence of plastic compressive shock wave. The subsequent stress-strain reduction of material closely behind the shock wave front follows the constitutive curve as illustrated in Figure 3-7.

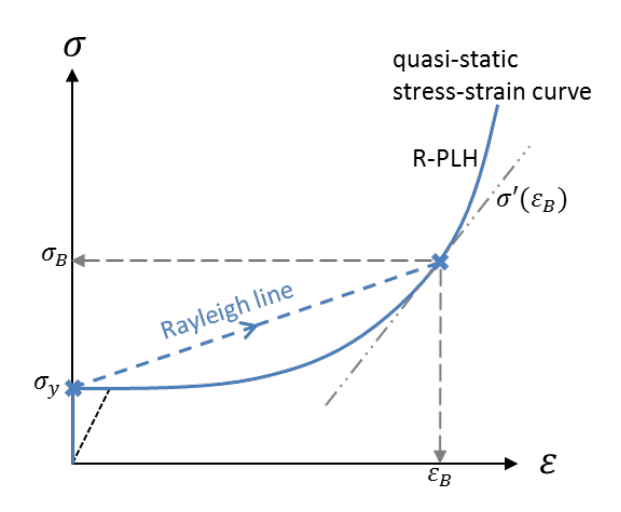


Figure 3-8: Rayleigh line describing the material states under plastic shock compression wave

$$k(\varepsilon) = \frac{1}{2} \left(\sigma'(\varepsilon) + \frac{\sigma(\varepsilon) - \sigma_y}{\varepsilon_B} \right)$$
 (3.33)

$$\dot{x} = \sqrt{\frac{1}{\rho_o} \left(\frac{\sigma(\varepsilon) - \sigma_y}{\varepsilon_B} \right)}$$
 (3.34)

$$\frac{d}{dt}(v_B) = \frac{k(\varepsilon)\dot{\varepsilon}}{\rho_o\dot{x}} \tag{3.35}$$

The total mass acceleration of rigid impactor and crushed material behind the shock wave front is

$$\left(M_o + \rho_o A_o x(t)\right) \frac{d}{dt}(v_B) = -\sigma(\varepsilon) A_o \tag{3.36}$$

 M_o refers to the mass of rigid impactor, A_o refers to the cross-sectional area of cellular material and x(t) is the Lagrangian position of shock wave front at time, t. Note that velocity of the impactor and crushed material is assumed to be the same (i.e. v_B). At this juncture, it is worth to highlight that the stress component responsible for resisting the motion of impactor and crushed material is the shock stresses of material directly behind the shock wave front. This is one of the key differences comparing with other shock wave models (e.g. R-P-P-L, E-P-P-R and Power Law Shock Model) previously discussed. These models consider the material stresses directly ahead of the impactor in their equation of motion.

With the definition of specific mass $m = \frac{M_0}{A_0}$, the above expression can be re-arranged to give

$$\frac{d}{dt}(v_B) = -\frac{\sigma(\varepsilon)}{m + \rho_0 x(t)} \tag{3.37}$$

Combining the above total mass acceleration and the time derivations of the velocity and strain jump and performing integration, we can obtain the lagrangian position of the plastic shock wave front as a function of time.

The initial conditions include:

At time t = 0; x(t = 0) = 0, $\varepsilon(t = 0) = \varepsilon_0$

$$x(t) = \frac{m}{\rho_o} \left(\exp\left(-\int_{\varepsilon_o}^{\varepsilon(t)} \frac{k(\varepsilon)}{\sigma(\varepsilon)} d\varepsilon\right) - 1 \right)$$
 (3.38)

Hence, the velocity of shock wave front can be determined by taking the time derivative of x(t).

$$\frac{d}{dt}x(t) = -\frac{mk(\varepsilon)}{\rho_o\sigma(\varepsilon)}\exp\left(-\int_{\varepsilon_o}^{\varepsilon(t)} \frac{k(\varepsilon)}{\sigma(\varepsilon)} d\varepsilon\right) \frac{d\varepsilon}{dt}$$
(3.39)

The above shock wave velocity can be further simplified with a dimensionless function $f(\varepsilon)$ that comprises information on the constitutive relation, particularly, the strain hardening regime of the cellular material.

$$f(\varepsilon) = \frac{k(\varepsilon)}{\sigma(\varepsilon)} \exp\left(-\int_{\varepsilon_o}^{\varepsilon(t)} \frac{k(\varepsilon)}{\sigma(\varepsilon)} d\varepsilon\right)$$
(3.40)

$$\frac{d}{dt}x(t) = -\frac{m}{\rho_o}f(\varepsilon)\frac{d\varepsilon}{dt}$$
(3.41)

Combining with the shock speed defined in the Section 4.3 and performing integration to obtain the time function with respect to the shock strain and stress directly behind the shock wave front.

$$\sqrt{\frac{\sigma(\varepsilon) - \sigma_{y}}{\rho_{o}\varepsilon_{B}}} dt = -\frac{m}{\rho_{o}} f(\varepsilon) d\varepsilon$$
(3.42)

$$t = -\frac{mV_o}{\sigma_y} \int_{\varepsilon_o}^{\varepsilon(t)} \frac{f(\varepsilon)\sqrt{\sigma_y \varepsilon_B}}{\sqrt{\alpha \varepsilon_o (\sigma(\varepsilon) - \sigma_y)}} d\varepsilon$$
(3.43)

Where,
$$\alpha = \frac{K \varepsilon_o^n}{\sigma_y}$$

K is the strength index while the n is the strain hardening index. α is termed as the stress-enhancement parameter related to the initial shock stress ε_o . The initial shock strain and stress can be expressed by:

$$\varepsilon_o = \left(\frac{\rho_o(V_o)^2}{K}\right)^{\frac{1}{n+1}} \quad ; \qquad \sigma(\varepsilon_o) = \sigma_y + K \left(\frac{\rho_o(V_o)^2}{K}\right)^{\frac{n}{n+1}} \tag{3.44}$$

With the following relationship,

$$\sigma'(\varepsilon) = n \frac{\sigma(\varepsilon) - \sigma_{y}}{\varepsilon_{B}} \quad \to \quad k(\varepsilon) = \frac{n+1}{2n} \sigma'(\varepsilon) = q \sigma'(\varepsilon) \tag{3.45}$$

The expression that describes the lagrangian position of the plastic shock wave front as a function of time can be re-written as

$$x(t) = \frac{m}{\rho_o} \left(\left(\frac{\sigma(\varepsilon_B)}{\sigma(\varepsilon_o)} \right)^{-q} - 1 \right)$$
 (3.46)

With the general definition of the hardening curve using the power-law equation,

$$\sigma(\varepsilon) = \sigma_y + K\varepsilon^n \tag{3.47}$$

The dimensionless function $f(\varepsilon)$ can be re-written as

$$f(\varepsilon) = \frac{nq\alpha(1+\alpha)^q \left(\frac{\varepsilon_B}{\varepsilon_o}\right)^{n-1}}{\varepsilon_o \left(1+\alpha \left(\frac{\varepsilon_B}{\varepsilon_o}\right)^n\right)^{q+1}}$$
(3.48)

Substituting this function of $f(\varepsilon)$ into the time function with respect to the shock strain and stress within the crushed region and solving the integral will give

$$t = -\frac{mV_o nq}{\sigma_y \varepsilon_o} (1 + \alpha)^q \int_{\varepsilon_o}^{\varepsilon_B} \frac{\left(\frac{\varepsilon_B}{\varepsilon_o}\right)^{\frac{n-1}{2}}}{\left(1 + \alpha \left(\frac{\varepsilon_B}{\varepsilon_o}\right)^n\right)^{q+1}} d\varepsilon$$

$$t = T \left(1 - \left(\frac{1 + \alpha}{\left(\frac{\varepsilon_B}{\varepsilon_o}\right)^{-n} + \alpha}\right)^q\right)$$
(3.49)

Where $T = \frac{mV_o}{\sigma_y}$ refers to the characteristic time parameter that relates the conversion of the mass's kinetic energy into the internal energy of the cellular material.

Re-arranging the expression will give us the shock strain function in time domain.

$$\varepsilon_{B} = \varepsilon_{B}(t) = \varepsilon_{o} \left(\frac{1 + \alpha}{\left(1 - \left(\frac{t}{T}\right)\right)^{\frac{1}{q}}} - \alpha \right)^{-\frac{1}{n}}$$
(3.50)

Given that $\sigma(\varepsilon) = \sigma_y + K\varepsilon^n$, the function to describe the time-dependent dynamically-enhanced material stress is

$$\sigma_B(t) = \sigma_y \left(1 + \alpha \left(\frac{1 + \alpha}{\left(1 - \frac{t}{T} \right)^{\frac{1}{q}}} - \alpha \right)^{-1} \right)$$
 (3.51)

The function that describes the velocity jump across the shock wave front, with respect to time, can also be determined using the following relationship:

$$v_B = \sqrt{\frac{1}{\rho_o} (\sigma(\varepsilon_B) - \sigma_y) \varepsilon_B}$$

$$v_B(t) = V_o \left(\frac{1+\alpha}{\left(1 - \frac{t}{T}\right)^{\frac{1}{q}}} - \alpha \right)^{-q}$$
(3.52)

Note that the velocity jump [v] is also equal to the particle velocity of the crushed material behind the shock wave front, since in this model, the particle velocity of the material in the uncrushed region is zero.

The total time of debris penetration $t = T_{end}$ can be obtained by substituting $v_B(t) = 0$.

With the total time of penetration, the total penetration distance D_{end} of the debris can be computed by taking definite integration of the debris velocity-time function $v_B(t)$.

$$D_{end} = \int_{t=0}^{T_{end}} v_B(t) dt$$
 (3.53)

The plastic shock wave velocity can be evaluated using the following expression:

$$\dot{x} = \sqrt{\frac{1}{\rho_o} \frac{[\sigma]}{[\varepsilon]}}$$

$$\dot{x} = \frac{V_o}{\varepsilon_o} \left(\frac{1 + \alpha}{\left(1 - \frac{t}{T}\right)^{\frac{1}{q}}} - \alpha \right)^{q - 1}$$
(3.54)

With the shock wave velocity-time function derived, the total distance of material crushing X_{end} between the debris and the shock wave front can be evaluated by taking finite integration of this shock wave speed relative to the particle velocity ahead of the shock front.

$$X_{end} = \int_{t=0}^{T_{end}} \dot{x}(t) dt$$
 (3.55)

4. Modified R-PLH Model

The one-dimensional shock wave models discussed thus far hold the assumption that the frontal face of the impactor remains vertically-flat (i.e. perpendicular to the direction of impact motion) and the interface between cellular material and impactor's nose remains frictionless. However, in the problem where penetration of debris through the cellular material is concerned, it is fairly reasonable to consider effects that could influence the penetration resistance. These effects include changes in nose geometry of the debris and frictional resistances. Thus, this chapter will explain the possible adjustments to the existing R-PLH model and proposed a modified analytical model to encompass these effects.

Furthermore, the modified model will also account for the changes in material state due to incidental elastic wave propagation ahead of the shock wave front. Though, due to complexity involved when dealing with shock and elastic waves propagating through cellular medium of different densities, the effects of wave reflections and interactions will be excluded in this modified analytical model. Lastly, this chapter will compare and discuss predictions on debris penetrations under certain impact scenario using certain analytical models of interest.

4.1 Shape Coefficients, Frictional Resistance and Initial Elasticity

Jones et al. in [18] included the effect of pressure-dependent friction on the normal impact and penetration problem by a rigid projectile. Chen and Li in [19] presented two dimensionless parameters to be included in the penetration resistance, when formulating the equation of motion. These parameters, known as the shape coefficients, are related to the geometry of the projectile's nose shape, which take frictional resistance into consideration. In respect to this thesis work, only debris with vertical-flat (i.e. with rectangular cross-section) and hemispherical nose shape will be considered.

Figure 4-1 shows the cross-section of an axisymmetric projectile, with illustrations of the normal and tangential reaction forces that resist the motion of the projectile.

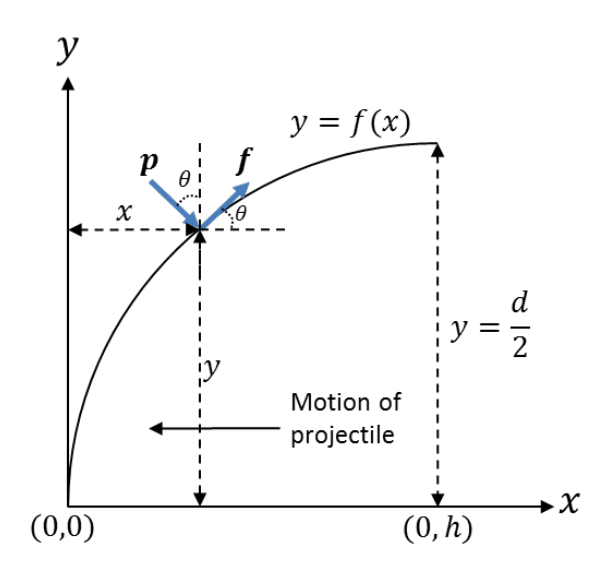


Figure 4-1: Cross-section for an axisymmetric projectile with hemispherical nose shape

Based on simple geometrical derivation, the increment of the resultant resisting force per arc length of the projectile's nose surface can be presented as:

$$dF = 2\pi y (psin\theta + fcos\theta)ds \tag{4.1}$$

Therefore, the overall net motion-resisting force can be eventually expressed as

$$F = 2\pi \int_0^h (yy'p + yf)dx \tag{4.2}$$

Where p refers to the normal crushing force acting on the projectile, due to the material stress behind the shock wave front, while f refers to the frictional force (i.e. as a function of p with μ as the dynamic friction coefficient). y refers to the function that describes the geometry of the projectile nose shape. In accordance to Jones et al. [18], the distribution of p over the nose surface is not uniform, considering that the moving direction of particle velocities changes over the nose surface. This explains why a factor of $\sin^2 \theta$ is applied to the dynamic terms of the resisting function p. In the problem of debris penetration within cellular material, the resisting force p can be written in the same form as the dynamically-enhanced stress of the material behind the shock wave front. Hence, bearing in mind the similar effect of the nose geometry on the material stress, the resisting force and the frictional force can be considered as:

$$p = \sigma_{v} + K\varepsilon^{n} \sin^{2} \theta \tag{4.3}$$

$$f = \mu(\sigma_y + K\varepsilon^n \sin^2 \theta) \tag{4.4}$$

The net motion-resisting force equation can be re-written as:

$$F = 2\pi \int_0^h \left(K \varepsilon^n y \frac{y'^3 + \mu y'^2}{1 + y'^2} + \sigma_y (yy' + y\mu) \right) dx \tag{4.5}$$

According to Chen and Li in [19], the relevant shape coefficients for a projectile with hemispherical nose shape geometry can be introduced as:

$$N_1 = 1 + \frac{8\mu}{d^2} \int_0^h y \, dx \tag{4.6}$$

$$N_2 = N^* + \frac{8\mu}{d^2} \int_0^h \frac{yy'^2}{1 + y'^2} dx$$
 (4.7)

$$N^* = \frac{8}{d^2} \int_0^h \frac{yy'^3}{1 + y'^2} dx \tag{4.8}$$

Where d refers to the diameter of the projectile (in this case, projectile also refer to the debris)

Finally, the resulting dynamically-enhanced stress that incorporates the effects of nose geometry and frictional resistance can be written as

$$\sigma(\varepsilon_B) = N_1 \sigma_v + N_2 K \varepsilon^n \tag{4.9}$$

The shape coefficients for a projectile with flat vertical nose are $N_1 = N_2 = 1$. However, it shall be noted that thus far, only frictional resistance along the nose's surface is considered (i.e. the friction traction along the debris body shaft is ignored).

In summary, the plastic crushing resistance of cellular material to debris penetration with a hemispherical nose shape shall be written as:

$$F_R = \frac{\pi d^2}{4} \left(N_1 \sigma_y + N_2 K \varepsilon^n \right) \tag{4.10}$$

Similarly, for the case of debris with rectangular cross-section (i.e. with vertical flat nose shape), the resistance force can be written as:

$$F_R = wh(N_1\sigma_y + N_2 K\varepsilon^n)$$
(4.11)

Where w and h are the width and height of the rectangular-shape debris respectively.

Turning the attention to the initial elastic property of the cellular material, this "partial" effect of initial elastic response on the penetration resistance will be incorporated into the modified analytical model. The reflection/refraction and interaction of waves along the cellular material will be relatively complex to incorporate into the analytical solution and thus, will not be accounted for. However, the effects of particle velocities, strains and stresses induced by the incident elastic wave within the pre-shocked region will be considered. Nevertheless, one shall note with the fact that the elastic limit strain for cellular material are considerably smaller than its plastic strains, the influence of the initial elastic response on the overall penetration phenomenon may not be significant.

4.2 Proposed Modifications to R-PLH Model

The principle approach to incorporate the shape coefficients into the existing R-PLH model is by modifying the equation of motion that describes the debris penetration into the foam material. The remaining basic formulations that define the constitutive relations of the foam material will not be affected. The effect of material elasticity, particularly influencing the material states within the pre-shock region, will be incorporated into the jump conditions (i.e. sudden changes in physical quantities of material) across the shock wave front. Figure 4-2 illustrates the material constitutive relation of the proposed modified model. Figure 4-3 shows the constitutive relations in stress versus plastic strain plot.

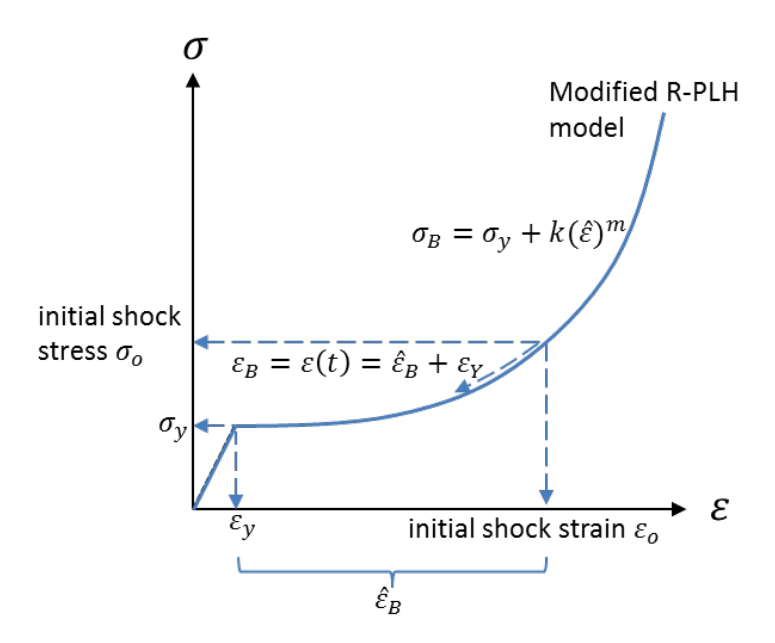


Figure 4-2: Stress-strain idealization for modified R-PLH model (in σ vs ε)

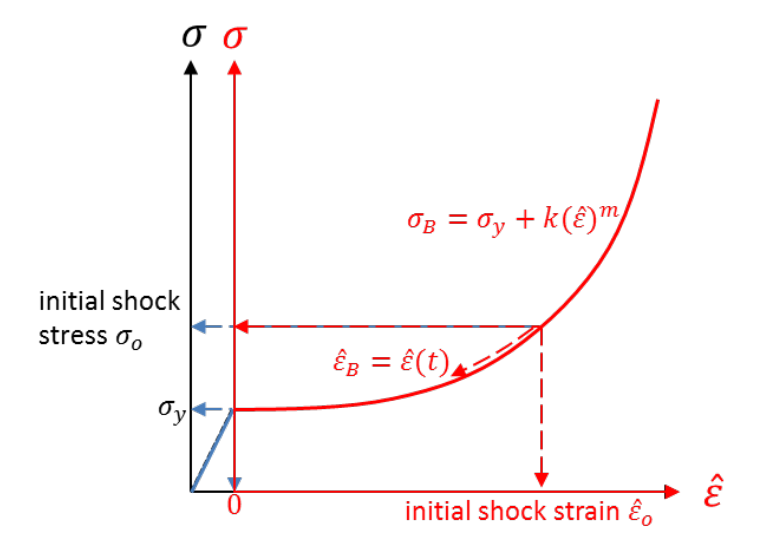


Figure 4-3: Stress-strain idealization for modified R-PLH model (in σ vs $\hat{\epsilon}$)

With the inclusion of the elastic strain ε_Y into the constitutive relation, the particle velocity and the material strain at the pre-shock region will be v_A and ε_Y respectively. Similarly to the Regime 3 in E-P-P-R model discussed previously, the initial particle velocity v_A can be defined as:

$$v_{A_{initial}} = \frac{\sigma_{y}}{\rho_{o}c_{1}} = \varepsilon_{Y}c_{1} \tag{4.12}$$

Where the linear sound velocity of the foam material c_1 can be determined using the following expression.

$$c_1 = \sqrt{\frac{E}{\rho_o}} \tag{4.13}$$

Therefore, the revised jump conditions across the shock wave front, in function of time, will be written as follow:

$$[\sigma] = \sigma(\hat{\varepsilon}_B(t)) - \sigma_y$$
 $[\varepsilon] = \varepsilon_B(t) - \varepsilon_Y = \hat{\varepsilon}_B(t)$ $[v] = v_B(t) - v_A(t)$

$$[\sigma] = \frac{\rho_o[v]^2}{[\varepsilon]} = \frac{\rho_o(v_B(t) - v_A(t))^2}{(\varepsilon_B(t) - \varepsilon_Y)} = \frac{\rho_o(v_B(t) - v_A(t))^2}{\hat{\varepsilon}_B(t)}$$
(4.14)

$$v_B(t) = \sqrt{\frac{1}{\rho_o} \left(\sigma(\hat{\varepsilon}_B) - \sigma_y\right) \hat{\varepsilon}_B} + v_A(t)$$
 (4.15)

The time derivatives of the relative velocity and strain jump can be obtained accordingly.

$$\frac{d}{dt}(v_B - v_A) = \frac{d}{dt}\left(v_{B_{relative}}\right) = \frac{\frac{1}{2}\left(\sigma'(\hat{\varepsilon}_B) + \frac{\sigma(\hat{\varepsilon}_B) - \sigma_y}{\hat{\varepsilon}_B}\right)\hat{\varepsilon}_B}{\rho_o\sqrt{\frac{1}{\rho_o}\left(\frac{\sigma(\hat{\varepsilon}_B) - \sigma_y}{\hat{\varepsilon}_B}\right)}} \tag{4.16}$$

Similarly, the above expression can be further simplified with relative shock wave velocity \dot{x} and the average between the slopes of tangent line at shock state and the Rayleigh line. Figure 4-4 illustrates the Rayleigh line which describes the constitutive states of material under the effect of precursor elastic wave and plastic shock wave. Similarly, the subsequent stress-strain reduction of material closely behind the shock wave front follows the constitutive curve as presented in Figure 4-3. It is worth to note that the "unloading" path of the material at a fixed location does not follow the stress-strain curve, but rather, depends on the material unloading characteristics (i.e. with or without elastic recovery).

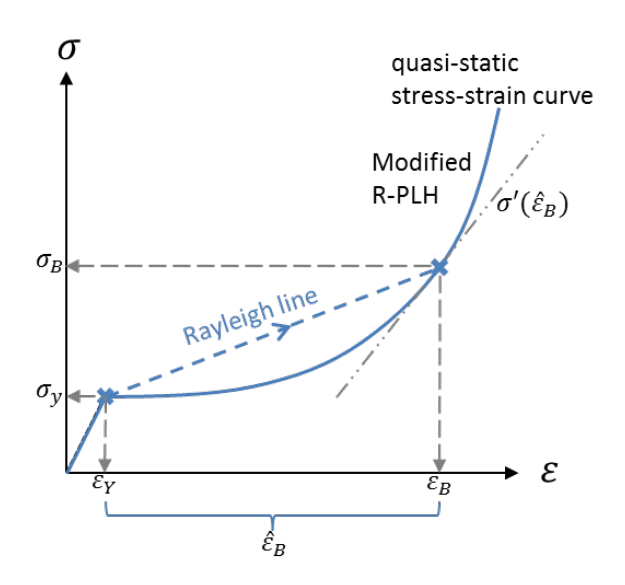


Figure 4-4: Rayleigh line for modified R-PLH model

$$k(\hat{\varepsilon}_B) = \frac{1}{2} \left(\sigma'(\hat{\varepsilon}_B) + \frac{\sigma(\hat{\varepsilon}_B) - \sigma_y}{\hat{\varepsilon}_B} \right)$$
(4.17)

$$\dot{x} = \sqrt{\frac{1}{\rho_o} \left(\frac{\sigma(\hat{\varepsilon}_B) - \sigma_y}{\hat{\varepsilon}_B} \right)} \tag{4.18}$$

$$\frac{d}{dt}(v_{Brelative}) = \frac{k(\hat{\varepsilon}_B)\dot{\hat{\varepsilon}_B}}{\rho_o \dot{x}}$$
(4.19)

Note that the \dot{x} refers to the shock wave speed relative to the particle velocity v_A , ahead of plastic shock wave.

Incorporating the shape coefficients into the equation of motion that describes the total mass acceleration of the rigid debris and crushed material behind the shock wave front, the following expression can be obtained

$$(M_o + \rho_o A_o x(t)) \frac{d}{dt} (v_{Brelative}) = -\sigma^*(\hat{\varepsilon}_B) A_o$$
(4.20)

Where $\sigma^*(\hat{\varepsilon}_B)$ can be expressed as follow:

$$\sigma^*(\hat{\varepsilon}_R) = N_1(\sigma_v) + N_2 K(\hat{\varepsilon}_R)^n \tag{4.21}$$

Therefore,

$$\frac{d}{dt}(v_{B_{relative}}) = -\frac{\sigma^*(\hat{\varepsilon}_B)}{m + \rho_o x(t)}$$
(4.22)

Note that x(t) no longer represents the lagrangian position of the shock wave front since the particle velocity in the pre-shock region is non-zero. However, x(t) describes the length of material crushing behind the shock wave over the time domain.

As per similar to the original R-PLH model, we can obtain the following expression of the function of x(t):

$$x(t) = \frac{m}{\rho_o} \left(\exp\left(-\int_{\hat{\varepsilon}_o}^{\hat{\varepsilon}_B(t)} \frac{k(\hat{\varepsilon}_B)}{\sigma^*(\hat{\varepsilon}_B)} d\hat{\varepsilon}_B \right) - 1 \right)$$
(4.23)

The relative velocity of shock wave front can then be determined by taking the time derivative of x(t).

$$\frac{d}{dt}x(t) = -\frac{mk(\hat{\varepsilon}_B)}{\rho_o \sigma^*(\hat{\varepsilon}_B)} \exp\left(-\int_{\hat{\varepsilon}_o}^{\hat{\varepsilon}_B(t)} \frac{k(\hat{\varepsilon}_B)}{\sigma^*(\hat{\varepsilon}_B)} d\hat{\varepsilon}_B\right) \frac{d\hat{\varepsilon}_B}{dt}$$
(4.24)

In which the dimensionless function $f^*(\hat{\varepsilon}_R)$ is

$$f^*(\hat{\varepsilon}_B) = \frac{k(\hat{\varepsilon}_B)}{\sigma^*(\hat{\varepsilon}_B)} \exp\left(-\int_{\hat{\varepsilon}_O}^{\hat{\varepsilon}_B(t)} \frac{k(\hat{\varepsilon}_B)}{\sigma^*(\hat{\varepsilon}_B)} d\hat{\varepsilon}_B\right)$$
(4.25)

By combining with the relative shock speed defined in the earlier section and performing integration, the time function with respect to the shock strain and stress directly behind the shock wave front can be expressed as

$$t = -T \int_{\hat{\varepsilon}_o}^{\hat{\varepsilon}_B(t)} \frac{f^*(\hat{\varepsilon}_B) \sqrt{\sigma_y \hat{\varepsilon}_B}}{\sqrt{\alpha \hat{\varepsilon}_o (\sigma(\hat{\varepsilon}_B) - \sigma_y)}} d\hat{\varepsilon}_B$$
(4.26)

Where the stress-enhancement parameter α related to the initial shock stress, the characteristic time parameter, the initial shock strain and stress can be expressed respectively as follows.

$$\alpha = \frac{K(\hat{\varepsilon}_o)^n}{\sigma_v} \tag{4.27}$$

$$T = \frac{m(V_o - v_{A_{initial}})}{\sigma_{v_i}} \tag{4.28}$$

$$\hat{\varepsilon}_o = \left(\frac{\rho_o \left(V_o - v_{A_{initial}}\right)^2}{K}\right)^{\frac{1}{n+1}} \quad ; \quad \sigma(\varepsilon_o) = \sigma_y + K \left(\frac{\rho_o \left(V_o - v_{A_{initial}}\right)^2}{K}\right)^{\frac{n}{n+1}} \quad (4.29)$$

With the following relationship,

$$\sigma'(\hat{\varepsilon}_B) = n \frac{\sigma(\hat{\varepsilon}_B) - \sigma_y}{\hat{\varepsilon}_B} \quad \to \quad k(\hat{\varepsilon}_B) = \frac{n+1}{2n} \sigma'(\hat{\varepsilon}_B) = q \sigma'(\hat{\varepsilon}_B)$$
 (4.30)

$$\sigma'(\hat{\varepsilon}_R) = nK(\hat{\varepsilon}_R)^{n-1} \tag{4.31}$$

$$\sigma^*(\hat{\varepsilon}_R) = N_1(\sigma_V) + N_2 K(\hat{\varepsilon}_R)^n \tag{4.32}$$

The dimensionless function $f(\varepsilon)$ can be re-written as

$$f^*(\hat{\varepsilon}_B) = \frac{nq\alpha(N_1 + N_2\alpha)^q \left(\frac{\hat{\varepsilon}_B}{\hat{\varepsilon}_o}\right)^{n-1}}{\hat{\varepsilon}_o \left(N_1 + N_2\alpha \left(\frac{\hat{\varepsilon}_B}{\hat{\varepsilon}_o}\right)^n\right)^{q+1}}$$
(4.33)

Note that $\sigma'(\hat{\varepsilon}_B)$ does not contain shape coefficients since $\sigma'(\hat{\varepsilon}_B)$ is derived based on the constitutive relations of the material.

Substitute this function of $f^*(\hat{\varepsilon}_B)$ into the time function with respect to the shock strain and stress, and solve the integral will give

$$t = \frac{T}{N_1} \left(1 - \left(\frac{N_1 + N_2 \alpha}{N_1 \left(\frac{\hat{\varepsilon}_B}{\hat{\varepsilon}_O} \right)^{-n} + N_2 \alpha} \right)^q \right)$$
(4.34)

Therefore, re-arranging the above expression will give us shock strain function in time domain.

$$\hat{\varepsilon}_{B} = \hat{\varepsilon}_{B}(t) = \hat{\varepsilon}_{o} \left(\frac{1}{N_{1}} \left(\frac{N_{1} + N_{2}\alpha}{\left(1 - \frac{t(N_{1})}{T}\right)^{\frac{1}{q}}} - N_{2}\alpha \right) \right)^{-\frac{1}{n}}$$
(4.35)

It is imperative to note that $\hat{\varepsilon}_B$ is not referring to the actual strain value. The actual strain value can be evaluated by evaluating $\varepsilon_B = \hat{\varepsilon}_B + \varepsilon_Y$

Given that $\sigma(\hat{\varepsilon}_B) = \sigma_y + K(\hat{\varepsilon}_B)^n$, the function to describe the time-dependent dynamically-enhanced material stress is

$$\sigma(\hat{\varepsilon}_B) = \sigma_B(t) = \sigma_y \left(1 + \alpha \left(\frac{1}{N_1} \left(\frac{N_1 + N_2 \alpha}{\left(1 - \frac{t(N_1)}{T} \right)^{\frac{1}{q}}} - N_2 \alpha \right) \right)^{-1} \right)$$
(4.36)

The function that describes the change in particle velocity within the post-shock region with respect to time can also be obtained with the following relationship:

$$v_B(t) - v_A(t) = \sqrt{\frac{1}{\rho_o} \left(\sigma(\hat{\varepsilon}_B) - \sigma_y\right) \hat{\varepsilon}_B}$$
(4.37)

$$v_{B_{relative}} = \left(V_o - v_{A_{initial}}\right) \left(\frac{1}{N_1} \left(\frac{N_1 + N_2 \alpha}{\left(1 - \frac{t(N_1)}{T}\right)^{\frac{1}{q}}} - N_2 \alpha\right)\right)^{-q}$$
(4.38)

It is worth to note that the particle velocity v_A within the pre-shock region will be time-dependent. T_{end} refers to the total time of debris penetration. With the total time of debris penetration, the total penetration distance D_{end} for the debris can be computed by summing up the definite integration of the debris relative velocity-time function and the additional distance due to the particle velocity v_A . An upper and lower bound approximation of the particle velocity $v_A(t)$ can be considered; upper bound assumes constant v_A throughout the penetration time, while the lower bound assumes v_A to decrease linearly from $v = v_{A_{initial}}$ at time t = 0 to v = 0 at time $t = t_{end}$. The total penetration time t_{end} is taken as the time for the relative velocity of debris and shock wave front to reach zero.

With upper bound assumption:

$$D_{end,upper} = \int_{t=0}^{T_{end}} v_{B_relative}(t) dt + v_{A_{initial}} T_{end}$$
 (4.39)

With lower bound assumption:

$$D_{end,lower} = \int_{t=0}^{T_{end}} v_{B_relative}(t) dt + \frac{1}{2} v_{A_{initial}} T_{end}$$
 (4.40)

The plastic shock wave relative velocity can be evaluated using the following expression:

$$\dot{x} = \sqrt{\frac{1}{\rho_o} \frac{[\sigma]}{[\varepsilon]}}$$

$$\dot{x} = \frac{V_o - v_{A_{initial}}}{\hat{\varepsilon}_o} \left(\frac{1}{N_1} \left(\frac{N_1 + N_2 \alpha}{\left(1 - \frac{t(N_1)}{T}\right)^{\frac{1}{q}}} - N_2 \alpha \right) \right)^{q-1}$$
(4.41)

With the shock wave relative velocity-time function derived, the total distance of material crushing X_{end} between the debris and the shock wave front can be evaluated as follows:

With upper bound assumption:

$$X_{end,upper} = \int_{t=0}^{T_{end}} \dot{x}(t) dt + v_{A_{initial}} T_{end}$$
 (4.42)

With lower bound assumption:

$$X_{end,lower} = \int_{t=0}^{T_{end}} \dot{x}(t) dt + \frac{1}{2} v_{A_{initial}} T_{end}$$
(4.43)

In summary, the following calculation procedures are performed during the analytical model predictions:

- Establish the power-law parameters (i.e. strength index K and strain hardening index n) that describe the strain densification regime of the foam material
- Compute initial plastic shock strain $\hat{\varepsilon}_B$, stress enhancement parameter α , characteristic time parameter T
- Evaluate plastic shock strain-time function $\hat{\varepsilon}_B$
- Evaluate shock stress-time function $\sigma(\hat{\epsilon}_B)$ to give shock-induced stresses behind the shock wave front
- Evaluate velocity-time function that describes the motion of debris and crushed material behind the shock wave front. This absolute velocity-time curve can be determined by adding $v_{A_{initial}}$ to the relative velocity-time function. In this respect, it is assumed that the $v_{A_{initial}}$ remains constant over time
- Determine debris penetration distance by finding the area under the velocity(absolute)-time curve
- Similar approach is used to determine the shock wave termination distance

4.3 Analytical Predictions

This section presents predictions of debris penetration into polymeric foam using two analytical models; R-PLH Model and Modified R-PLH Model. The debris-catcher impact scenario to be considered is initiated from the situation whereby the soft-catcher is positioned in close proximity to the concrete wall. The approach to formulate the material constitutive curve for the selected foam type is explained. Eventually, these analytical predictions will then be used to compare with the numerical results in the subsequent chapter. The limitations of the analytical models will also be discussed, which bridge over to the propositions for the numerical simulation work using LS-DYNA.

4.3.1 Impact Scenario of Large Wall Debris

Upon initiation of the explosion, the entire concrete wall break up and launch at relatively same velocity as computed by the Debris Launch Velocity (DLV) formula by Van Doormaal in [20]. The DLV formula is presented below.

$$DLV = C * \sqrt{\frac{NEQ}{v^{\frac{2}{3}}\rho t}}$$
 (4.44)

Where C refers to 525 m/s, NEQ is the charge mass (kg), V is the internal volume of structure (m³), ρ is the density of concrete (kg/m³) and t is the thickness of wall.

The ballistic phenomenon of debris moving at same launch velocity will predominately occur at very close distance to the concrete wall. As the debris cloud expands further, the influence of "small scale flow" will cause the debris with larger masses to move faster than the smaller debris masses. One can refer to the ballistic filtering technique developed by the Klotz Group.

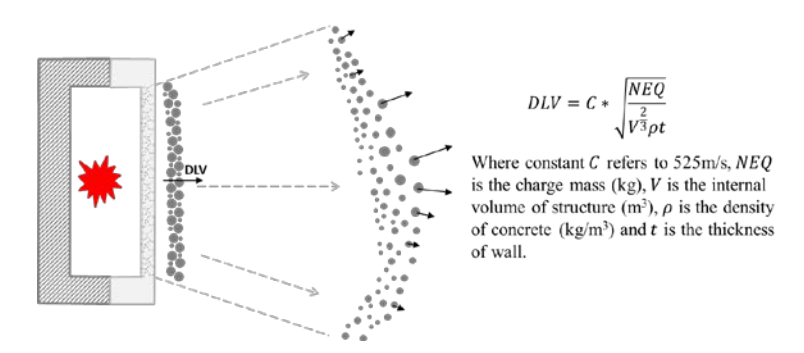


Figure 4-5: Ballistic filtering phenomenon after break-up of concrete wall

Considering the challenges involved in soft-catching debris moving at different velocities, it is therefore preferable to focus on the impact scenario involving the entire concrete wall moving as single debris, which is to say, when the soft-catcher is positioned at a very close distance to the concrete wall specimen.

Figure 4-6 illustrates the elevation view of impact scenario of the large wall debris penetrating and stop within the soft-catcher.

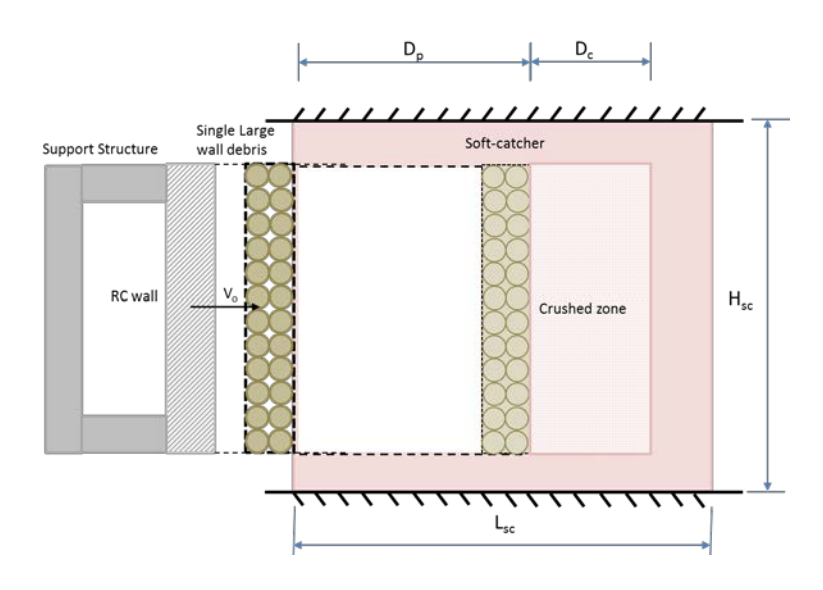


Figure 4-6: Impact scenario of one single large wall debris

The 1D analytical model can be a reasonable approach to predict the debris penetration depth D_p and the crushing depth C_p . This is attributed to the fact that the wave propagation beyond the axial impact direction will not be critical to consider in this particular scenario. Furthermore, the frontal face of the single wall debris remains vertically flat, which is essentially the fundamental assumption in the 1D analytical model. Three debris launch velocities of 50 m/s, 100 m/s and 145 m/s will be considered, in which correspond to the respective loading densities of 1.7 kg/m³, 6.8 kg/m³ and 14.3 kg/m³, using DLV formula. The other input parameters, which are consistent with the KASUN structure (ammunition magazine structure) [21] include: internal structure volume of 8 m³ and wall thickness of 0.15 m. The concrete density is assumed to be 2500 kg/m³.

4.3.2 Predictions based on R-PLH Model

The type of cellular material considered for design of the soft-catcher is the commercially-available structural polymeric foam, Rohacell 110WF, with a nominal density of 110 kg/m 3 . This is a type of closed-cell rigid polymethacrylimide foam. With the aim to provide experimental data for future validation of numerical constitutive models, Arezoo in [22] had investigated the quasi-static mechanical properties of Rohacell foams, with densities ranging from 50 kg/m 3 to 200 kg/m 3 . Table 4-1 presents some of the measured material properties for the 110WF foam.

Material properties	Values	Unit
Relative density, ρ^*/ρ_s	0.078	
Young modulus, E _{compression}	82.5	MPa
Compressive yield stress, σ_{cy}	2.48	MPa
Plateau stress, σ_{pl}	2.36	MPa
Tensile yield strength, σ_{ty}	2.05	MPa

Table 4-1: Material properties of Rohacell 110WF

Figure 4-7 illustrates the quasi-static empirical stress-strain responses of the Rohacell foams with densities of 51 kg/m³, 71 kg/m³ and 110 kg/m³. These responses are obtained under a strain rate of 0.01 s⁻¹.

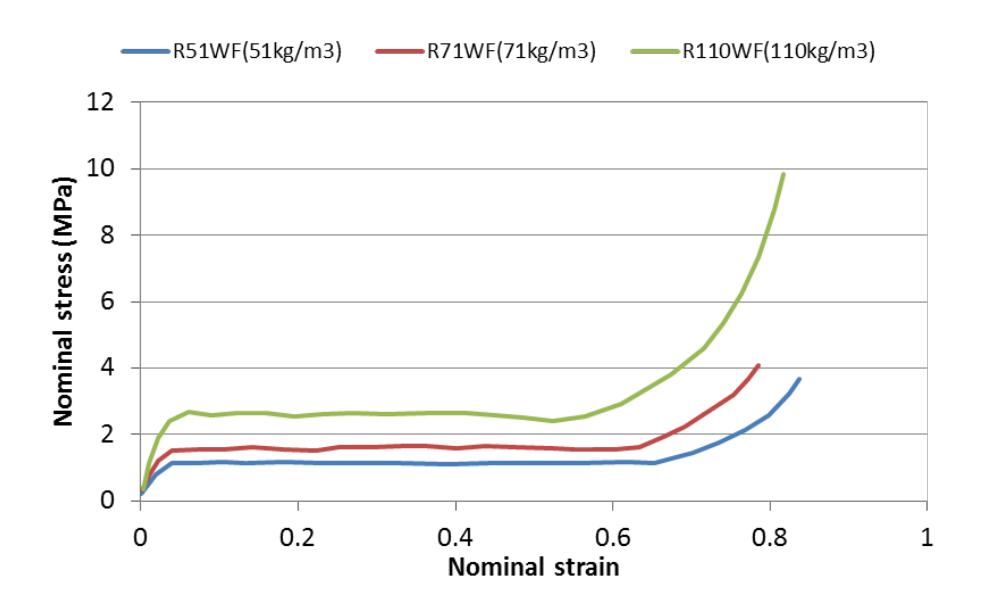


Figure 4-7: Quasi-static stress-strain curves for Rohacell foams with different densities

Observing that the available experimental curves terminate at a rather low stress value, these curves will be further "extended", taking reference with the empirical formulations derived in [4]. According to [4] in formulating a stress-strain diagram for an elasto-plastic foam, the initial elastic regime can be represented based on Hook's Law using plateau stress and Young Modulus. The hardening regime can be constructed using the following formulations:

$$\sigma = \sigma_{pl} \quad for \quad \varepsilon \le \varepsilon_D \left(1 - \frac{1}{D} \right)$$
 (4.45)

$$\sigma = \frac{\sigma_{pl}}{D} \left(\frac{\varepsilon_D}{\varepsilon_D - \varepsilon}\right)^m \quad for \quad \varepsilon > \varepsilon_D \left(1 - \frac{1}{D}\right)$$
 (4.46)

Where

$$\varepsilon_D = 1 - 1.4 \left(\frac{\rho^*}{\rho_s} \right) \tag{4.47}$$

The plateau stress is defined by σ_{pl} , while the densification strain ε_D is the function of the relative density. $\frac{\rho^*}{\rho_s}$ is the relative density, with ρ^* refers to the initial foam density and ρ_s refers to the density of the constituent material that makes up the foam. The parameter D and m were empirically obtained using past available test data for the polymethacrylimide foam, covering a wide range of relative densities (0.028 to 0.155). The D and m can be approximately defined by 2.3 and 1 +/- 0.4 respectively. Hence, using the material properties in Table 4-1, the extended stress-strain curve can be developed accordingly. Figure 4-8

presents the extended stress-strain curve for foam R110WF, in comparison with the experimental curves obtained from [22].

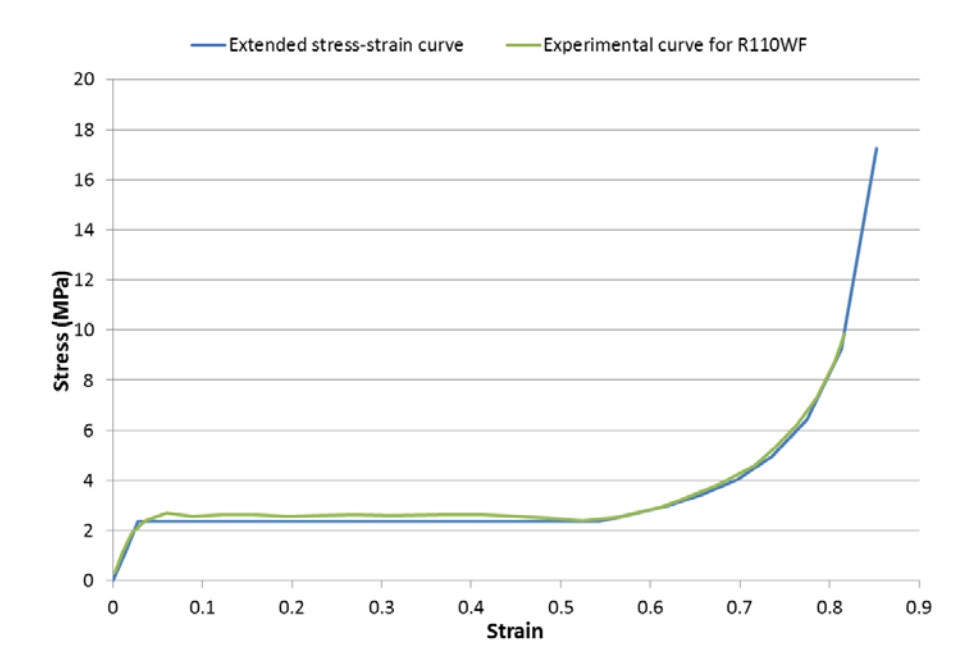


Figure 4-8: Extended stress-strain curve, in comparison with the experimental curve for R110WF

The rigid-power law hardening (R-PLH) analytical model uses power law equation to describe the hardening regime of the foam material which starts at zero strain, while the initial elastic response of the material is ignored. The relevant coefficients (i.e. K and n) that describe the best-fit power law graph to the extended stress-strain curve can be obtained using MS Excel solver. This is presented in Figure 4-9. The hardening regime can be described by the following power-law equation, with the strength index, K and strain hardening index, n to be 118.122 MPa and 13.1 respectively.

$$\sigma = \sigma_{pl} + K\varepsilon^{n}$$

$$\sigma = 2.36 + 118.122\varepsilon^{13.1}$$
(4.48)

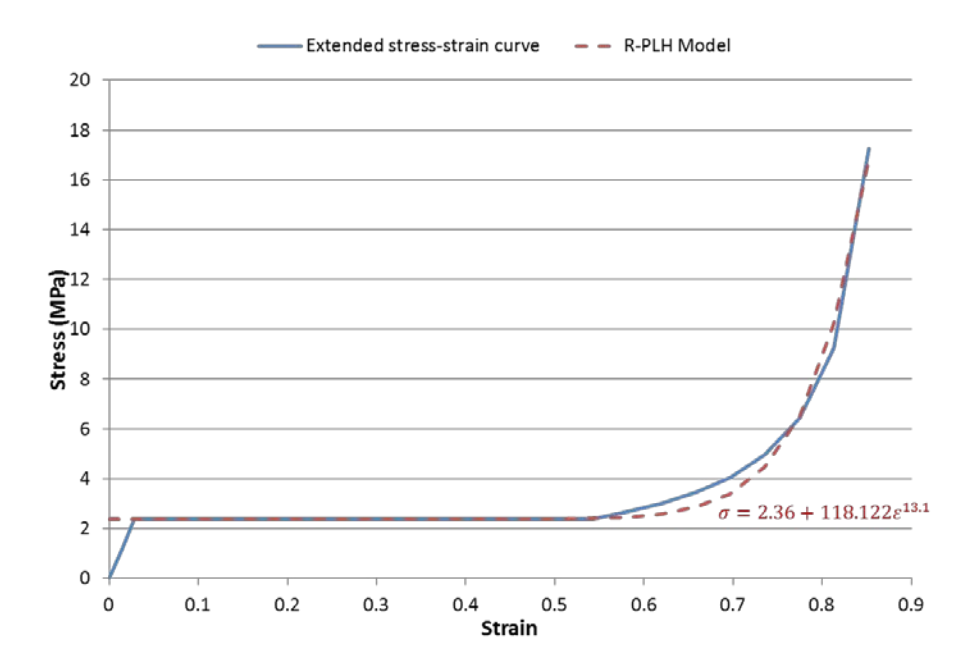


Figure 4-9: Power-law curve (R-PLH model), in comparison with the extended stress-strain curve

Considering the material properties defined for the debris and the soft-catcher, as well as establishing the power-law coefficients for the constitutive relationship of the soft-catcher, the analytical calculations of the debris-soft catcher interactions based on R-PLH model can now be computed using MAPLE program. Table 4-2 presents the input parameters for the R-PLH model.

Input parameters	Value	Unit		
Concrete debris				
Impact Velocity	145	m/s		
Debris density	2500	kg/m3		
Dimension of debris (h x w x t)	1 x 1 x 0.15	m		
Specific mass	375	kg/m ²		
Soft-catcher				
Foam density	110	kg/m ³		
Yielding stress	2.36	MPa		
Strength index, K	118.122	MPa		
Strain hardening index, n	13.1			

Table 4-2: Input parameters for R-PLH model

Under the impact velocity of 145 m/s, the initial shock strain and stress at time t=0 is determined to be 0.7565 and 5.417 MPa respectively. Figure 4-10 shows the strain and stress development over time in the plastic region.

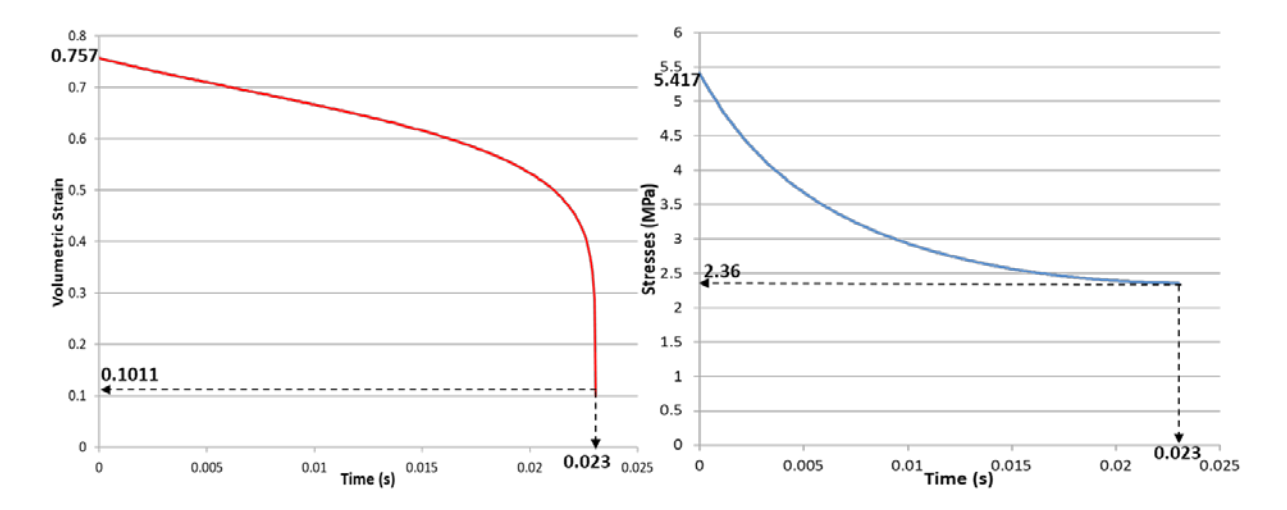


Figure 4-10: Strain and stress development over time

It is worth to highlight that in this analytical model, the shock strains and stresses plotted in Figure 4-10 represent the states for foam material closely behind the plastic shock wave. This model does not evaluate the distribution of strains and stresses over the spatial domain (i.e. the crushed material in between the debris and the plastic wave front). This model assumes that the debris travels at the same velocity with the material particle within the plastic region, which is one of the fundamental principles behind the derivation of motion equation presented in Eq. 4.36. At time t = 0.023 s, also referred as the total time of penetration, the shock strain reduces to a value of 0.1011. This strain value is related to the shock stress by the power law equation that defines the hardening regime. It is to note that in theory, this reduction of shock strain shall eventually reach the yield strain value of 0.0286. However, due to truncation error in the computational process, the lowest strain value obtained is 0.1011. This phenomenon of shock strain reduction is further discussed in the numerical modelling and simulation section. Note that this truncation error is insignificant to influence the debris penetration results and thus, can be ignored.

As anticipated, the decrease in strain will also result in a corresponding decrease in stress along the material constitutive curve. One should note that the stress will decrease until it reaches the plateau stress (i.e. yielding stress) and remains constant thereafter, which is by and large expected. This can be explained by the fact that the stress resistances function comprises the quasi-static term (i.e. plateau stress which is not time-dependent) and the dynamic term (i.e. stress enhancement which is time-dependent). Therefore, at time when the debris penetration terminates, the only term remains in the stress resistance function will be the plateau stress.

The total time of debris penetration can be obtained by evaluating the debris velocity-time function when debris velocity equals to zero. The total time of debris penetration is determined to be 23.04 msec. The total distance of debris penetration can be computed by performing definite integration of the velocity-time function curve, which gives 1.316 m. Similarly, the total distance travelled by the plastic shock wave front within the foam can be computed by taking definite integral of the shock wave velocity-time function curve. The

total distance travelled by the wave front is 1.922 m. It is to note that both the strain and particle velocity of cellular materials in the uncrushed region (i.e. ahead of the plastic wave front) is taken as zero in this R-PLH model. Figure 4-11 compares the velocity-time history plots of the debris and the shock wave front.

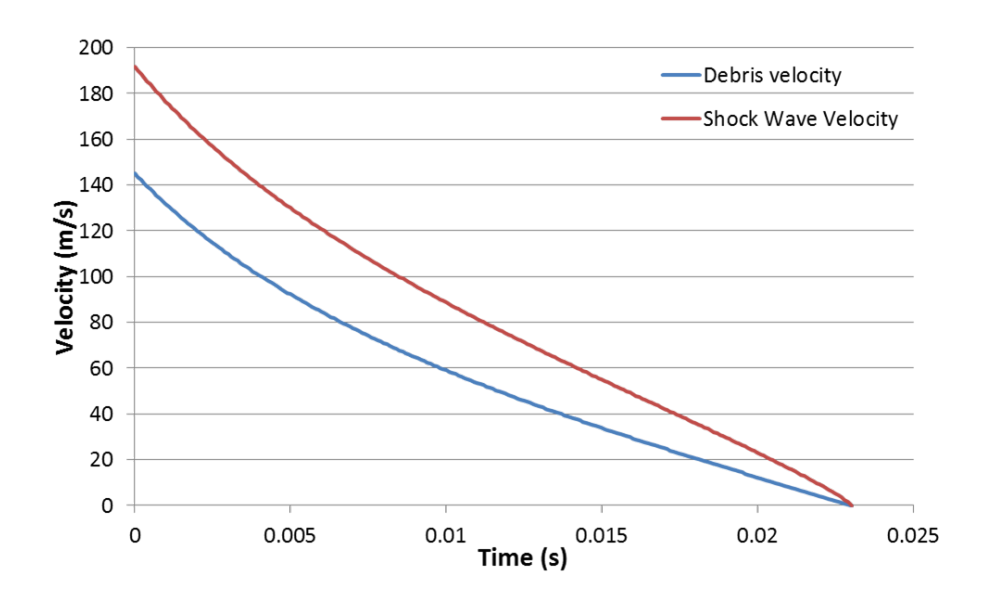


Figure 4-11: Velocity-time plots for debris and shock wave front

Table 4-3 presents the analytical results obtained under three different impact velocities.

Outputs	50m/s	100m/s	145m/s
Initial shock strain	0.651	0.718	0.757
Initial shock stress (MPa)	2.783	3.893	5.417
Total time of penetration (msec)	7.94	15.89	23.04
Debris penetration distance (m)	0.190	0.692	1.316
Shock wave termination distance (m)	0.316	1.054	1.922

Table 4-3: R-PLH Model's predictions obtained under three different impact velocities

4.3.3 Predictions based on Modified R-PLH Model

Essentially, the Modified R-PLH Model considers only the effect of initial elasticity of foam material under this particular 1D impact scenario. The fact that the single wall debris consists of vertical frontal face implies that the shape coefficients (i.e. N₁, N₂ and N*) are all equal to unity. As discussed in the previous sections, this model assumes that the strain and particle velocity of the material ahead of the shock wave front will be non-zero (i.e. equivalent to elastic limit strain and particle velocity corresponds to linear speed of sound for stress wave in medium). As similar to the R-PLH Model, the power law equation is again established to define the hardening regime of the foam material. However, the only difference is that the Modified R-PLH Model considers the hardening regime to start only beyond elastic limit strain. Therefore, these power law coefficients will need to be re-computed again. Figure 4-12

illustrates the best-fit power law curve for the Modified R-PLH Model with strength index, K and strain hardening index, m to be 168.85 MPa and 12.6 respectively.

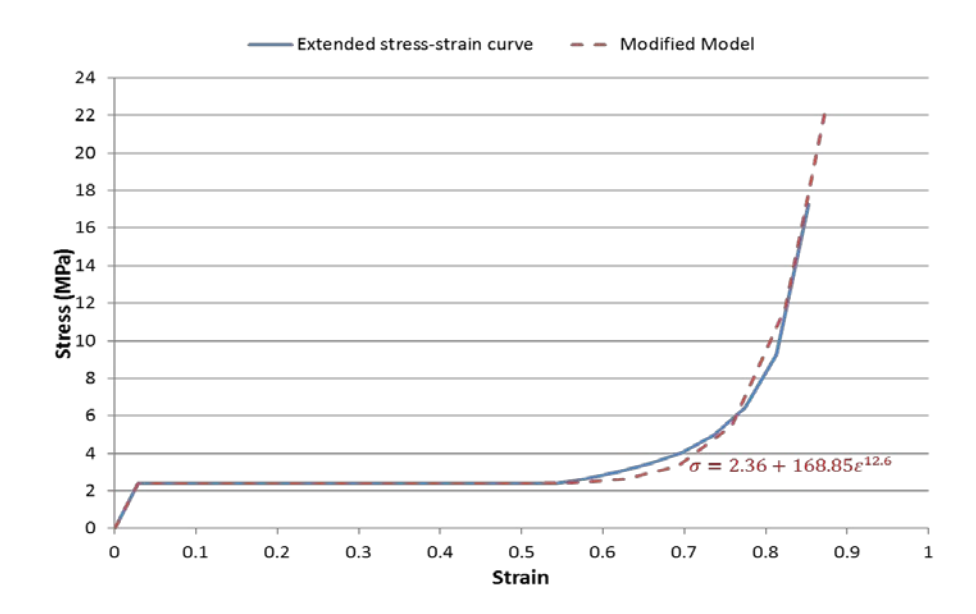


Figure 4-12: Power-law curve (Modified model), in comparison with extended stress-strain curve

Table 4-4 presents the input parameters for the Modified R-PLH Model. The parameters for the concrete debris remain unchanged.

Input parameters	Value	Unit	
Soft-catcher			
Foam density, ρ_o	110	kg/m ³	
Yielding stress, σ_y	2.36	MPa	
Elastic limit strain, ε_y	0.0286		
Strength index, K	168.85	MPa	
Strain hardening index, n	12.6		

Table 4-4: Input parameters for Modified R-PLH model

Under the impact velocity of 145 m/s, the initial shock strain and stress at time t=0 for material directly behind the shock wave front is determined to be 0.7382 (total strain) and 4.6 MPa respectively. Figure 4-13 shows the development of shock strains and stresses over time. The total time of penetration is 0.019 s, giving the corresponding shock strain value of 0.119 and shock stress value of 2.36 MPa.

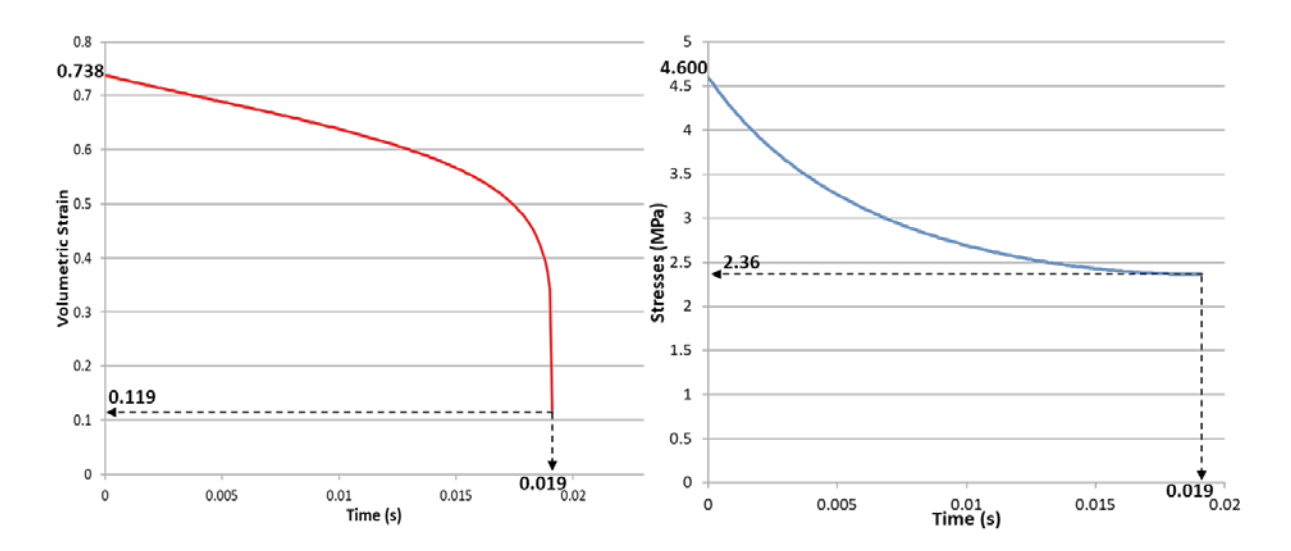


Figure 4-13: Strain and stress development over time for modified model

Considering the initial elastic properties of the foam, the material particle ahead of the plastic shock wave front will be induced with a velocity equivalent to the following expression, where c_1 refers to the linear sound speed of stress wave in the foam. The $v_{A_{initial}}$ is found to be 24.77 m/s, with c_1 being determined as 866.025 m/s.

$$v_{A_{initial}} = \frac{\sigma_{y}}{\rho_{o} c_{1}} \tag{4.49}$$

$$c_1 = \sqrt{\frac{E}{\rho_o}} \tag{4.50}$$

As the formulations of the analytical model are generally derived from Rankine-Hugoniot relationship (i.e. relating jumps in physical quantities of the material across the shock wave front), both the debris and shock wave velocity-time functions are derived relative to the particle velocity in the elastic region (i.e. v_A). Figure 4-14 compares the relative velocity-time history plots of the debris and the shock wave front.

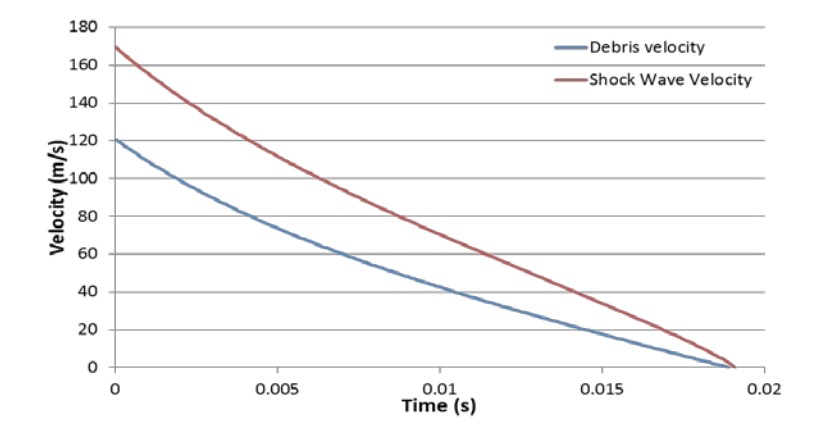


Figure 4-14: Relative velocity-time plots for debris and shock wave front in modified model

The total time of penetration $t=t_{end}$ is determined as 19.1 msec. The distances given by the relative velocity-time functions for debris and shock wave front are 0.951 m and 1.478 m respectively. However, noting that Figure 4-14 depicts the relative velocity-time plots, these distances do not relate to the actual penetration distances. There is henceforth a need to include the additional distance travelled due to the effect of particle velocity v_A . An upper and lower bound approximation of the particle velocity v_A can be considered; upper bound assumes constant v_A throughout the penetration time, while the lower bound assumes v_A to decrease linearly from $v=v_{A_{initial}}$ at time t=0 to v=0 at time $t=t_{end}$. The total penetration time t_{end} is taken as the time for the relative velocity of debris and shock wave front to reach zero.

Therefore, the debris penetration and shock wave termination distance can be respectively obtained as:

The upper bound assumption:

$$D_{debris} = 0.951 + \left(v_{A\ initial}t_{end}\right) \tag{4.51}$$

$$D_{shock\ wave} = 1.478 + \left(v_{A\ initial}t_{end}\right) \tag{4.52}$$

The lower bound assumption:

$$D_{debris} = 0.951 + \frac{1}{2} \left(v_{A_initial} t_{end} \right) \tag{4.53}$$

$$D_{shock\ wave} = 1.478 + \frac{1}{2} \left(v_{A_initial} t_{end} \right) \tag{4.54}$$

Table 4-5 summarized the analytical predictions obtained from the Modified R-PLH model, under three different impact velocities.

Outputs	50m/s	100m/s	145m/s
Initial shock strain	0.564	0.662	0.738
Initial shock stress (MPa)	2.484	3.299	4.6
Total time of penetration (msec)	4.0	11.95	19.1
Debris penetration distance (m)	0.100 (lower)	0.559 (lower)	1.188 (lower)
	0.149 (upper)	0.707 (upper)	1.424 (upper)
Shock wave termination distance (m)	0.145 (lower)	0.824 (lower)	1.715 (lower)
	0.195 (upper)	0.972 (upper)	1.951 (upper)

Table 4-5: Summary of results from Modified R-PLH Model's predictions

4.3.4 Concluding Remarks

The impact scenario between the large wall debris and the soft-catcher (i.e. foam material) is evaluated using both R-PLH Model and Modified R-PLH Model. In total, three different initial impact velocities are assumed. Various responses of foam material due to one-dimensional shock wave propagation are obtained.

Figure 4-15 and Figure 4-16 compares the predictions of absolute debris velocities between the R-PLH Model and Modified R-PLH Model. The predictions from Modified R-PLH Model consist of 2 approaches; "Upper" refers to the assumption of constant particle elastic velocity throughout the penetration time, while "Lower" assumes a linear decrease of particle elastic velocity during the penetration time. It depicts that the Modified R-PLH Model-Upper predicts a slower rate of velocity decrease for the debris under three cases with different impact velocities. Conversely, Modified R-PLH Model-Lower predicts a steeper slope of velocity-time curves for all cases. At this juncture, it is timely to mention that for the Modified R-PLH Model-Upper approach, it is conveniently assumed that upon reaching its predicted penetration termination time (i.e. time equivalent when relative velocity of debris reaches zero), the velocity of debris will drop to zero instantaneously. In the subsequent sections that discuss the numerical analyses, one can appreciate the complexities involved in predicting how the debris terminates its motion upon reaching the particle elastic velocity, in which is closely associated with the propagation of elastic stress waves. Nonetheless, the predictions of both upper and lower bounds of Modified R-PLH Model will be validated with numerical models, in order to determine the right approach.

With the inclusion of non-zero particle velocity induced by the precursor elastic waves, the Modified R-PLH Model predicts lower initial shock strains and stresses for all cases with various impact velocities. This phenomenon seems rational; considering that a foam material with inherent elastic properties will more likely to better attenuate the impact forces coming from the debris impact, as compared to a rigid material.

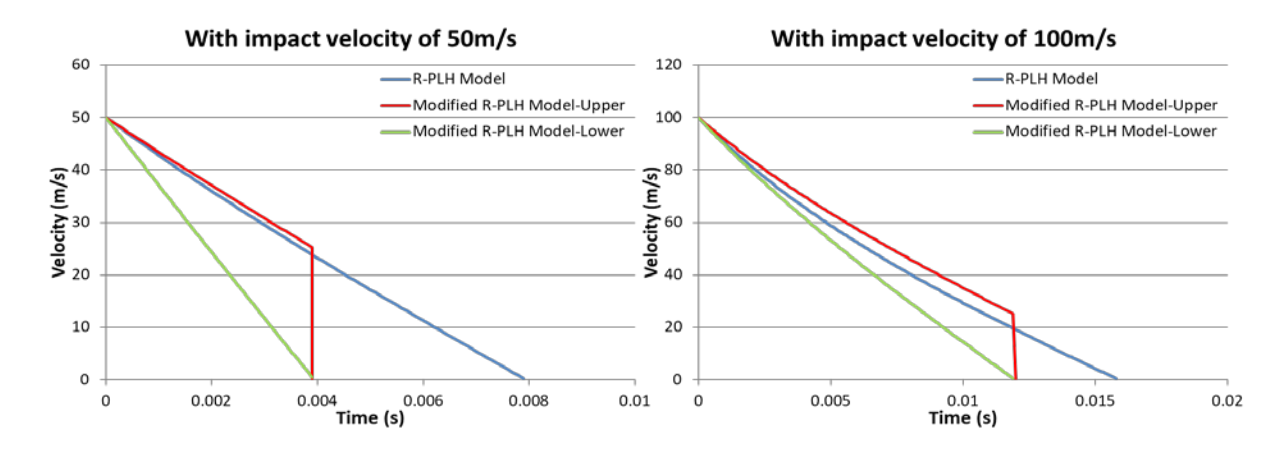


Figure 4-15: Comparison of absolute velocity-time curves of debris between Modified R-PLH and R-PLH Model, under impact velocity of 50m/s and 100m/s

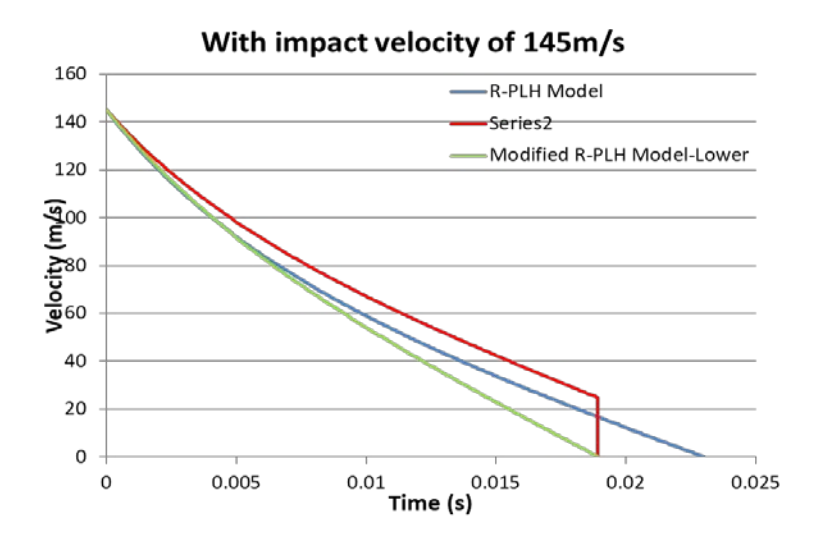


Figure 4-16: Comparison of absolute velocity-time curves of debris between Modified R-PLH and R-PLH Model, under impact velocity of 145m/s

Preliminary Design of Soft-catcher (based on Modified R-PLH Model's Predictions)

From these analytical results, it is apparent to establish a preliminary design length of 2m for the soft-catcher, based on the shock wave termination distance computed with debris launch velocity of 145 m/s. The shock wave termination distance essentially consists of the debris penetration distance and the material crushing length ahead of the debris. The impact stresses acting on the debris are evaluated based on the initial shock stress at time t=0. The highest initial shock stress of 4.6 MPa is observed for the case when debris launch velocity is 145 m/s. This shock stress is about 13.1% of concrete compressive strength, considering the design strength of 35 MPa. As one prerequisite to ensure no additional damage to debris during soft-catching process, the maximum induced shock stress shall preferably be less than say 20% of the concrete compressive strength.

Finally, before moving on to the numerical modelling and simulation, it is worthwhile to highlight various assumptions made in the Modified R-PLH Model:

- single rigid debris impact
- 1D shock wave propagation (i.e. no radial expansion of shock wave) ignoring the pre-stressing of cellular material beyond the axial impact direction
- homogeneity of material properties in the direction of impact (multiple, or graded foams not considered)
- infinite thickness of cellular material (the reflection of plastic/elastic waves through graded foam is not taken into account)
- material reaches yielding stress and strain, and subjects to particle velocity $v_{A_{initial}}$ when elastic wave passes through
- uniform distribution of shock stresses within crushed (plastic) zone
- same velocity for debris and crushed particle in plastic zone
- abrupt termination of $v_{A_{initial}}$ when shock wave ceases

In which, the validity and consequences of the assumptions in *italic* are verified through 1D numerical analyses (See Section 5.3).

5 Numerical Simulation

LS-DYNA is one of the commonly used advanced numerical FE codes to model and simulate responses of material under non-linear dynamic events, such as impact problems, crush scenarios or explosive events. Contact interface modelling, which is a major characteristic in this thesis work, is one of the unique capabilities in LS-DYNA. LS-PrePost will be used as pre- and postprocessor tool.

This chapter firstly discusses the approaches to perform 1D numerical modelling and simulation to validate the analytical model predictions obtained from the previous chapter. The quasi-static responses of the chosen material model will be validated through material cell test. Shock stresses, strains, particle velocity and shock wave propagation within the soft-catcher as a function of time will be evaluated in an impactor-target scenario. This is then followed by propagating 1D numerical models into 2D domain, in which material failure characteristics are taken into consideration. Relevant outputs (e.g. shock stresses, support reaction forces) from the 2D numerical analyses will be presented for future detailed design of soft-catcher. Lastly, a sensitivity study will be performed to appreciate the influence of certain material properties of the soft-catcher on its overall response.

5.1 Validations of Material Models

The quasi-static material cell test is performed using explicit solver in LS-DYNA. The Lagrangian solid elements (eight-node solid element) with ELFORM = EQ. 1 (underintegrated constant stress solid element) is used to model the cell. The two material models to consider are the: Material Model 63, MAT_CRUSHABLE_FOAM and Material Model 18, MAT_POWER_LAW_PLASTICITY. The aim of the material cell test is to examine and validate the material responses under compressive and tensile loading. Thereafter, conclusions will be drawn to recommend the appropriate material model for subsequent numerical modelling. Figure 5-1 shows the single brick element constructed for the cell test.

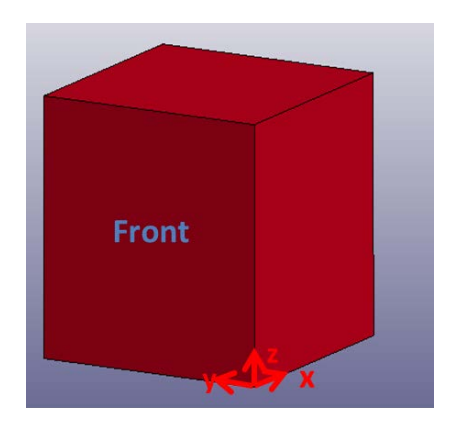


Figure 5-1: Single brick (1-point integration) element for cell test

The adopted consistent units in the model are m, kg, s and Pa. The dimension of the cell is 1 m by 1 m by 1 m.

5.1.1 MAT_63: CRUSHABLE FOAM

MAT_CRUSHABLE_FOAM (material model MAT_63) is an isotropic crushable foam model that responds mainly in one-dimensional manner. The tensile behaviour assumes a perfectly-plastic response with a user-defined tensile cut-off stress value. The unloading is assumed to be elastic, which will reach this cut-off stress value, before reloading to follow the material's stress-strain curve. The material compressive constitutive relationship, in the form of stress versus volumetric strain, will be incorporated by user via DEFINE_CURVE card. The volumetric strain γ is defined as 1 minus relative volume V, as shown in the following expression. The relative volume refers to the ratio of the current volume over the initial volume of the element.

$$\gamma = 1 - V \tag{5.1}$$

The effective plastic strain obtained from the LS-DYNA output is defined as the integrated volumetric strain, which is the natural logarithm of the relative volume.

The material model constitutive curve is illustrated in Figure 5-2, which is plotted directly from Figure 4-12 in previous section.

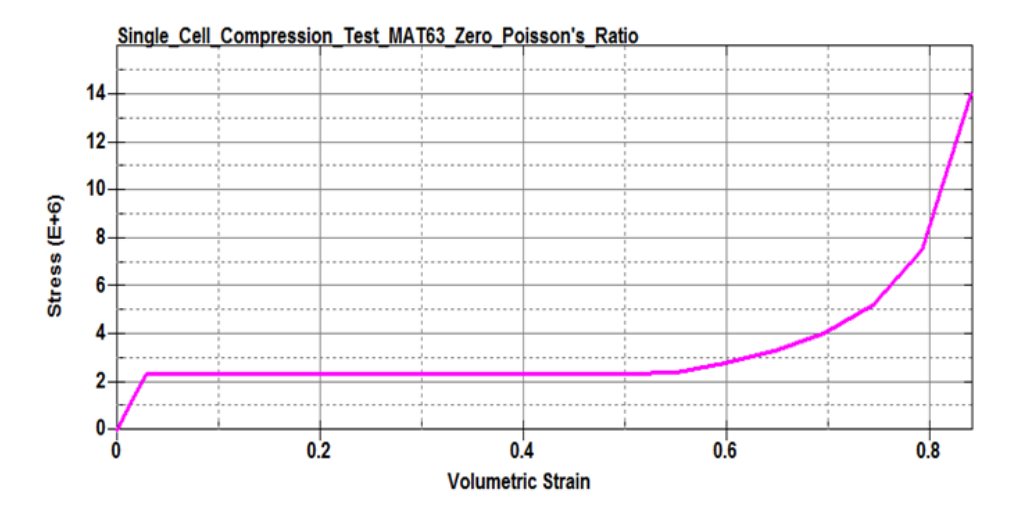


Figure 5-2: Material constitutive curve defined in LS-DYNA

The input parameters for the material model are tabulated below:

Input parameters	Value	Unit
Density (RO)	110	kg/m ³
Elasticity (E)	82.5	MPa
Poisson's Ratio (PR)	0	
Tensile stress cut-off (TSC)	2.05	MPa
Damping	0.1	

Table 5-1: Input parameters for MAT_63 Crushable Foam

The bottom corners of the element will have the translational restraints being defined as shown in Figure 5-3, using BOUNDARY_SPC_SET card. Hourglass control type 6 (Belytschko-Bindeman), which is mandatory for explicit analysis, is assigned for the solid element.

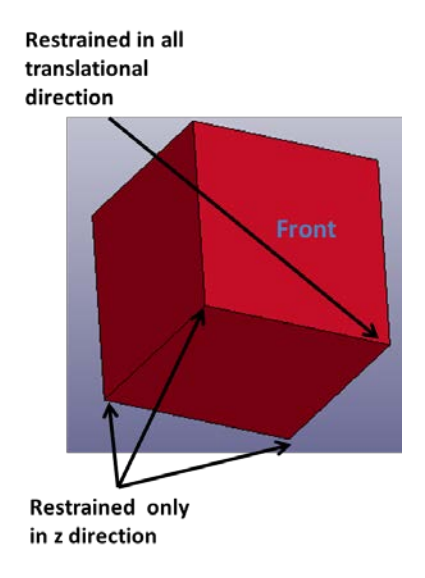


Figure 5-3: Boundary conditions for the cell test

5.1.1.1 Compressive Loading Test

The compressive loading to the element is applied via PRESCRIBED_MOTION_SET. The top four nodes are assigned with prescribed displacement at approximated loading rate of 0.01m/s, which is consistent with the experimental stress-strain curve being considered for the material. Figure 5-4 shows the prescribed displacement loading curve.

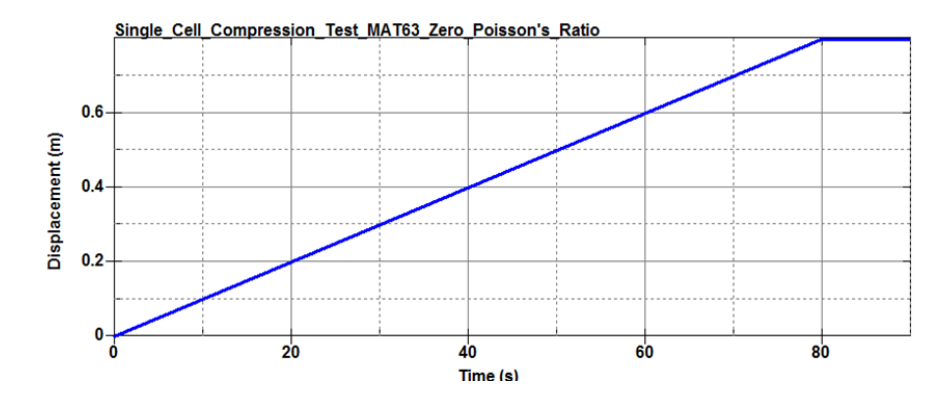


Figure 5-4: Prescribed displacement loading curve for compressive load test

Figure 5-5 and Figure 5-6 show the time-history plots for effective stress and plastic strain for the element under compressive loading.

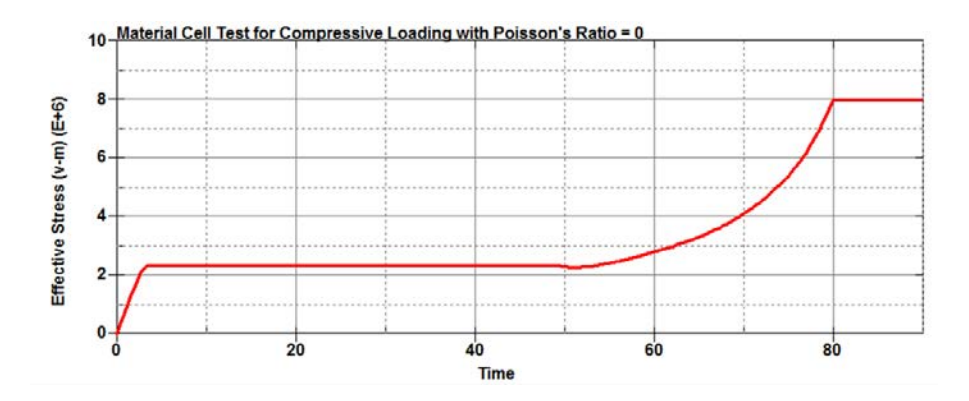


Figure 5-5: Effective stress-time history plot for MAT_63 under compressive loading

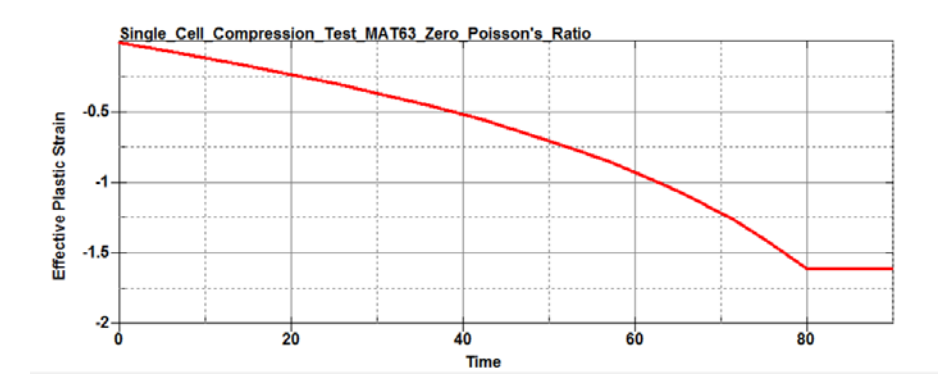


Figure 5-6: Effective plastic strain-time history plot for MAT_63 under compressive loading

The effective plastic strain shown in Figure 5-6 is used to compute the equivalent volumetric strain. Figure 5-7 shows the effective stress vs volumetric strain output curve obtained from the compressive loading test, overlaid with the material's constitutive curve (defined as input in MAT_63). It can be evidently seen that the response of MAT_63 under compressive loading correlates very well with the material's constitutive curve.

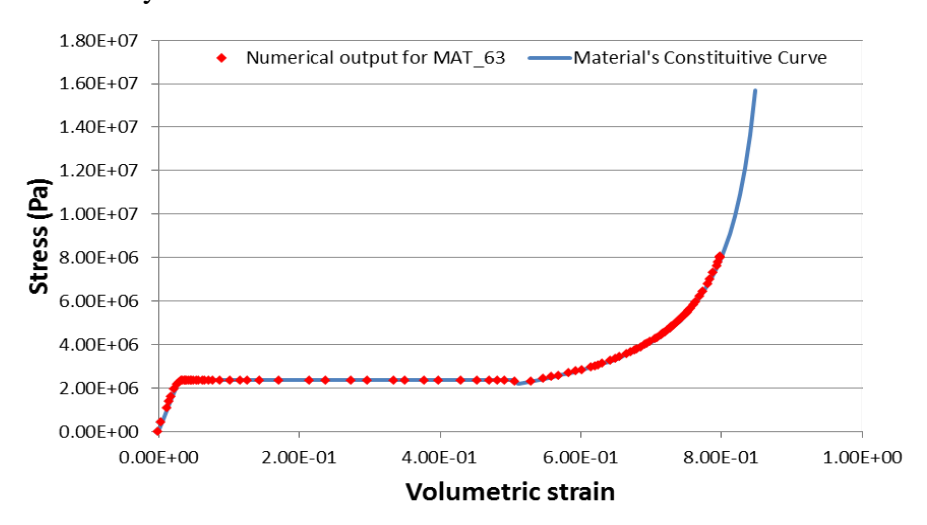


Figure 5-7: Effective stress vs volumetric strain curve for MAT_63 under compressive loading

The effect of increase in Poisson's Ratio (PR) of up to 0.3 on the material response to compressive loading is also examined. With the increase in Poisson's Ratio, it is expected that the relative volume (i.e. current over initial volume) will increase. Therefore, the effective plastic strains and stresses will reduce, as compared to the model with zero Poisson's Ratio. In order to obtain adequate numerical results in the hardening regime, the prescribed displacement load curves for model with PR of 0.15 and PR of 0.3 are proposed as follows:

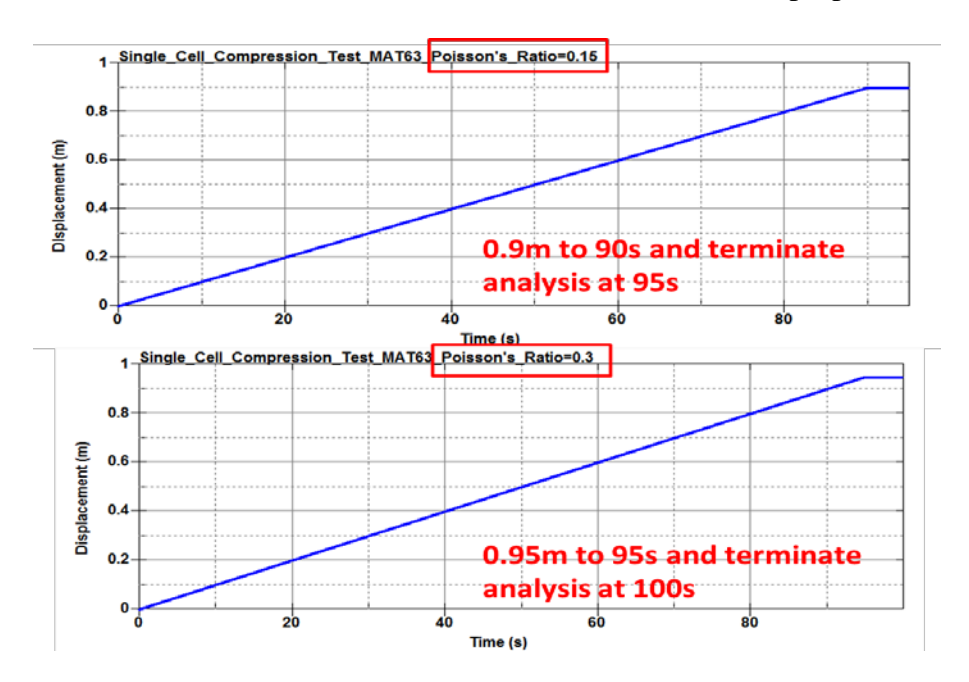


Figure 5-8: Prescribed loading curve for model with PR=0.15 and 0.3 respectively

Figure 5-9 shows the effective stress vs volumetric strain curves from the various models with different Poisson's Ratio. It can be seen that the material responses remain unaffected by the change in Poisson's Ratio.

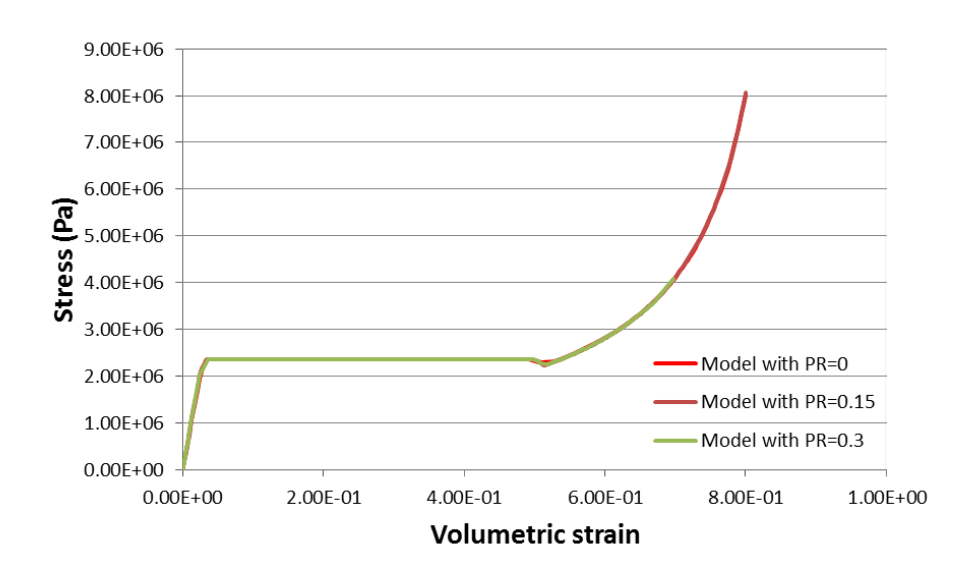


Figure 5-9: Effective stress vs volumetric strain plots for models with various Poisson's Ratio

Figure 5-10 shows the stress vs volumetric strain curves from the various models subjected to different applied loading rate. These loading rate ranges from 0.001 m/s to 145 m/s. The left plot of Figure 5-10 illustrates noticeable increases in stresses when the loading rate exceeds 1m/s, which implies that the material model is strain rate-sensitive. Furthermore, it appears that the numerical analyses with higher loading rates generate steeper slope of stress-strain curves within the elastic regime, as compared to the material model input curve. The red plot indicates the material's constitutive curve (set as input curve in the numerical analyses). The right plot of Figure 5-10 amplifies the stress-strain responses near the elastic limit. It is clearly seen that the elastic limit strains obtained from all the numerical models, even for the case with lowest loading rate of 0.001 m/s, are apparently higher (i.e. about 0.034) than the material's pre-defined elastic strain of 0.0286. The elastic limit strain for models with loading rate higher than LR10 (i.e. LR10 refers to loading rate of 10m/s) is approximately 0.0343.

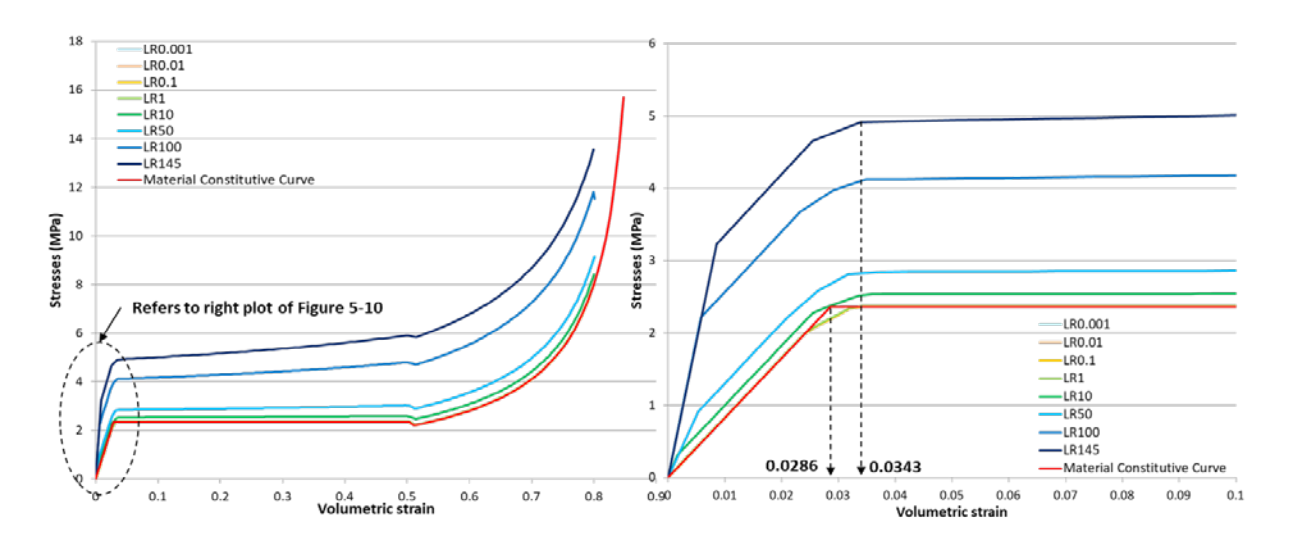


Figure 5-10: Stress vs volumetric strain plots for models with different loading rate (m/s)

5.1.1.2 Tensile Loading Test

Similar to the compressive loading test, the tensile loading test is performed using prescribed displacement loading applied to the top nodal points with the same loading rate of 0.01 s⁻¹, via PRESCRIBED_MOTION_SET. Figure 5-11 shows the prescribed displacement loading curve.

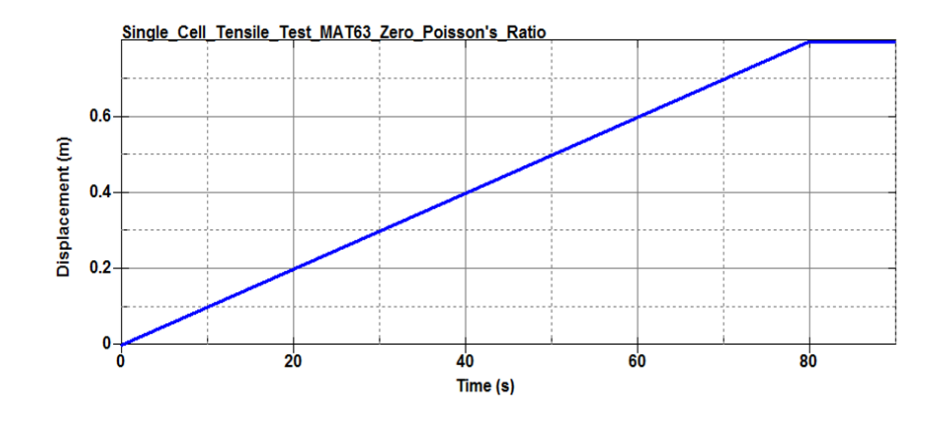


Figure 5-11: Prescribed displacement loading curve for tensile loading test

Figure 5-12 shows the effective stress vs volumetric strain for the element under tensile loading, in comparison with the theoretical plot of tensile behaviour (i.e. tensile cut-off stress with perfectly-plastic response beyond elastic strain limit). The theoretical plot is determined based on elasticity of 82.5 MPa and tensile strength of 2.05 MPa for the foam material. It is clearly illustrated that the elastic strain values obtained from the numerical models under tensile loading are much lower than the elastic strain value derived theoretically.

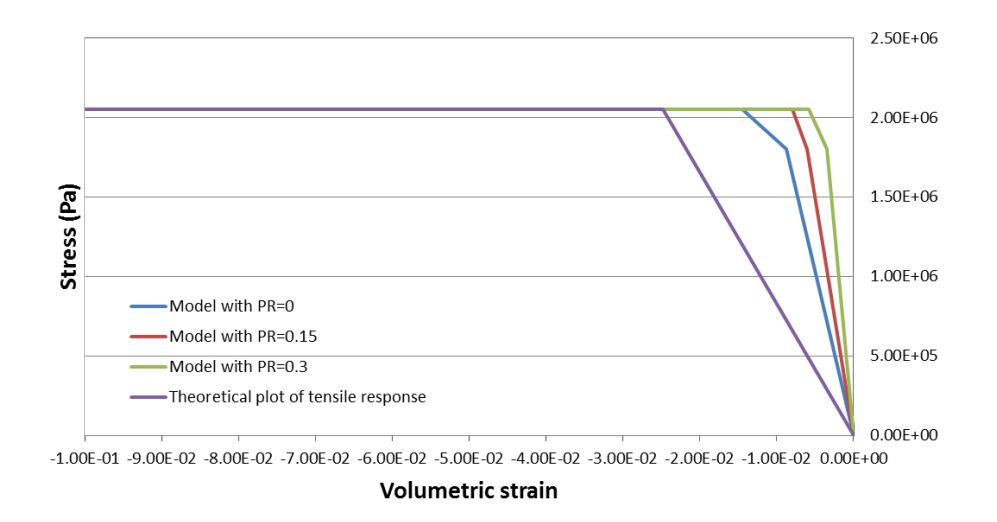


Figure 5-12: Effective stress vs volumetric strain curves for models with different Poisson's Ratio for MAT 63 under tensile loading

5.1.2 MAT_18: POWER LAW PLASTICITY

This material model considers elasto-plastic behaviour with isotropic hardening and uses power law coefficients (i.e. strength coefficient and hardening exponent) to define the hardening regime. This material model is commonly used for metal or plastic forming analysis.

Figure 5-13 shows the input parameters defined for the material model. A compressive loading is applied to the element using the same prescribed displacement loading as before. The strength index, K and hardening index, N for the MAT_18 are obtained directly from the respective strength index (118.12 MPa) and hardening index (13.1) used in analytical model (R-PLH model).

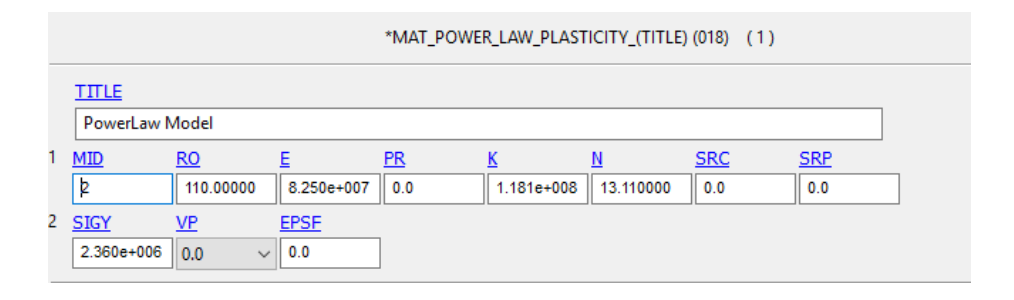


Figure 5-13: Input parameters for MAT_18

Figure 5-14 presents the output effective stress vs plastic strain curve. Considering elastic yield strain of 0.0286 (i.e. E_{input}/σ_y), the plastic strain of 0.2 corresponds to an effective stress of about 53.8 MPa, as shown from the LS Dyna output. However, the original constitutive curve shows that the material is still within the stress plateau region with a plastic strain of 0.2, as illustrated in Figure 5-15.

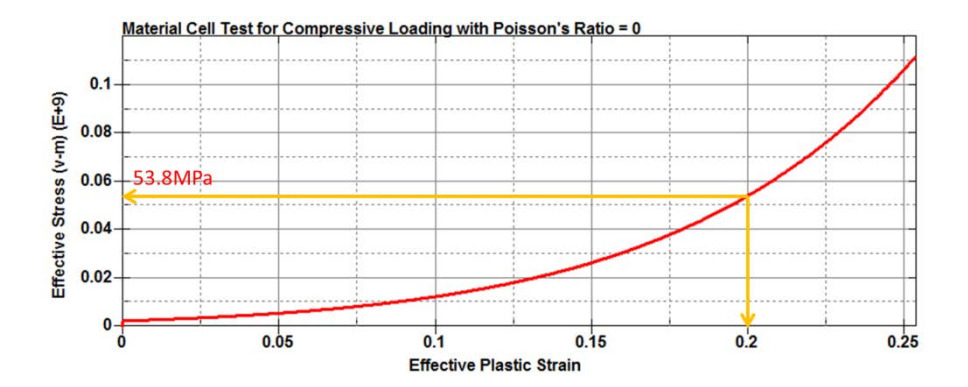


Figure 5-14: Effective stress vs plastic strain plot for MAT_18

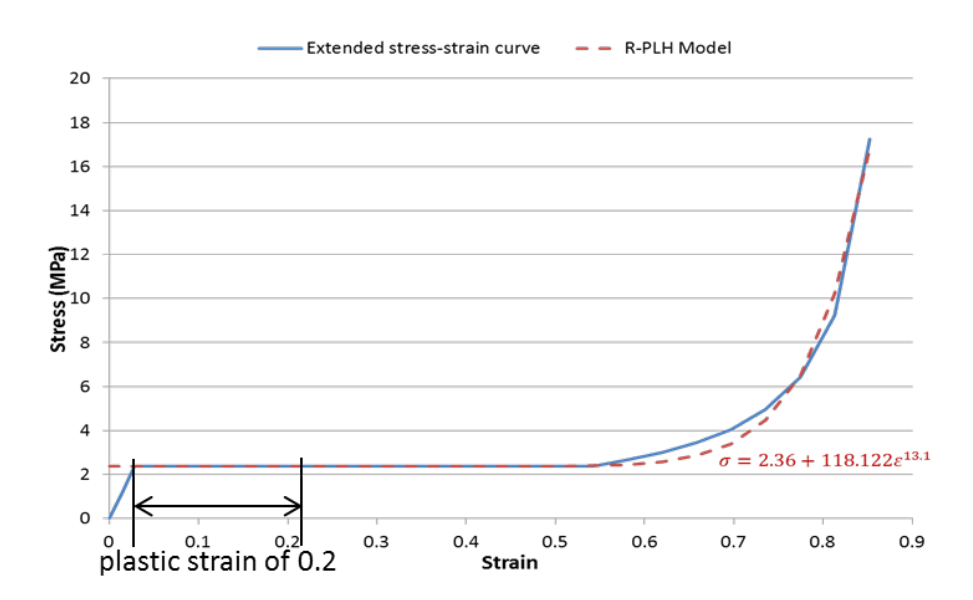


Figure 5-15: Original constitutive curve for foam material

5.1.3 Concluding Remarks

The material model MAT_18 presents a less straightforward mean to calibrate the material constitutive curve. The output compressive stress-strain curve obtained does not illustrate a distinct "stress plateau region" beyond the initial elasticity, which deviates from one of the key material characteristics for the rigid plastic foam in consideration.

In contrast, the use of material model MAT_63 CRUSHABLE FOAM for compression loading yields consistent results as compared with the user-defined material constitutive relationship. Apparently, the increase in Poisson's Ratio up to 0.3 does not influence the material response. This material model does automatically account for the effect of strain rate by default, yet there are no means for user to input any strain rate parameters. The material

response under tensile loading appears to be less favourable than under compressive loading, given that the elastic limit tensile strains do not relate well with the theoretical value.

In conclusion, the direct use of stress vs volumetric strain curve obtained from material properties as an input curve in MAT_63 provides a relatively easy and accurate mean to calibrate the numerical model's constitutive response. Furthermore, the material model responds well with the user-defined constitutive relationship, especially under compressive loading, which is the main loading phenomenon in the subsequent impact scenario problem. Therefore, MAT_63 will be chosen as the material model for the soft-catcher.

5.2 Numerical Modelling

This section briefly discusses the various key input deck cards utilized for the running of numerical analyses. LS-PREPOST is the selected tool for creating the geometry and boundary conditions of the models, as well as post-processing the simulation results.

5.2.1 General Modelling Information

The adopted consistent units for this model are m, kg, s and Pa. Both the impactor and target are modelled using solid constant stress elements with single integration point (i.e. element formulation type: ELFORM 1). The use of under-integrated solid elements generally lowers computational cost. In severe deformation problem, using under-integration elements can be more stable in terms of avoiding error termination due to negative Jacobian at integration point, as compared to using fully-integrated solid elements. Furthermore, the fact that the foam material has negligible Poisson's Ratio eliminates the option of using fully-integrated solid elements. However, in order to avoid the occurrence of negative volume errors in soft material, HOURGLASS control is incorporated with formulation type 2 (Flanagan-Belytschko viscous form), as recommended (by LS-DYNA online support).

The definitions of the appropriate boundary conditions for the impactor and the target are incorporated via BOUNDARY_SPC_SET card. No rotational restraints are assigned to the target model.

The velocities of impactor considered in the numerical simulation include 50 m/s, 100 m/s and 145 m/s (See Section 4.3.1), which are incorporated using INITIAL_VELOCITY card. This card assigns the user-defined velocity to all nodal points of the impactor model.

LS-DYNA automatically computes the required new timestep. In the CONTROL_TIMESTEP card, there is an option to adjust the timestep factor (TSSFAC), which is used to scale the critical timestep. In order to avoid numerical instabilities, as well as eliminating contact penetration errors when higher impact velocities are involved, this timestep factor is further reduced from the default value of 0.9 to 0.1, though the time taken to complete the analysis will increase.

The rigid impactor is modelled using MAT_20 (RIGID) while the foam target is modelled using MAT_63 (CRUSHABLE FOAM).

5.2.2 Formulation of Contact Type

Interactions between different entities or parts in the numerical model can be effectively addressed by incorporating relevant contact option and parameters. The prediction capability of the numerical model largely depends on the modelling accuracy of the contact interface. Contact forces are determined when segments or nodes of one entity penetrate into segments of another entity. The selected method of computing contact forces are the penalty-based approach, which is commonly used for its stability.

In this impactor-target problem, CONTACT_AUTOMATIC_SURFACE_TO_SURFACE is selected as the contact type option, considering that the contact area between the impactor and target is relatively large. It is also preferable to use segment-based contact since the interaction between impactor and target involves sharp corners. Note that in using surface to surface contact type, the selection of slave and master component in the CONTACT card is not critical, though in the problem, the impactor is defined as the slave while the target is the master. It is worth to highlight that during the analysis, LS-DYNA automatically adjusted the slave and master interface stiffness in the CONTACT card from the default value of 1.0 as follows: Scale factor on slave penalty stiffness SFS = 0.1 and master penalty stiffness SFM = 10. This is mainly attributed to the significant difference in the material stiffness between concrete and foam.

With the target being considered as a type of soft material (crushable foam), large deformations under moderate to high impact velocity will likely cause error termination due to negative volumes and/or element inversion. To avoid such errors, CONTACT_INTERIOR card with crush activation thickness factor of 0.1 (default) and contact interior type 1 (i.e. for uniform compression) are assigned for the foam target. The crush activation thickness defines the fraction of the initial element thickness in which if the current element thickness falls below this value, the internal contact treatment will be activated to avoid mesh tangling. In addition, an optional card (SOFT=2), which is for segment-based contact, is activated in the CONTACT card, as recommended for contact interface involving soft materials such as foam material. The conventional approach of detecting node penetration into segment and computing penalty forces based on global material stiffness increases the likelihood of numerical instabilities in contact interface of soft materials. The SOFT option computes local spring stiffness based on nodal masses and initial timestep.

Finally, the set of input cards required for the numerical analysis include the followings:

CONTROL_TERMINATION
CONTROL_TIMESTEP
DATABASE_BINARY_D3PLOT
BOUNDARY_SPC_SET
SET_NODE
CONTACT_AUTO_SURFACE_TO_SURFACE
CONTACT_INTERIOR
PART
SECTION_SOLID
MAT_RIGID
MAT_CRUSHABLE FOAM
HOURGLASS

INITIAL_VELOCITY
ELEMENT_SOLID
NODE
SET_PART_COLUMN

5.3 Model of 20m Target Length - Validations of 1D Analytical Models

The main objective of this section is to the validate the 1D analytical model predictions, in particular the debris velocity, material shock stress and strain development over time domain, and the shock wave propagation phenomenon. Therefore, numerical models are developed in one-dimensional aspect. Figure 5-16 illustrates the numerical model developed for the 1D impactor-target problem.

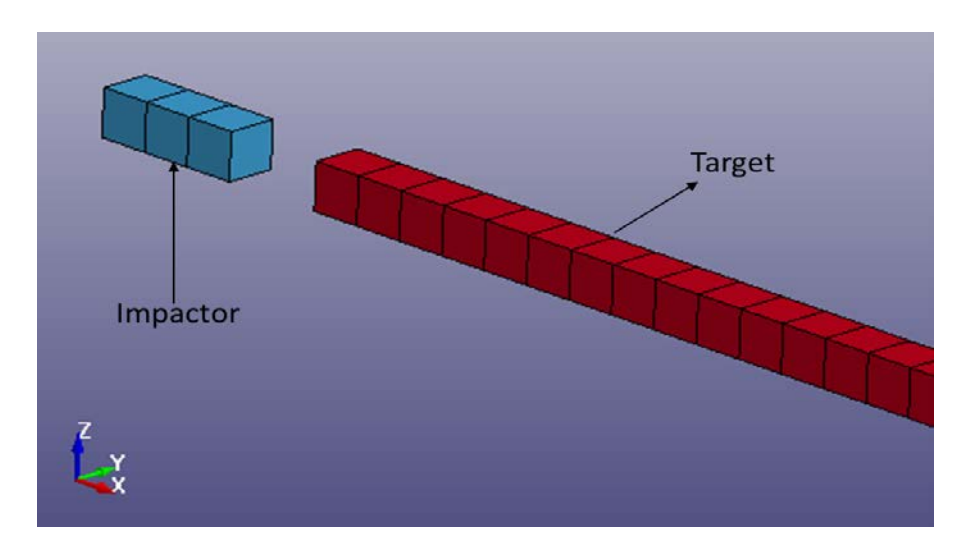


Figure 5-16: Numerical model for 1D impactor-target problem

It can be seen that the 1D numerical model best-represents the response of materials at the centre part of the debris-soft catcher scenario. Consistent to the impact scenario presented in the analytical model prediction, the thickness of impactor is set at 0.15 m, which gives a specific mass of 375 kg/m². The boundary conditions of the model are illustrated in Figure 5-16 and Table 5-2. No rotational restraints are defined.

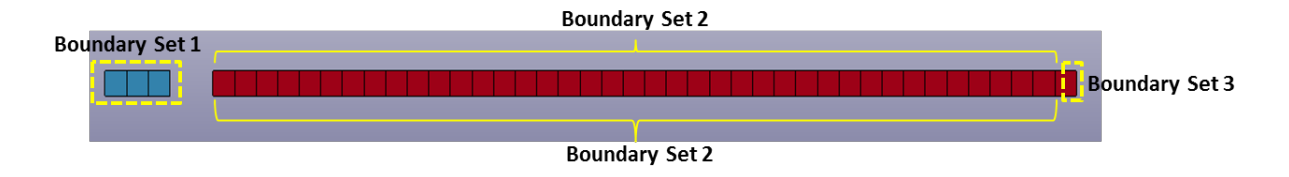


Figure 5-17: Boundary conditions for the 1D numerical model

Boundary Set	Translational restraints		
Option (1)	X	Υ	Z
1	No	Yes	Yes
2	No	Yes	Yes
3	Yes	Yes	Yes

Table 5-2: Translational restraints specified for the boundary sets

5.3.1 Velocity-Time History of Impactor

The velocity-time history of nodal point 1 of the impactor are extracted from numerical analyses of different target lengths and plotted in Figure 5-18. The element size considered is 0.050 m.

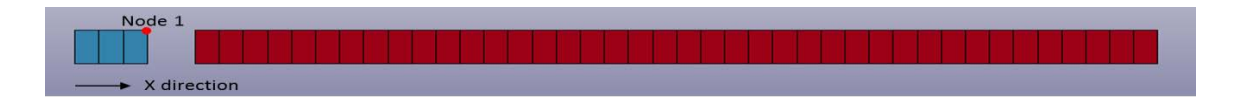


Figure 5-18: Nodal point 1 of the impactor

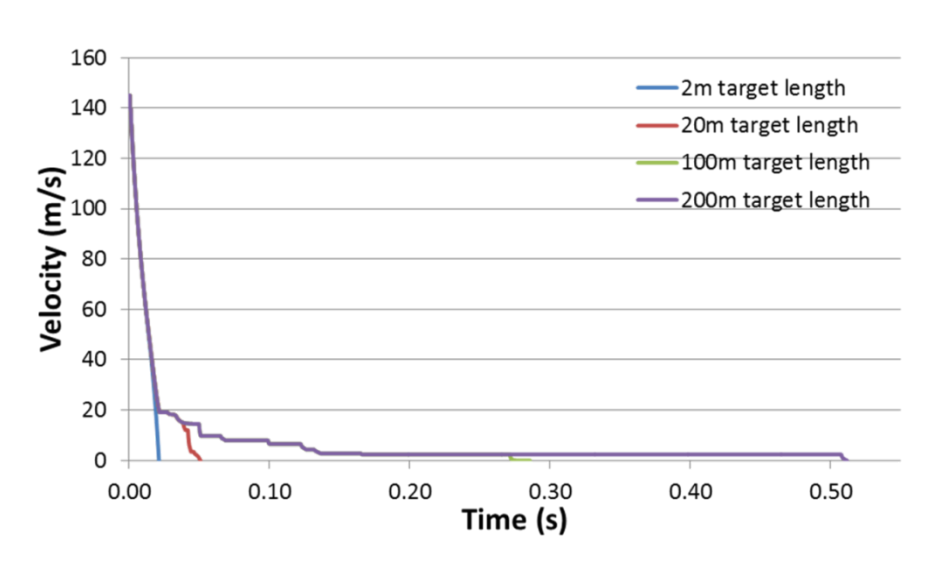


Figure 5-19: Velocity-time curves of impactor's nodal point 1 with different target lengths for 145 m/s

With the initial impact velocity set at 145 m/s, Figure 5-19 shows that the velocity rate of the impactor at initial phase (i.e. before reaching near the initial particle velocity due to linear sound speed of stress wave in material, $v_{A_{initial}}$ as reported in the analytical prediction report) for models of 20 m, 100 m and 200 m target length show consistencies in the decreasing velocity rate. The $v_{A_{initial}}$ for the target material is found to be about 24.77 m/s. Beyond this initial velocity phase, the time taken for the impactor to reach zero velocity increases as the target length increases. This is by and large expected as one can imagine applying a same compressive load to a series of linear spring system with different lengths. An increase in spring length will result a corresponding increase in translational displacement. Further investigations on this phenomenon are presented in the later section.

In view that the analytical prediction approach does not account for finite thickness of the target, it is henceforth preferable to consider the numerical model with 20 m target length for the purpose of validating the analytical model predictions. This is especially so when the next few sections generally focus on validating the responses of target in the initial velocity regime (i.e. before reaching $v_{A_{initial}}$), and that models with 20 m, 100 m and 200 m target length show consistent deceleration in this velocity regime. In addition, the effect of target's end boundary on plastic wave propagation can be avoided.

Figure 5-20 shows the velocity-time curves for the numerical models of 20 m target length (20mTL) with three different element sizes; 0.050 m, 0.025 m and 0.010 m. These are compared with the analytical model predictions. Unlike R-PLH Model, the Modified R-PLH Model considers the influence of elastic properties of the foam material, though only the effect of incident elastic wave propagation on the material is incorporated. The Modified R-PLH Model_1 assumes constant $v_{A_{initial}}$ for particle velocity due to elastic precursor wave throughout the impact duration; while the Modified R-PLH Model_2 assumes $v_{A_{initial}}$ to decrease linearly from t=0 to t= T_{end} . The T_{end} refers to the time taken for difference between the plastic wave front velocity and the debris (or impactor) velocity to reach zero.

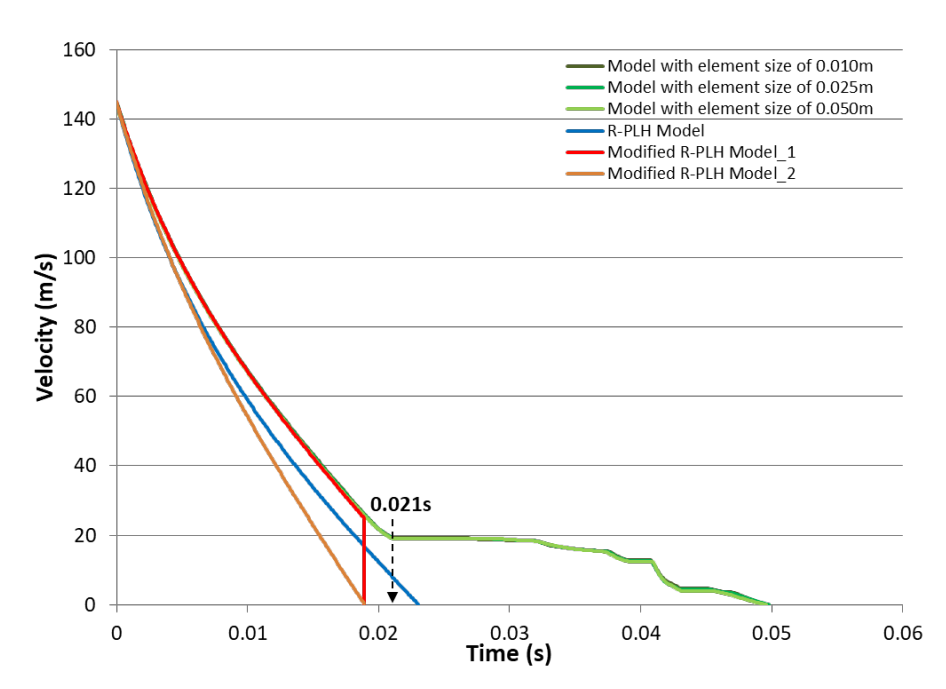


Figure 5-20: Velocity-time curves of 20mTL models with analytical predictions for 145 m/s

All three models with different element sizes show identical decreasing velocity rate of impactor with initial impact velocity of 145 m/s. It is apparent to recognize that the Modified R-PLH Model_1 relates well with the numerical models, up to velocity near $v_{A_{initial}}$, as the analytical model is unable to further evaluate the deceleration of the impactor below $v_{A_{initial}}$. Both R-PLH Model and Modified R-PLH Model_2 predicted steeper deceleration of the impactor. The sudden change in the rate of velocity is observed at approximately time t=0.021 s.

5.3.2 Effective Stress-Time History of Target

The effective stress-time histories of elements within 2 m from the impact end are evaluated and compared with analytical models. For the purpose of validation, only the stress states within selected time frame (i.e. from t=0, to the total time of penetration, t= T_{end} determined from analytical model predictions) will be considered. The T_{end} obtained from the analytical predictions of R-PLH Model and Modified R-PLH Model, for an initial impact velocity of 145 m/s, are 0.023 s and 0.019 s respectively. The larger value (i.e. 0.023 s) will be considered. The numerical results will be compared with the shock stress-time function derived from the 1D analytical models; R-PLH Model (w/o elasticity) and Modified R-PLH Model (with elasticity and constant initial particle velocity, $v_{Ainitial}$).

Figure 5-21 shows the shock stress-time function of target material closely behind the plastic wave front evaluated from the analytical models, with an initial impact velocity of 145 m/s. It is observed that with the consideration of initial elastic properties of the target material in the Modified R-PLH Model, the initial shock stress at time t=0 is reduced. The shock stresses for both models decrease with time and eventually reach a yielding level of 2.36 MPa.

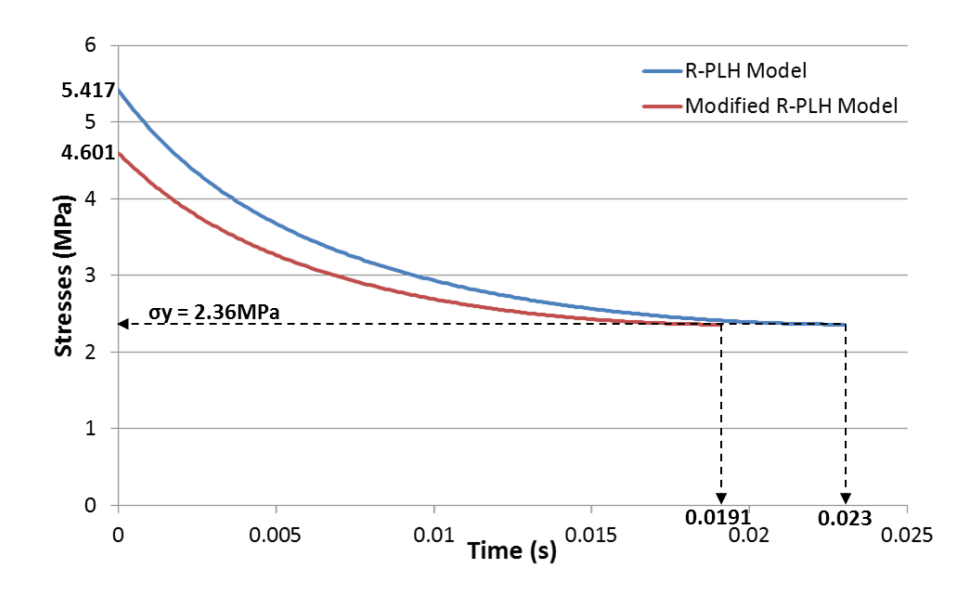


Figure 5-21: Analytical predictions of shock stresses for an impact velocity of 145 m/s

The left plot of Figure 5-22 extracts the effective stress-time histories for Element 2, 10 and 20 in the model with element size of 0.050 m to closely examine on the stress development across time domain. The "first" peak stresses for every element can be visibly identified, which will be used to compare with the shock stresses obtained from the analytical models. These initial peak stresses, which decrease with time, are induced when the plastic shock wave front propagates through the elements. For Element 10 and 20, it can be evidently seen that a precursor elastic wave first resulted an increase of effective stresses up to yielding stress value, before succeeding plastic shock wave kicks in to induce the "first" peak stresses. This is not as obvious for Element 2 since the separation distance between the plastic and elastic waves are generally small during the early phase of impact duration. Furthermore, it is evidently shown that the assumption of constant material stresses across the spatial domain within the crushed region (i.e. between the impactor and shock wave front) will be inaccurate. In fact, it can be seen at later part of impact duration, the material stresses within the plastic

zone are decreasing from the shock wave front to the impactor's end. This also implies that the numerical model predicts lower resultant shock stresses within the plastic zone, as compared to the analytical model. Note that the analytical model assumes constant shock stresses across spatial domain within the crushed zone. This observation of lower resultant shock stresses in the numerical model agrees well with the velocity-time curves of the impactor. The right plot of Figure 5-22 shows that velocity difference (i.e. velocity of impactor in numerical model minus velocity of impactor in analytical model) is increasing over time. The lowering of shock stresses in numerical model results in slower deceleration of the impactor.

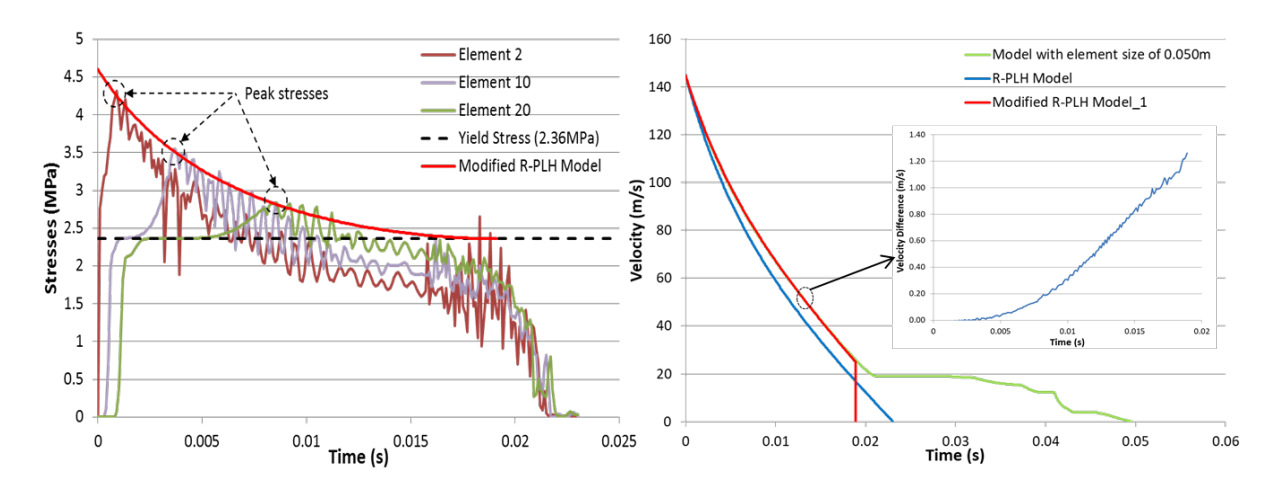


Figure 5-22: (Left plot) Effective stress-time histories for selected elements in 20mTL model with element size of 0.050 m, (Right plot) Velocity-time curve of impactors in numerical and analytical models, with velocity difference

Figure 5-23, Figure 5-24 and Figure 5-25 compares the "first" peak stresses of elements in models using different element sizes, with the analytical predictions. In general, the predictions from Modified R-PLH Model fit relatively well with the various numerical models. The first contact of impactor with target's Element 1 resulted in sharp surge of effective stress, which was higher than the analytically-predicted shock stress at time equals to zero. As time increases, the initial peak stresses of the elements generally reduce towards the yielding stress value of 2.36 MPa. This is expected since the precursor elastic wave will have already induced yielding stress to the uncrushed material ahead of the plastic shock wave. Note that when these peak stresses reach the yielding stress value, it also signifies the cessation of the plastic shock wave propagation.

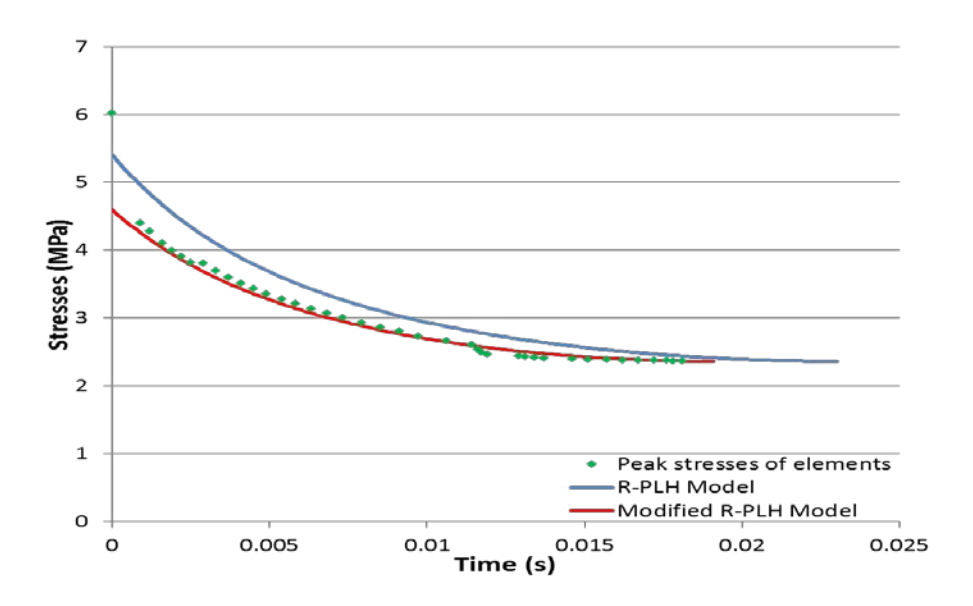


Figure 5-23: Comparison of "first" peak stresses in model (with element size of 0.050 m) with shock stresses predicted by analytical models

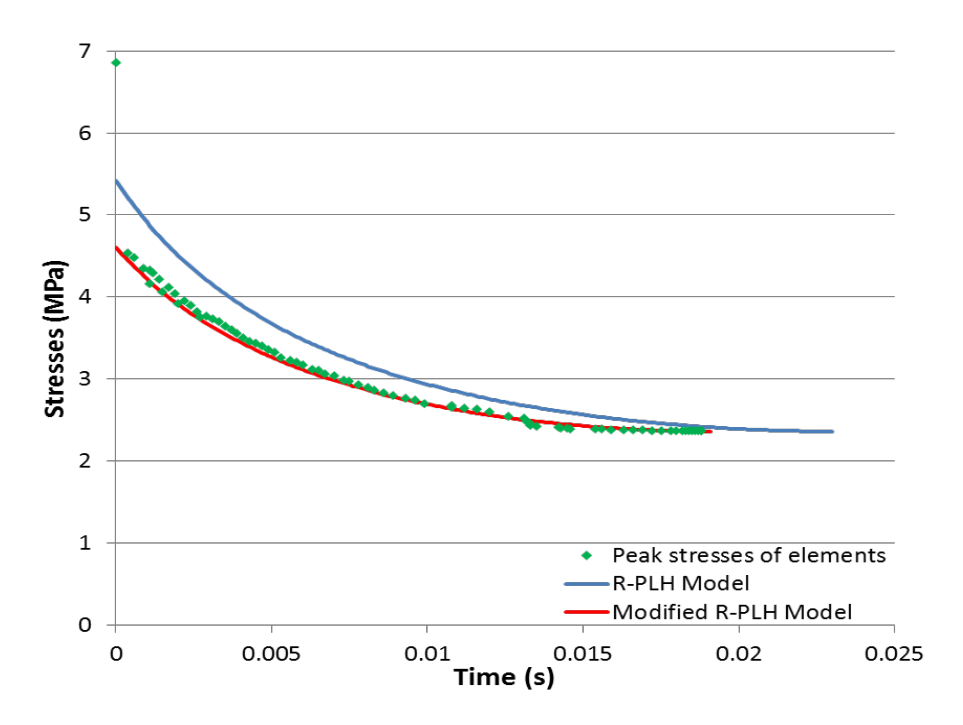


Figure 5-24: Comparison of "first" peak stresses in model (with element size of 0.025 m) with shock stresses predicted by analytical models

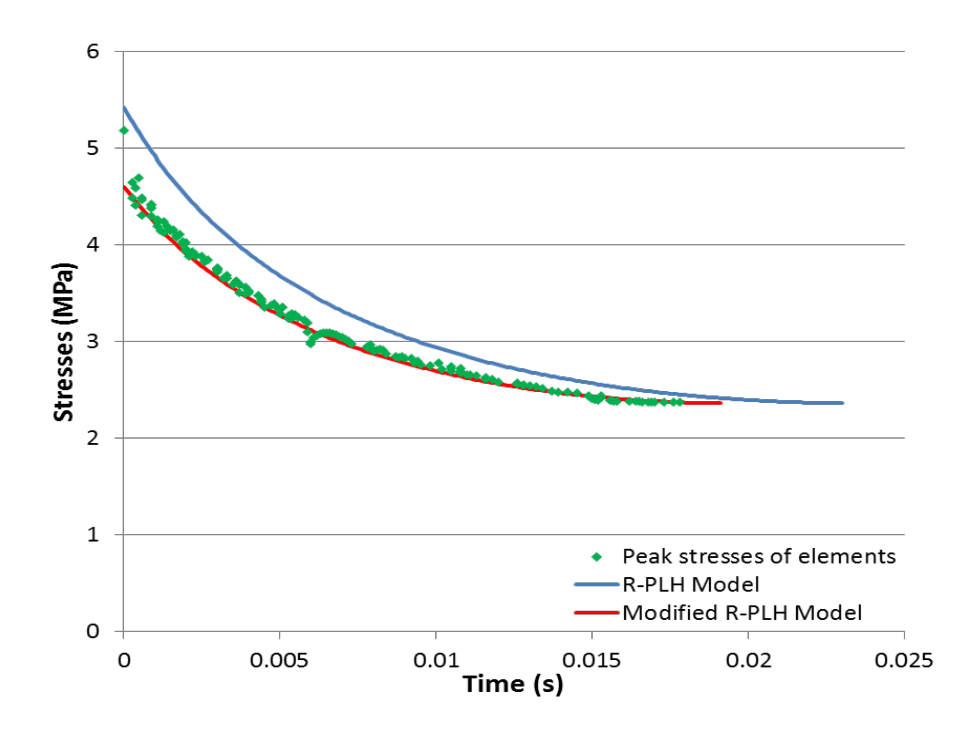


Figure 5-25: Comparison of "first" peak stresses in model (with element size of 0.010 m) with shock stresses predicted by analytical models

It is worth highlighting that the good agreement in the shock stress predictions further substantiates the consistency observed in the velocity-time history plots of impactor between the Modified R-PLH Model and the numerical simulations. This is pursuant to the fact that the shock stress (closely behind the shock wave front) obtained in the analytical model is the component that resists the motion of the impactor and the crushed material behind the plastic wave front. In the analytical model, both the impactor and the crushed material are assumed to travel at same velocity. Indeed, Figure 5-26 validates this assumption of particle velocity behind the wave front. Velocity-time curves of selected elements located at 0.1 m, 0.5 m, 1.0 m and 2.0 m respectively from the impact end are plotted against the impactor's velocity-time curve. It can be seen that an initial velocity of approximately 26.57 m/s is induced on the elements due to the presence of precursor elastic wave. Subsequently, the arrival of the plastic shock wave further increases the particle velocities to match with the impactor's velocity. This phenomenon demonstrates that the crushed materials are moving at the same velocity as the impactor. Note that the difference in the elastic velocity of 26.57 m/s, comparing to 24.77 m/s computed from the analytical model could be attributed by the steeper slope of stressstrain curves in the numerical model with higher loading rates. One can refer to the material model validation (See Section 5.1.1.1) for more information.

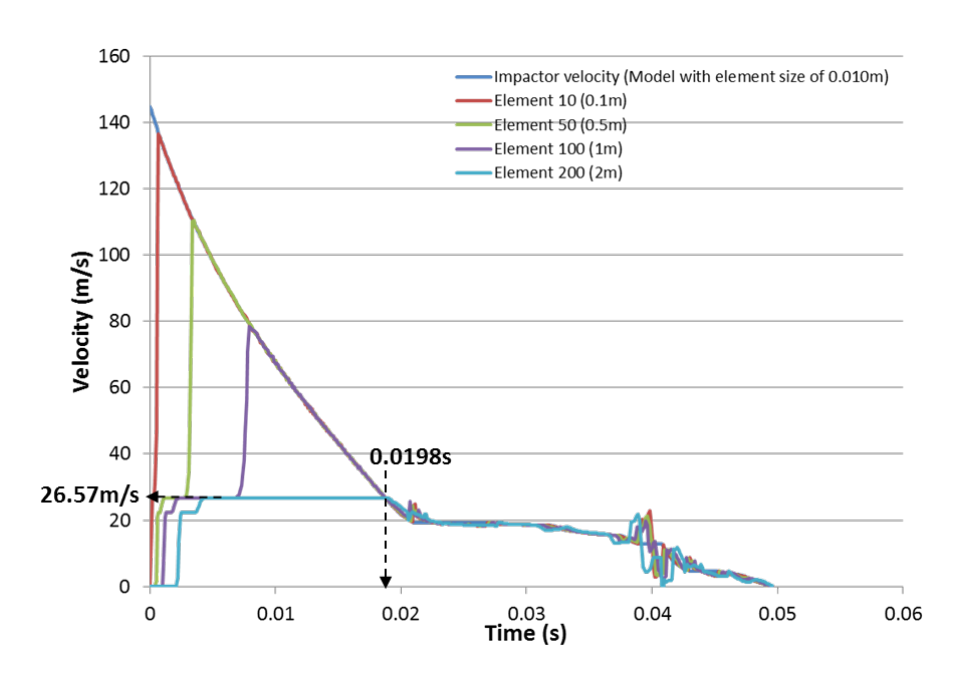


Figure 5-26: Velocities of selected elements in comparison with impactor's velocity for numerical model with element size of 0.010 m

5.3.3 Volumetric Strain-Time History of Target

Figure 5-27 presents the analytical predictions of shock strain for crushed material directly behind the shock wave front across the time domain. The Modified R-PLH Model predicts a lower initial shock strain response as compared to the R-PLH Model. Both models predict a gradual decrease in shock strain before coming to an abrupt decline of strain when approaching near its termination time, T_{end} . The lowest shock strain is determined when time $t=T_{end}$.

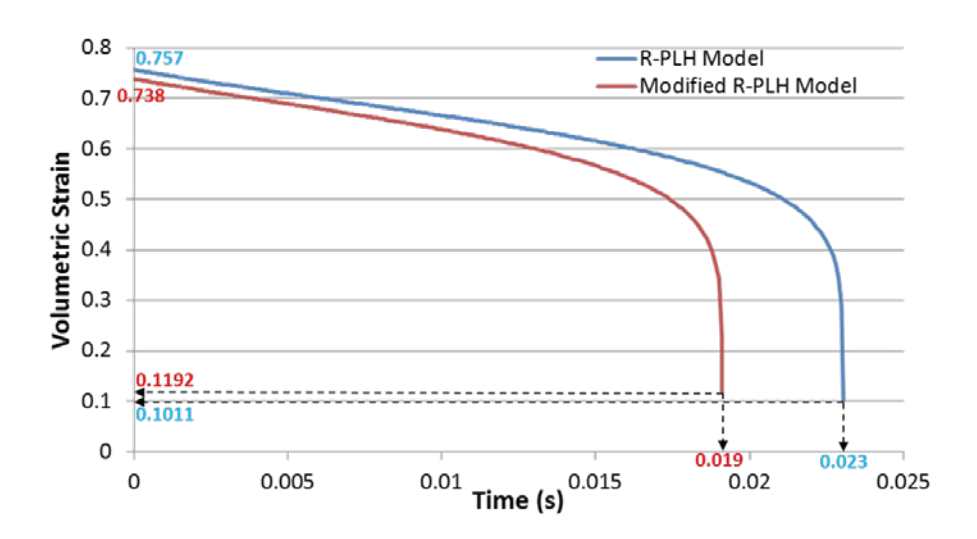


Figure 5-27: Analytical predictions of shock strain-time history for material in plastic region

To better understand the strain development of target elements across time domain, Figure 5-28 presents the volumetric strain-time histories of selected elements for model with element size of 0.050 m. These volumetric strains are evaluated based on the effective plastic strain

output obtained from numerical model. One can refer to the material model validation on how these volumetric strains can be computed. Due to presence of the precursor elastic wave, elements are first induced to elastic strain, before the shock wave front further increases the strain to initial shock level. This phenomenon is fairly obvious in elements located further away from the impact end. It is depicted that these initial shock strains for successive elements generally reduce over time, till it reaches the yield strain level.

The pre-defined elastic strain value for the target material is 0.0286. However, the elastic strain limit obtained from the numerical analysis is approximately 0.0343. This difference in elastic strain is observed and discussed in earlier section on material model validation.

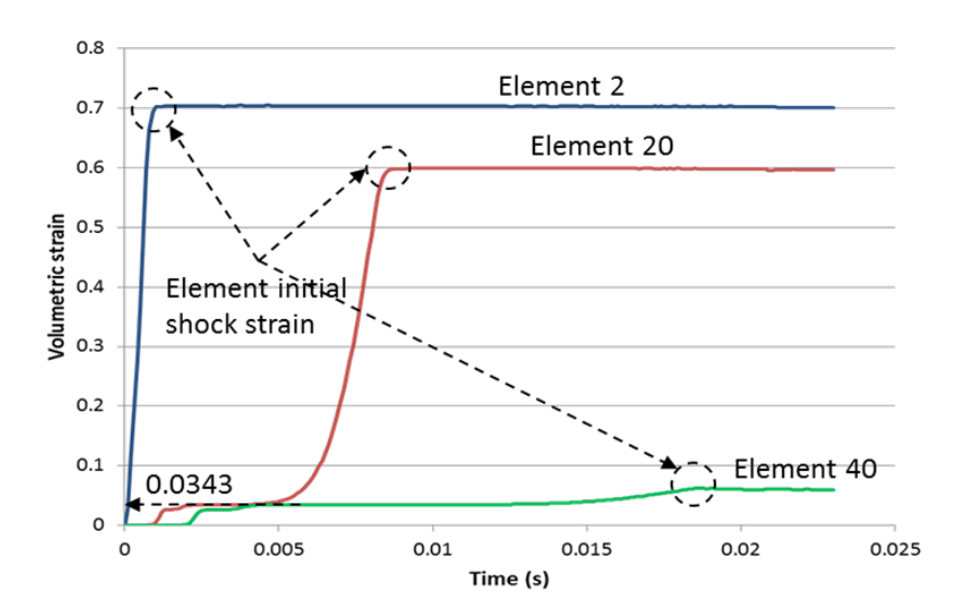


Figure 5-28: Volumetric strain-time histories for Element 2, 20 and 40 in model with element size of 0.050 m

Figure 5-29 combines the volumetric strain from the numerical model using element size of 0.050 m with the analytically-predicted shock strain. Both analytical models predicted higher initial shock strains, as compared to the numerical model, though the Modified R-PLH Model improves the predictions slightly. The predictions of higher shock strain from the analytical model appear to relate well with the phenomena observed from material model (MAT_63) validation exercise (See Section 5.1.1.1). Based on Figure 5-10, for a given stress value, the dynamic constitutive curve under a higher loading rate gives a lower corresponding volumetric strain, as compared to the material's quasi-static constitutive curve. At this juncture, it is good to highlight that the analytical model predictions are formulated using the material's quasi-static constitutive relationship. The profile of initial shock strain reduction over time from the Modified R-PLH Model appears to agree relatively well with the numerical results (i.e. gradual decrease of shock strain at initial impact duration, followed by a sharp decrease of shock strain at the later part of the impact duration).

The reduction of shock strain directly behind the shock wave shall eventually reach the elastic yield strain, as depicted from the numerical results in Figure 5-29. This is especially so when the precursor elastic wave will have yielded the material ahead of the shock wave front to elastic strain. However, due to truncation error in computation, the lowest strain values obtained from the analytical models are higher than the elastic strain value.

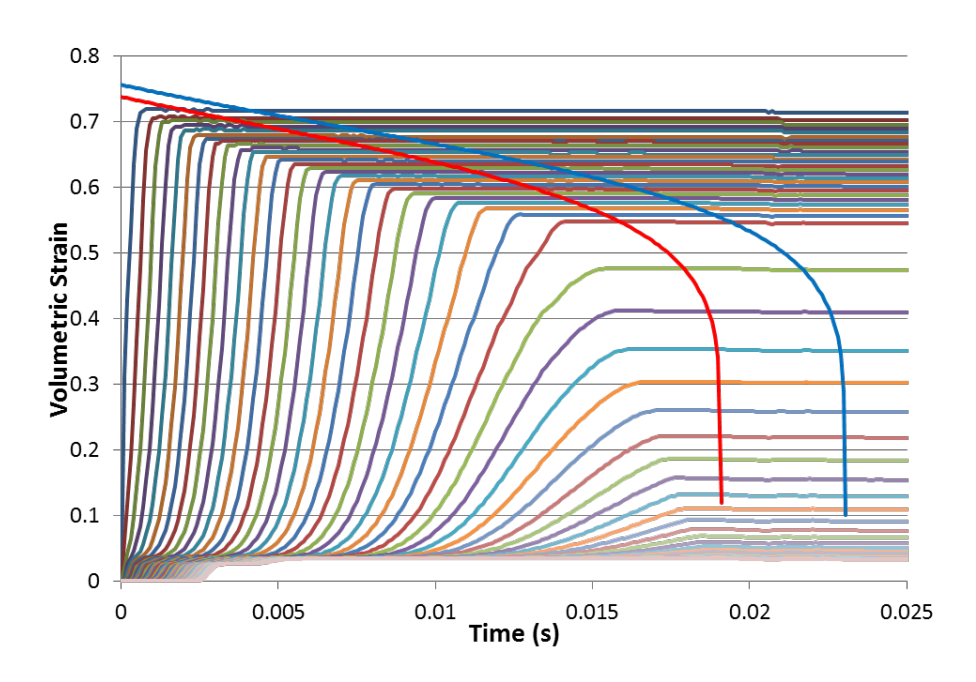


Figure 5-29: Volumetric strains in numerical model with element size of 0.050 m, in comparison with analytical model predictions

With the refinement of element size from 0.050 m to 0.010 m, the numerical model produces volumetric strain closer to the shock strain predicted by the analytical model. This is illustrated in Figure 5-30, where the difference of initial shock strain for Element 1 between the analytical model prediction and the numerical results reduces.

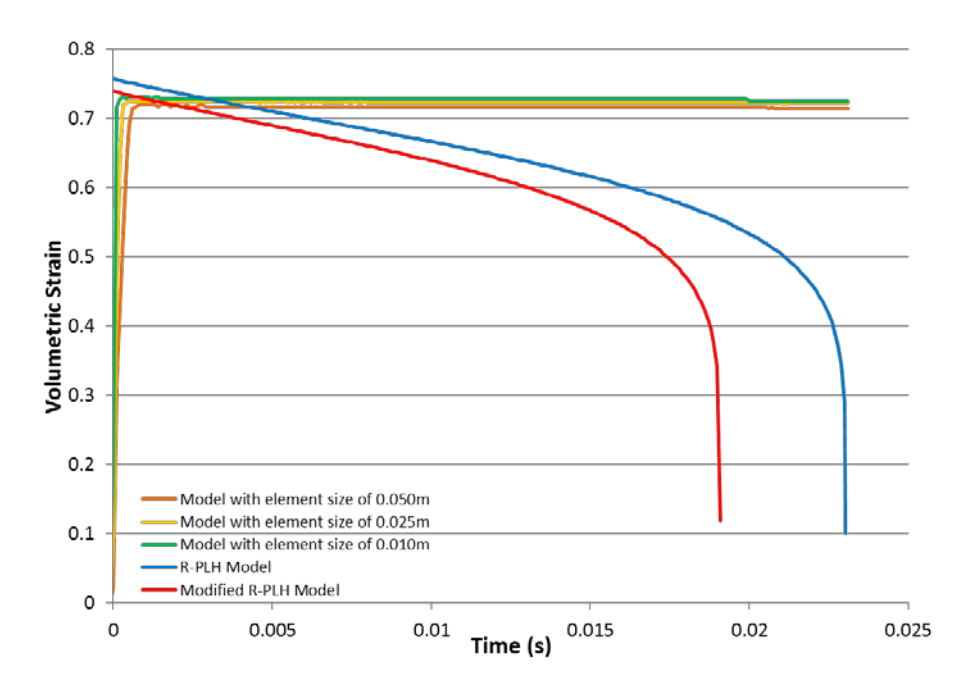


Figure 5-30: Volumetric strains for Element 1 in numerical models with different element sizes, in comparison with analytical model predictions

5.3.4 Plastic Shock Wave Propagation

The occurrence of plastic shock wave propagation in the numerical model can be visibly identified from the velocity-time curve of target elements, stress and strain development of the elements across the time domain. Due to the presence of shock wave, material particles behind the shock wave front are subjected to a sudden increase in velocity higher than the elastic velocity, as previously shown in Figure 5-26. This is the process whereby the target material is being crushed by the impactor. The jump of particle velocity in crushed region generally reduces as it approaches elastic velocity, which also implies the cessation of the shock wave. Similarly, elements are also subjected to abrupt jump in stress and strain; as the shock wave propagates pass these elements. That is why the onsets of "first" peak stress and the initial shock strain of elements in numerical models have been associated with the presence of plastic shock wave propagation. As the plastic shock wave ceases, the shock stress and strain reduce to yielding stress and elastic strain.

Figure 5-31, Figure 5-32 and Figure 5-33 present the effective stresses and volumetric strain of selected elements in model with element size of 0.010 m over time domain, in comparison with Modified R-PLH Model prediction of shock stress. The positioning of the shock wave front established based on peak effective stress appears to associate well with the onset of the initial shock strain. However, as the strength of plastic shock wave diminishes over time, this phenomenon become less obvious.

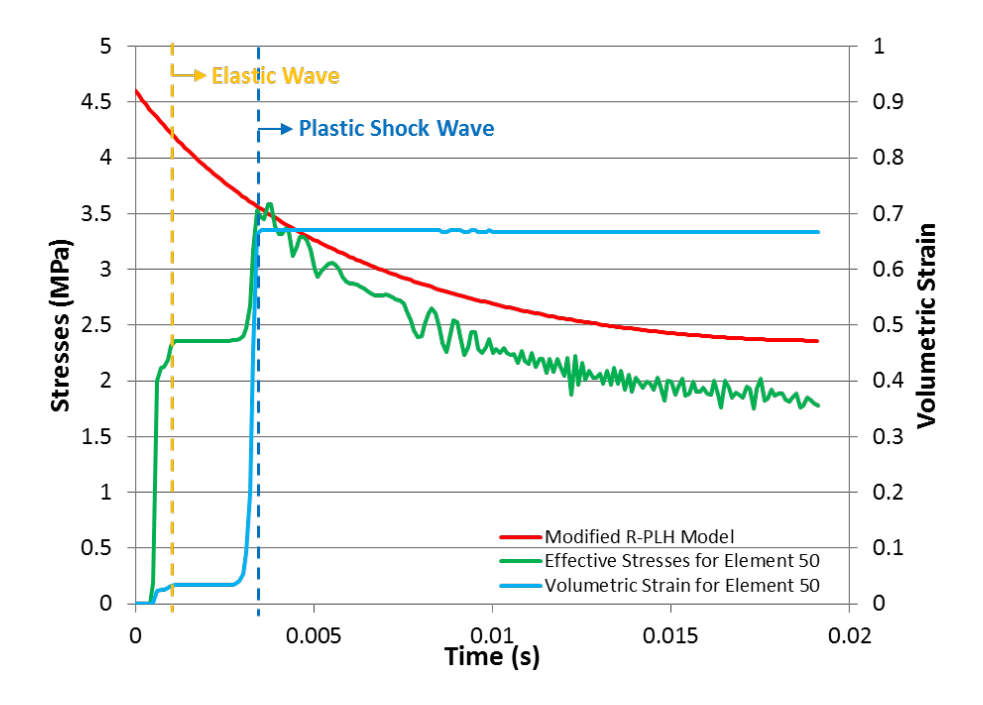


Figure 5-31: Effective stress and volumetric strain-time histories for Element 50

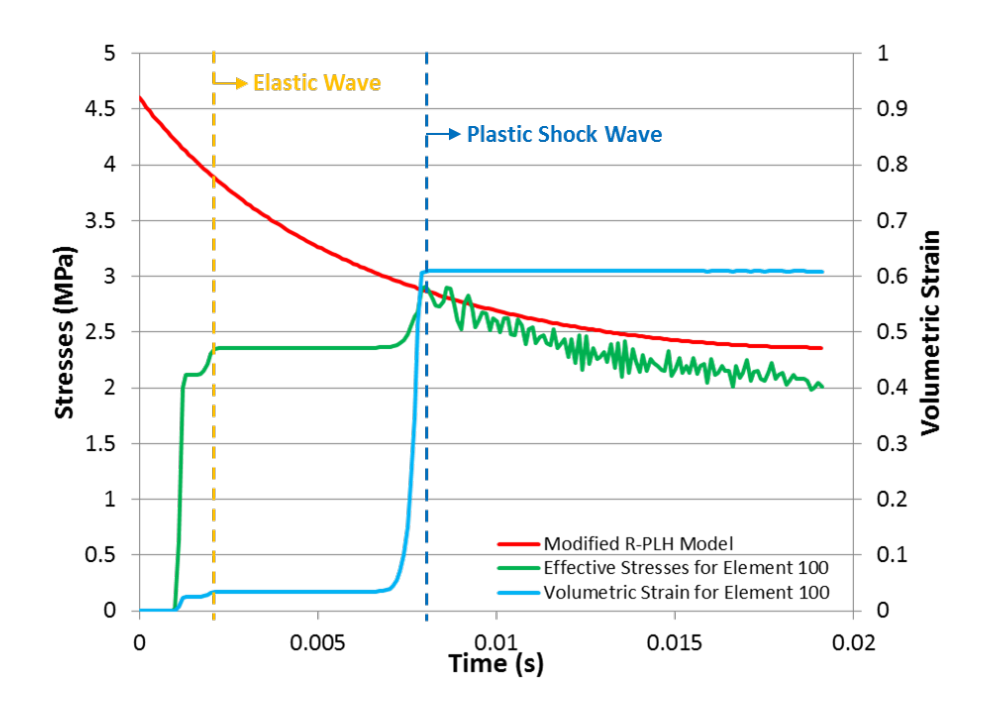


Figure 5-32: Effective stress and volumetric strain-time histories for Element 100

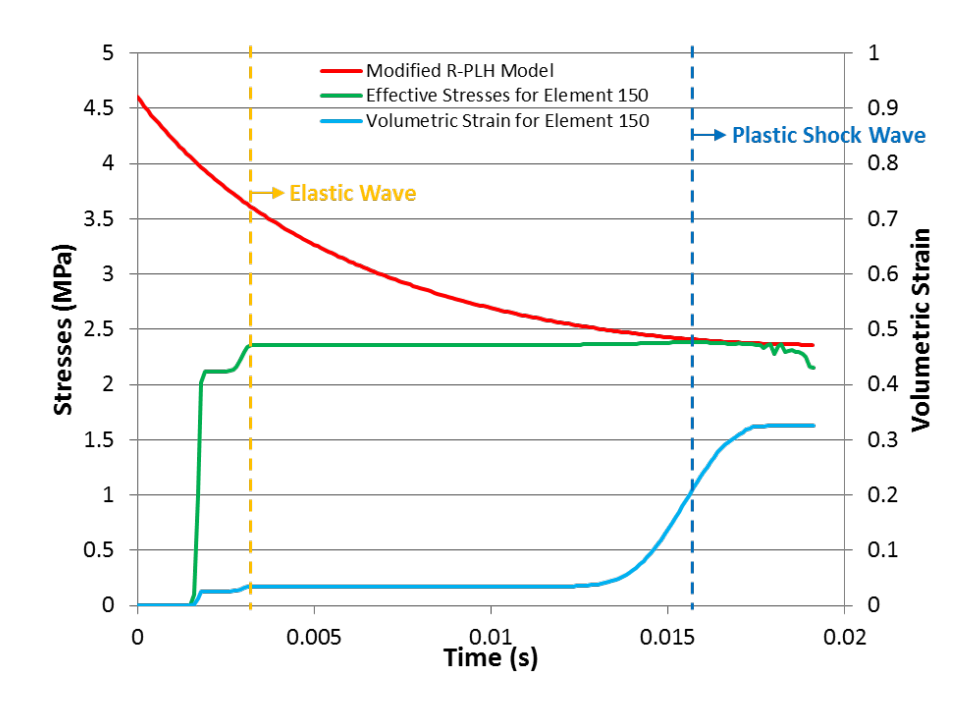


Figure 5-33: Effective stress and volumetric strain-time histories for Element 150

Based on Modified R-PLH Model, the termination distance for plastic shock wave is evaluated at 1.951 m from the target front, at a termination time of t=0.019 s. The shock wave termination also implies that the relative velocities of shock wave front and impactor, with respect to the particle velocity (i.e. $v_{A_{initial}} = 24.77$ m/s) due to elastic wave, to reach zero. Figure 5-34 shows the relative velocities of the shock wave front and the debris (i.e. impactor).

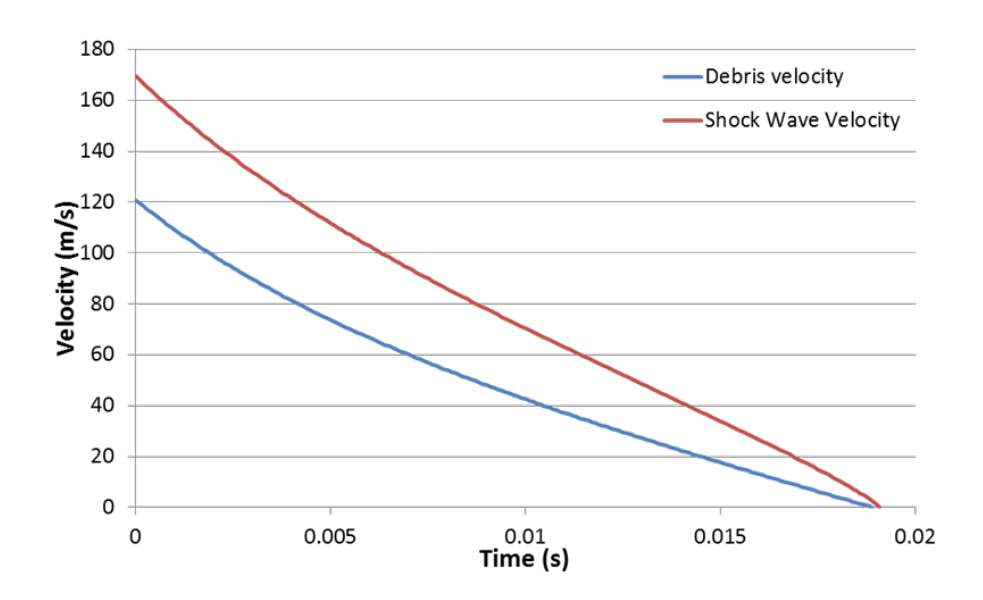


Figure 5-34: Relative velocities of shock wave front and debris from Modified R-PLH Model

Table 5-3 compares the arrival times for the plastic shock wave predicted by the Modified R-PLH Model and the numerical results based on model with element size of 0.010 m. Three specific locations within the crushed region defined by the analytical model are considered. It appears that the shock wave in the numerical model arrives slower than the one predicted in analytical model, which also explain why the shock stresses from the analytical model is higher than the numerical predictions at the same location.

Modified R-PLH Model Predictions				Numerio	al Predictions	
Location (m)	Shock stress (MPa)	Time of arrival (ms)	Element ID	Location (m)	Peak stress (MPa)	Time of arrival (ms)
0.5	3.693	2.85	50	0.495	3.584	3.71
1.0	3.047	6.50	100	0.995	2.906	8.01
1.5	2.604	11.25	150	1.495	2.381	15.61

Table 5-3: Comparison of arrival times of plastic shock wave in numerical and analytical models

Now, consider that the termination distance of shock wave predicted by the Modified R-PLH Model is 1.952 m from the impact end. The integration point of Element 195 is positioned at 1.945m. Figure 5-35 shows the effective stress and strain-time histories of this element. Both the stress and strain time histories depict that this element is not affected by the plastic wave propagation, which also suggests that the shock wave will probably be terminated before reaching this element.

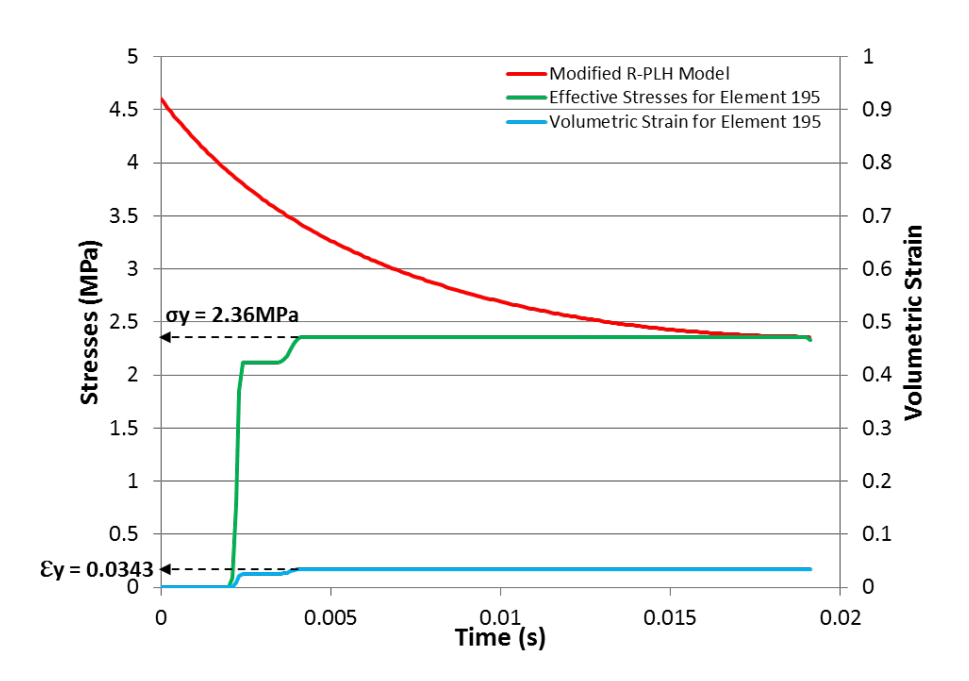


Figure 5-35: Effective stress and volumetric strain for Element 195 in model with element size of 0.010m

As previously illustrated in Figure 5-26, the velocity-time curves of target elements and impactor indicate that the plastic shock wave will likely to terminate before time t=0.0198 s. Considering the time ranging from t=0 to t=0.0198 s, the maximum plastic strain induced over the spatial domain of the target elements is presented in Figure 5-36. It is evidently shown that with the refinement of element sizes, the distance in which the shock wave terminates (i.e. when plastic strain reaches zero) generally decreases. The model with element size of 0.010 m shows that its shock wave terminates before the distance of 1.952 m, which is evaluated by the analytical model.

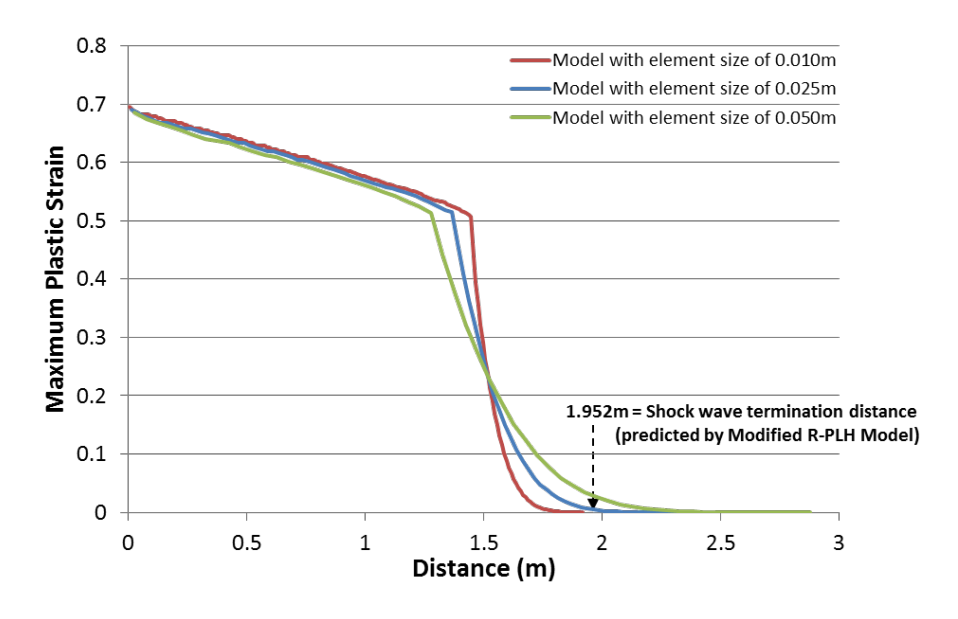


Figure 5-36: Maximum plastic strain of elements in numerical models with different element sizes, under impact velocity of 145 m/s

5.3.5 Effects of Different Impact Velocities

It is also of interest to study the responses of target material with respect to lower impact velocities of 50 m/s and 100 m/s. This section considers numerical models with different element sizes. Figure 5-27, Figure 5-28 and Figure 5-29 display the "first" peak stresses of elements with the analytical model predictions under impact velocities of 100 m/s and 50 m/s. It can be concluded that the shock stress predictions based on Modified R-PLH Model are in good agreement with the numerical results. Though for the case of higher impact velocities (i.e. 100 m/s), the peak stresses of numerical models with smaller element sizes appear to be more consistent than the models with coarser element sizes.

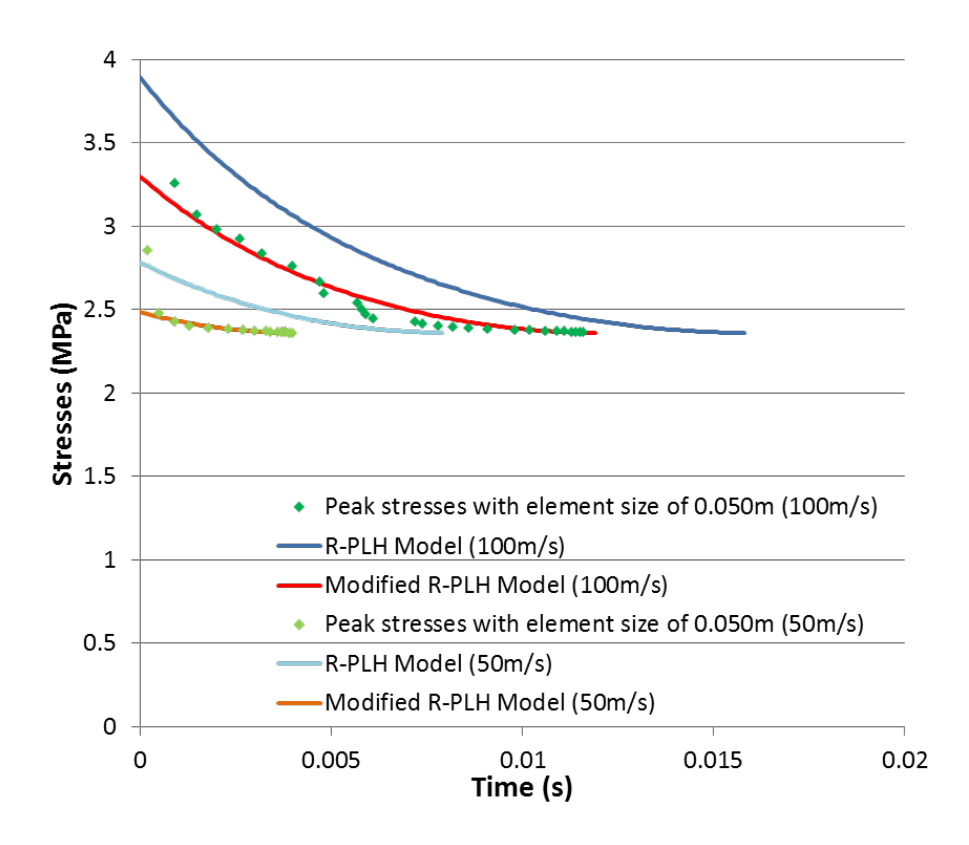


Figure 5-37: Peak stresses of elements (size of 0.050 m) with analytical predictions for different impact velocities

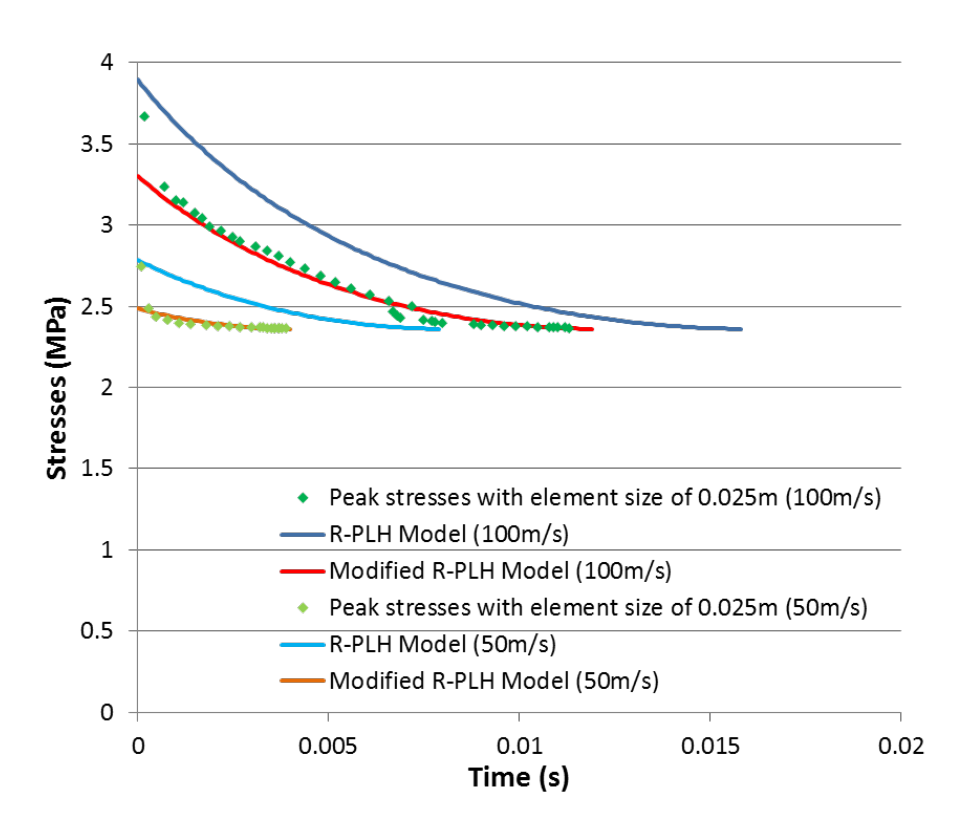


Figure 5-38: Peak stresses of elements (size of 0.025 m) with analytical predictions for different impact velocities

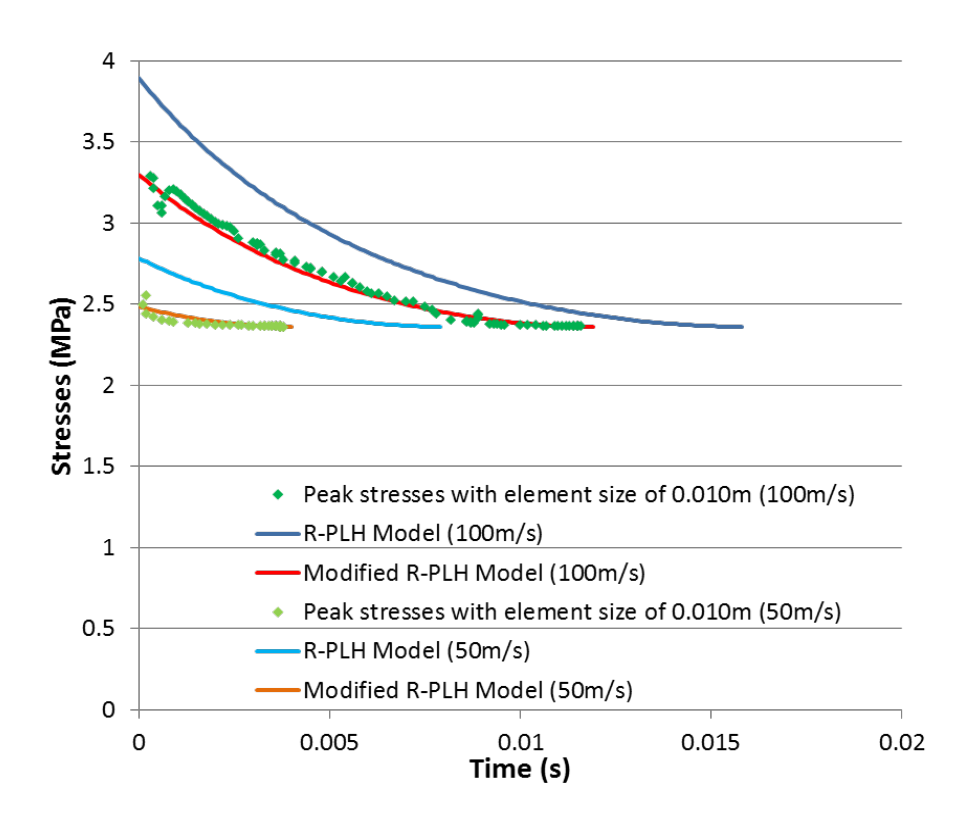


Figure 5-39: Peak stresses of elements (size of 0.010 m) with analytical predictions for different impact velocities

Table 5-4 presents the peak stresses of elements in numerical models with different element sizes at three different impact velocities, in comparison with the analytical model prediction of shock stresses. For comparison to be representative; the stresses from all numerical models are obtained at the same distance from the impactor's end. The integration point of Element 1 in model with mesh size 0.050 m is located at 0.025 m from the front. Apparently, it can be observed that the models with smallest element size of 0.010 m produces shock stresses that are closest to the one obtained from the analytical predictions, for impact velocities of 50 m/s and 145 m/s. For velocity of 100 m/s, it is the second closest.

	Analytical Prediction		Numerical Prediction		
Impact Velocities (m/s)	Initial Shock Stress (MPa)	Peak Stress of Element (MPa) (located at 0.025m from impactor's end)			
(III/3)	Modified R-PLH Model	Mesh Size = 0.010m	Mesh Size = 0.025m	Mesh Size = 0.050m	
50	2.484	2.440	2.615	2.854	
100	3.299	3.213	3.447	3.254	
145	4.601	4.639	5.694	6.022	

Table 5-4: Comparison of peak stresses with analytical model prediction of initial shock stresses

Figure 5-40 and Figure 5-41 compare the volumetric strain-time histories of Element 1 in numerical models with analytical predictions for the case of 50 m/s and 100 m/s respectively. In both figures, different element sizes are considered. Both figures show that with further mesh refinement, the initial shock strain in the numerical model generally correlate better with the analytical model predictions. Though it can be seen that the analytical models still predict higher initial shock strains, with Modified R-PLH Model provides slightly improved results. The numerical model with impact velocity of 50 m/s appears to be more sensitive to element size refinement.

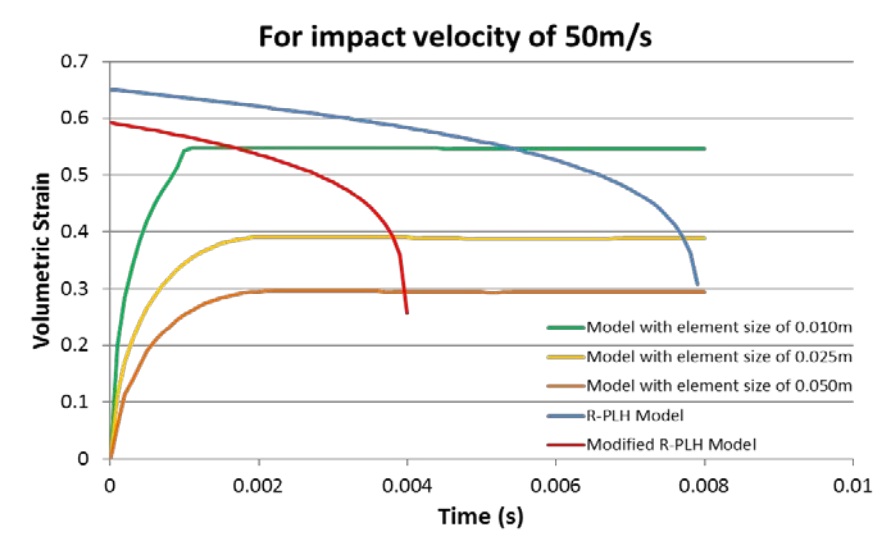


Figure 5-40: Volumetric strain-time histories of Element 1 in models of different element sizes for impact velocity of 50 m/s

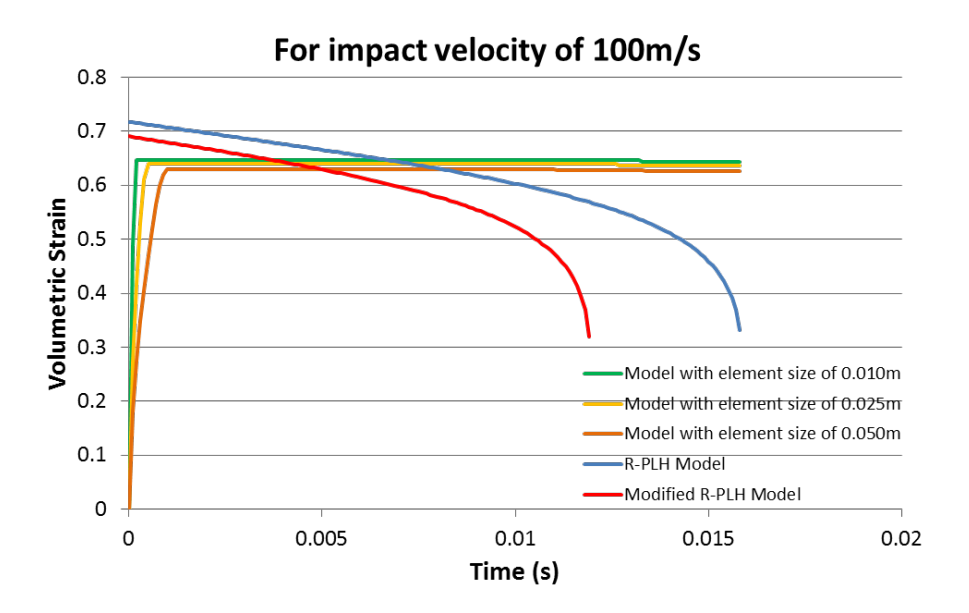


Figure 5-41: Volumetric strain-time histories of Element 1 in models of different element sizes for impact velocity of 100 m/s

Figure 5-42 and Figure 5-43 show the velocity-time curve for the numerical models with different element sizes, under impact velocity of 50 m/s and 100 m/s respectively. The Modified R-PLH model predicts results closer to the numerical models in particular when higher impact velocity is involved. But for the case of 50 m/s, the differences between R-PLH Model and Modified R-PLH Model in predicting impactor's velocity rate are rather negligible. The effect of element size reduction in model with higher impact velocities (i.e. 100 m/s and 145 m/s) do not seem to be dominating in the velocity-time curve of impactor. Conversely, for model with impact velocity of 50 m/s, the reduction in element size further increases the overall distance travelled by the impactor (i.e. area under the velocity-time curve).

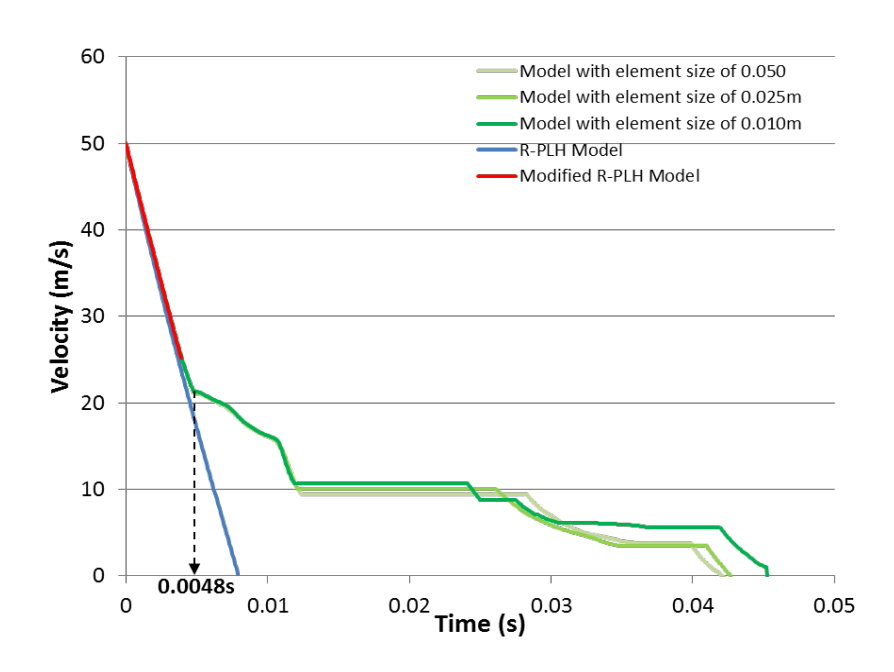


Figure 5-42: Velocity-time curve for model with initial impact velocity of 50 m/s

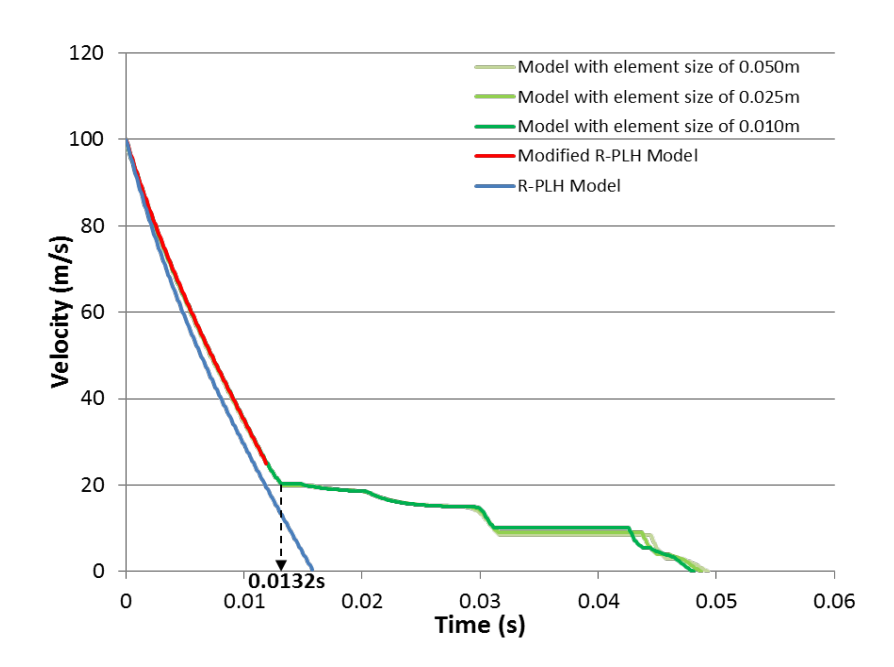


Figure 5-43: Velocity-time curve for model with initial impact velocity of 100 m/s

To evaluate the shock wave propagation in the numerical models against the analytical predictions, Figure 5-44 and Figure 5-45 present the maximum plastic strain induced over the spatial domain of the target elements, with indication of the termination distance predicted by the Modified R-PLH Model. It can be seen that in both cases of impact velocities, the distances in which the shock wave terminates in the numerical models, regardless of the element sizes, are observed to be greater than the analytical predictions. Nevertheless, with the refinement of mesh sizes, this termination distance appear to be closer to the analytical predictions.

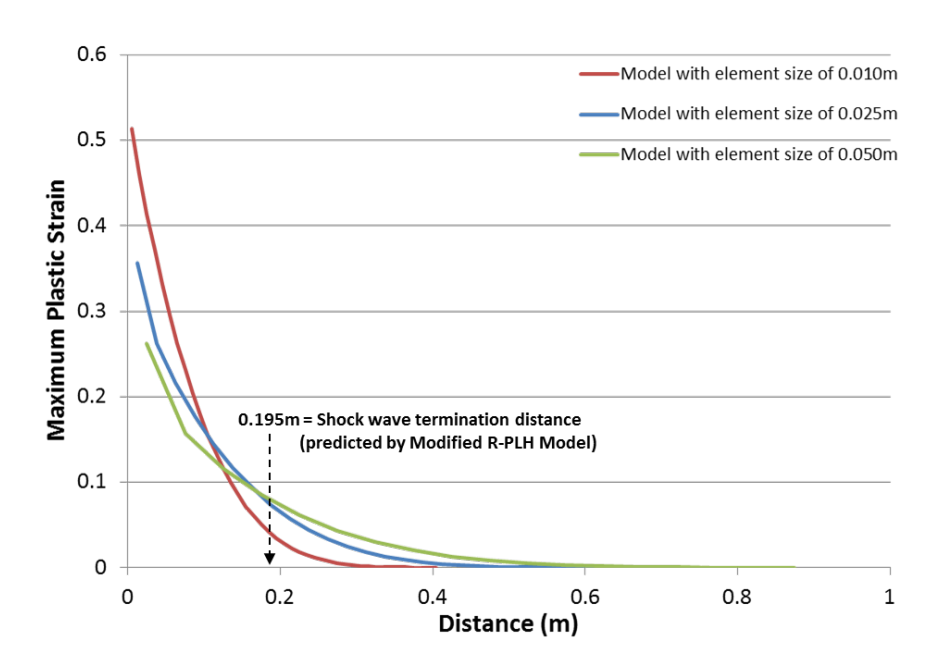


Figure 5-44: Maximum plastic strain of elements in numerical models with different element sizes, under impact velocity of 50 m/s

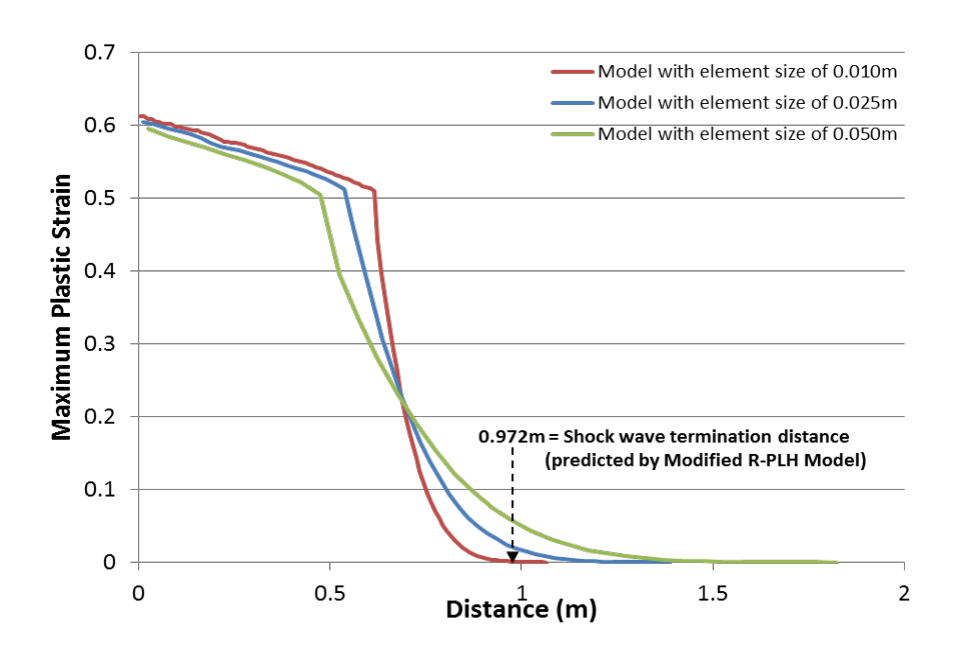


Figure 5-45: Maximum plastic strain of elements in numerical models with different element sizes, under impact velocity of 100 m/s

Table 5-5 compiles the shock wave termination distances from various numerical models under different impact velocities, in comparison with the Modified R-PLH Model predictions. Note that this termination distances are evaluated based on the plastic strain development within the target elements.

	Shock Wave Termination Distance (m)						
Impact Velocities (m/s)	Analytical Predictions (Modified R-PLH Model)	Numerical Models					
	(17001100 11 1 211 112001)	0.010m	0.025m	0.050m			
50	0.195	0.400	0.625	0.850			
100	0.972	1.060	1.375	1.800			
145	1.952	1.920	2.300	2.850			

Table 5-5: Shock wave termination distances predicted by numerical and analytical models

In addition, it is established that the termination times of the shock wave in the numerical model with element size of 0.010 m for the three different impact velocities are respectively; 0.0038 s for 50 m/s, 0.0117 s for 100 m/s and 0.01901 s for 145 m/s. These timings are before the times that are depicted in the impactor's velocity-time curves in Figure 5-26, Figure 5-42 and Figure 5-43. It is therefore reasonable to conclude that the crushing of target material due to incident plastic shock wave propagation has ceased before reaching elastic velocity.

5.3.6 Concluding Remarks

Numerical model with 20 m target length and initial impact velocity of 145 m/s

The inclusion of initial elastic properties of the foam material into the analytical model (i.e. particularly, Modified R-PLH Model_1) does improve the prediction of impactor's velocity-time relation. This observation is further validated through the consistency observed between the initial peak effective stresses of target elements and the shock stresses determined from the analytical model. The assumption of constant particle elastic velocity $v_{A_{initial}}$ throughout the impact duration seems to agree well with the numerical results, even though it remains questionable on how this elastic velocity decelerates to zero.

The consistency of "first" peak stresses of elements in time domain, with the Modified R-PLH Model has further reinforced the good agreement in velocity-time curve of impactors between the analytical and the numerical model. This proposition is valid since in the derivation of the analytical model, it is established that the component which resists the motions of impactor and crushed material is the shock stresses directly behind the plastic wave front. Therefore, this shock stress will be an important parameter to evaluate in order to obtain an accurate prediction of impactor's velocity. Furthermore, the use of finer element size (i.e. 0.010 m) provides an initial shock stress for Element 1 that is closer to the analytical model prediction.

Both analytical models predicted higher shock strains, as compared to the numerical results. It is also observed that as the element sizes reduces from 0.050 m to 0.010 m, the difference of initial shock strain for Element 1 between the analytical model prediction and the numerical results decreases.

The Modified R-PLH Model predicts the shock wave to terminate at 1.952 m from the impact end. This prediction seems to agree well with the numerical model that consists of element size of 0.010 m. The numerical models with coarser element sizes (i.e. 0.025 m and 0.050 m) produce shock waves that terminate beyond 2 m from the impact end.

Numerical models with 20 m target length but with lower impact velocities

Regardless of the impact velocities, the Modified R-PLH Model prediction of shock stresses largely relates very well with the numerical results. This is also the attributing factor to the consistency between the numerical model and the prediction by Modified R-PLH Model in velocity-time curve of the impactor. The use of finer element size (i.e. $0.010 \, \mathrm{m}$) produces the initial peak stresses of Element 1 that are closest to the shock stresses predicted by the Modified R-PLH Model. Conversely, the agreement of initial shock strain prediction between the analytical and numerical model are less satisfactory, particularly when the impact velocity decreases. Nevertheless, the decrease of element sizes in the numerical models appears to mitigate these differences with analytical model predictions.

Using the plastic strain development of target elements, the termination distance of plastic wave front is evaluated. It is established that with the use of element size of 0.010 m, the numerical model predictions will be in fairly good agreement with the analytical predictions, particularly when impact velocities are high (i.e. 100 m/s and 145 m/s). The modelling of

target element using size of 0.010 m seems to provide improved correlations with the analytical predictions.

To conclude, it is important to note that the 20mTL numerical model has well-validated the predictions from Modified R-PLH Model within the higher velocity time response regime (i.e. debris velocity ranging from initial impact velocity to near elastic velocity $v_{A_{initial}}$). This is especially so since the Modified R-PLH Model mainly predicts responses induced by plastic shock wave. In the lower velocity time response regime (i.e. debris velocity lower than elastic velocity), it is evaluated from the 20mTL model that only elastic waves are propagating. The debris deceleration will very much depend on the overall length of target. It is observed that as the overall target length increases, the distance travelled by debris within this lower velocity time response regime increases.

5.4 1D Numerical Model of 2 m Target Length - Design of Soft-Catcher

The previous sections have validated the 1D analytical model predictions using numerical models with 20 m target length, as well as studying the effect of element size refinement.

Now, considering that the overall thickness of soft-catcher to be limited to say, 2 m, it will be worthwhile to highlight and discuss the differences in target response for the numerical model with 2 m target length. The close proximity to target's end boundary condition can significantly increase the effective stresses and strains of the elements near the target's end, affecting the shock wave propagation. These effects may influence the overall impact resistance and the rate of velocity for the impactor. The element size to consider in this section will be 0.010 m. Recommendations will eventually be put forward in an attempt to relate numerical outputs with key design considerations for the soft-catcher.

5.4.1 Velocity-Time History of Impactor

The effects of end boundary condition for the target kick in at much earlier timing as compared to the model with 20 m target length (20mTL). Figure 5-46 illustrates the velocity-time curves for numerical models with 2 m and 20 m target length, for an initial impact velocity of 145 m/s. The smaller plot indicates the difference in velocities between the two models. The curve from the model with 2 m target length (2mTL) is observed to deviate from the other model at time of about t=0.012 s. This deviation in the rate of velocity before reaching elastic velocity may also suggest that the plastic wave termination is likely to be affected by the end boundary effects under this impact velocity of 145 m/s.

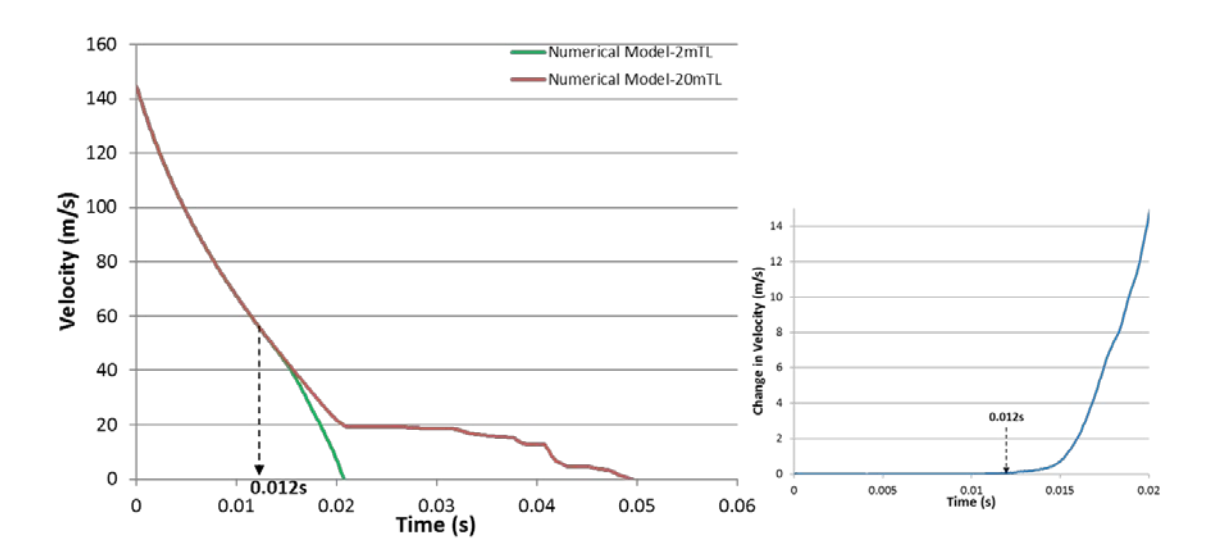


Figure 5-46: Velocity-time curves for models with 2 m and 20 m target length under impact velocity of 145 m/s; plot of difference in velocities (2mTL vs 20mTL) in time domain

5.4.2 Effective Stress-Time History of Target

Previously, it was emphasized that the shock stress directly behind the plastic wave front will be a key parameter to consider for obtaining an accurate prediction of impactor's velocity-time curve. Knowing that the rate of velocity for impactor in the model with 2mTL remain consistent with the other numerical model (i.e. 20mTL) before time t=0.012 s, it is therefore viable to substantiate the effective stress development of target elements in the 2mTL model before time t=0.012 s. Figure 5-47 depicts that the "first" peak stresses of Element 1 to 130 (Element 130's integration point being located at 1.295 m) are in good relatively agreement with the shock stress predictions in Modified R-PLH Model. The peak stress for Element 130 occurs at time t=0.01201 s. The initial impact velocity is 145 m/s.

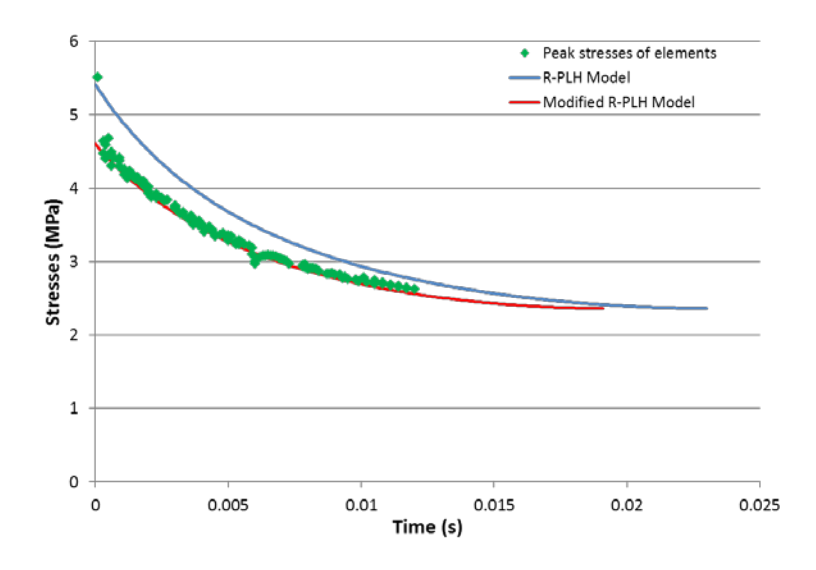


Figure 5-47: "First" peak stresses of Element 1 to 130 for numerical model with 2mTL, in comparison with analytical model predictions

Figure 5-48 compares the "first" peak stresses for Element 1 to 130 of these two numerical models. It also illustrates the respective stress-time histories plots for Element 50 and 175. Two key observations are noted: (i) the peak stresses appear to relate very well between these two numerical models; (ii) the end boundary effect for 2mTL model has resulted a gradual surge in effective stresses of target elements beyond time t=0.012 s. Prior to this, the responses of numerical models (both 2mTL and 20mTL) appear to have no significant differences in terms of peak and effective stresses.

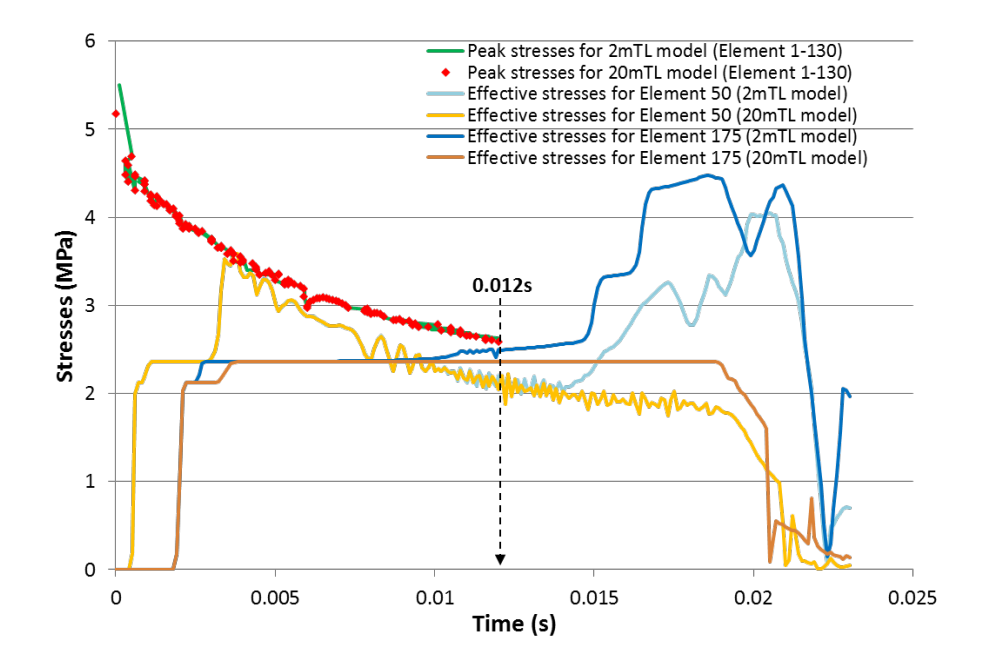


Figure 5-48: Comparison of "first" peak stresses (Element 1 - 130) and effective stresses (Element 50 and 175) between 2mTL and 20mTL model

5.4.3 Volumetric Strain-Time History of Target

Figure 5-49 demonstrates on how the close proximity to target end boundary condition can influence the volumetric strain development of elements in 2mTL model under an impact velocity of 145 m/s. The elements nearer to the impact end experience usual increase in strain due to plastic shock wave propagation, during the initial impact duration. Apparently, the Element 1 experiences almost similar increase in strain for both models, regardless of target length.

However, the response of Element 200 (i.e. at the target end) in both models differs. The surge in volumetric strain for Element 200 in 2mTL model occurs as early as time t=0.0024 s, which is predominately attributed by the effects of end boundary. It is noted that this timing agrees fairly well with the time at which the precursor elastic wave will probably reach the target end. (Given that the linear sound speed of elastic wave is about 866 m/s for E=82.5 MPa and initial density of 110 kg/m3. Thus, to reach a distance of 2 m, the time required is approximately 0.0023 s)

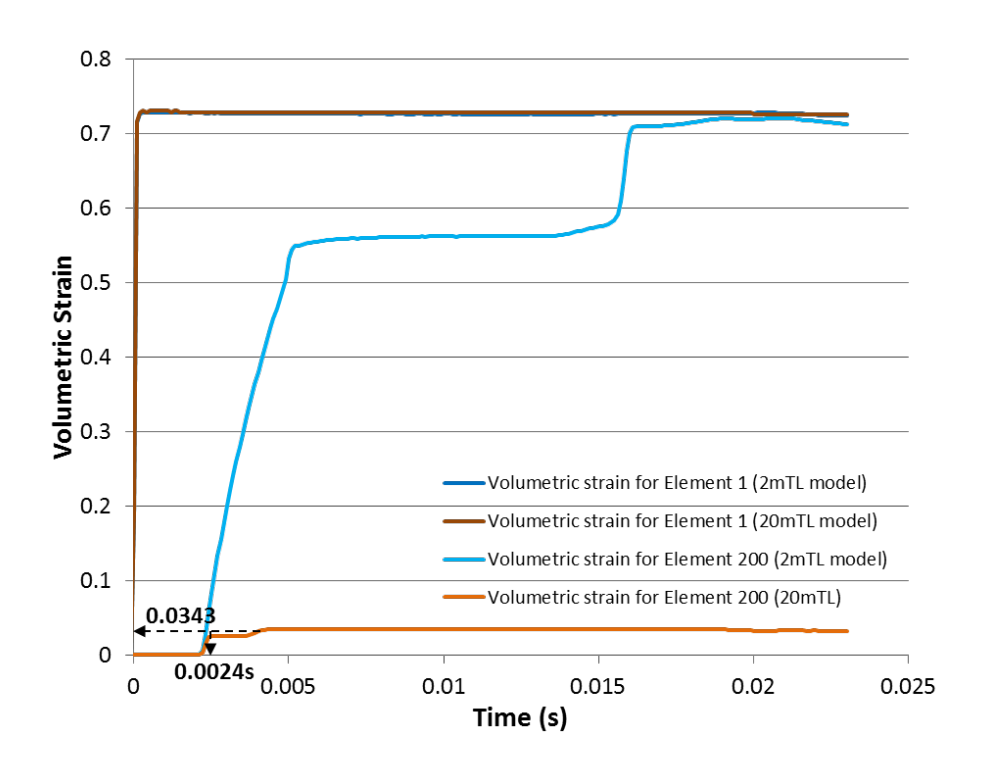


Figure 5-49: Volumetric strain-time histories of selected elements for 2mTL and 20mTL model

5.4.4 Plastic Shock Wave Propagation

Figure 5-50 illustrates the maximum plastic strain for the target elements in model with 2mTL, comparing the model with 20mTL under an impact velocity of 145 m/s. It is evidently shown that the termination of the plastic wave propagation is indeed affected by the end boundary effect. The location of which the shock wave terminates cannot be easily identified in this 2mTL model.

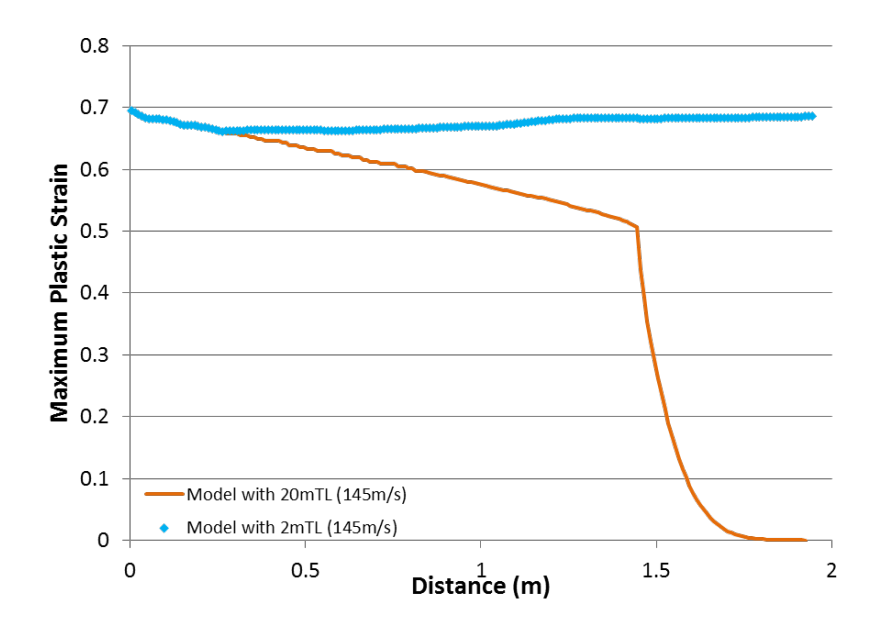


Figure 5-50: Maximum plastic strain for models with 2mTL and 20mTL, under impact velocity of 145 m/s

5.4.5 Impact Velocities of 50m/s and 100m/s

Figure 5-51 shows that the rate of velocity for impactors in models with 2 m target length under impact velocities of 50 m/s and 100 m/s do not differ from the respective models with 20m target length, within the regime above the elastic velocity. Hence, in both cases, the effects of end boundary may not be as significant as compared to the case of 145 m/s, to influence the plastic shock wave propagation. Figure 5-52 shows that the "first" peak stresses of elements are indeed in good agreement with the Modified R-PLH Model.

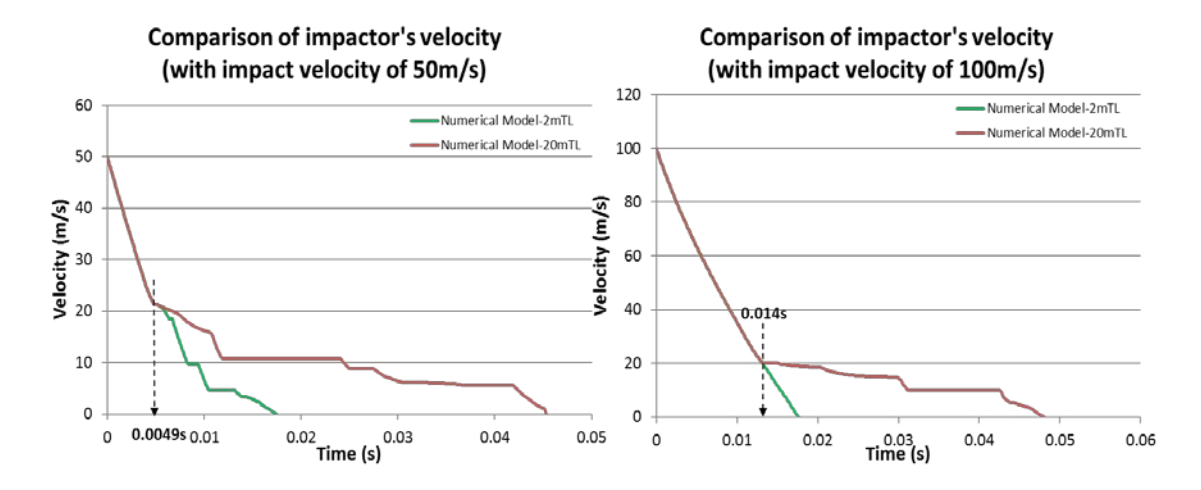


Figure 5-51: Velocity-time curves for models with 2mTL and 20mTL, under the initial impact velocities of 50 m/s and 100 m/s.

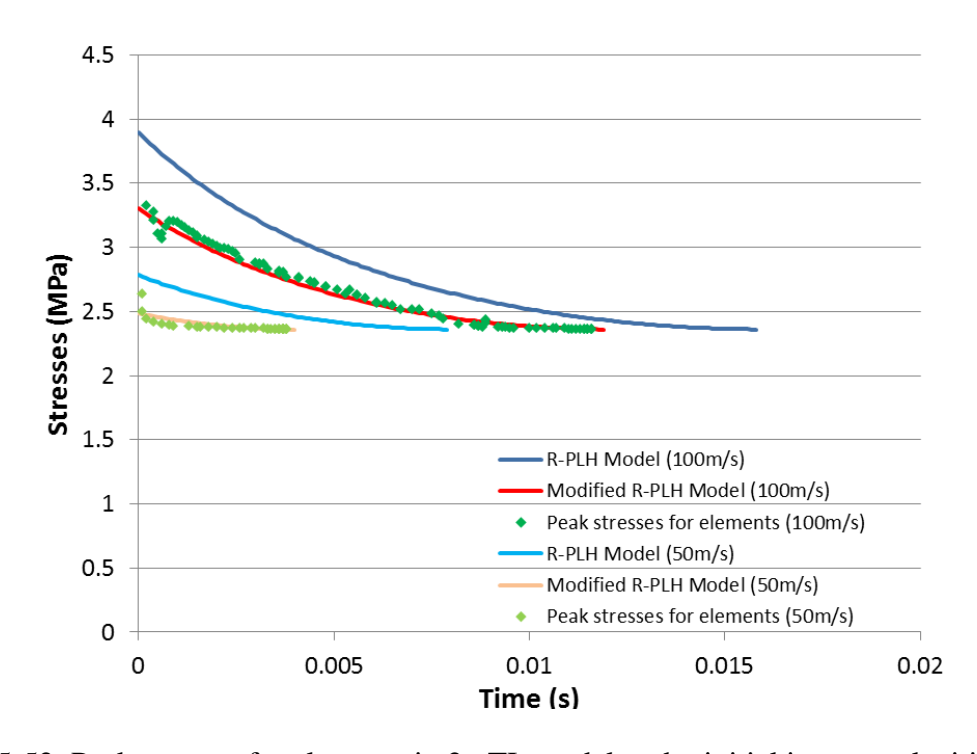


Figure 5-52: Peak stresses for elements in 2mTL model under initial impact velocities of 50 m/s and 100 m/s, in comparison with analytical models

Figure 5-53 shows that the terminations of the plastic wave propagation in models with 2mTL under impact velocities of 50 m/s and 100 m/s are not adversely affected by the end boundary effect.

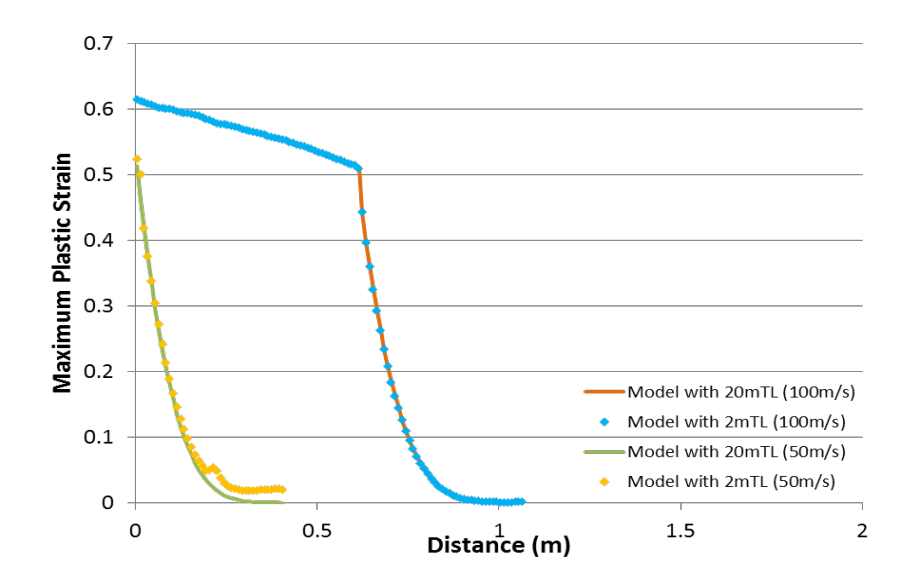


Figure 5-53: Maximum plastic strain for models with 2mTL and 20mTL, under impact velocities of 50 m/s and 100 m/s

5.4.6 Debris Damage Level vs Target's Impact Resistance

The magnitude of penetration resistance coming from the soft-catcher is one of the key considerations for designing the soft-catcher. In this thesis work, it is assumed that the material stresses at frontal face of soft-catcher are equivalent to the stresses imposed onto the concrete debris. From the effective stress-time histories plots of the target elements obtained from the numerical analysis, it is evident that Element 1 gives the highest "first" peak stress value upon first contact with the impactor. This observation remains valid even for the numerical model with 2 m target length at impact velocity of 145 m/s. Figure 5-54 shows the effective-stress-time history for model with 2m target length, with impact velocity of 145 m/s.

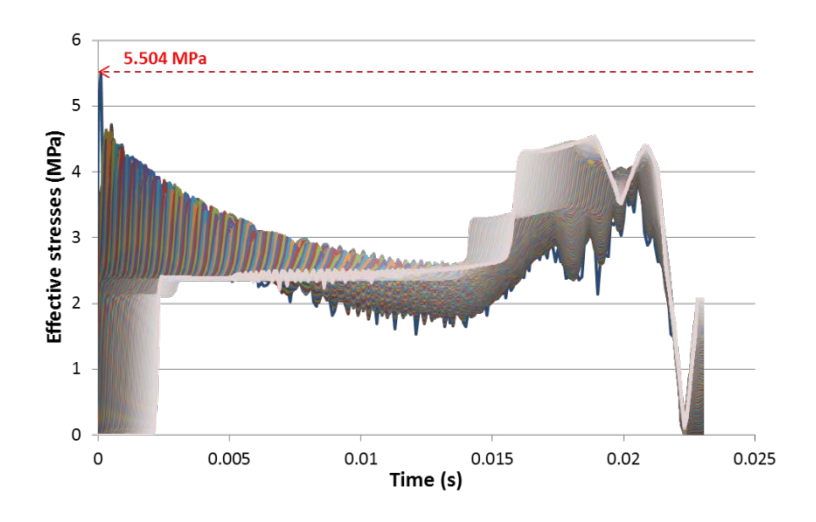


Figure 5-54: Effective stress-time histories for target elements in model with 2mTL at impact velocity of 145 m/s

Therefore, it is vital to ensure that the residual strength of concrete debris to be higher than the maximum "first" peak stress (i.e. from Element 1), in order to minimize any damage to debris during soft-catching process.

5.4.7 Penetration Distance of Debris

As discussed earlier, the numerical model with 20 m target length is unlikely to give reasonable representation of the soft-catcher's response in terms of debris penetration distance. This is due to the fact that the final travelling distance of the impactor in this numerical model includes a velocity time response regime which involves only elastic wave propagation within target material with overall thickness of 20 m. Figure 5-55 illustrates an additional distance of 0.38 m covered under the elastic wave propagation in the model with 20 m target length, under an impact velocity of 145 m/s.

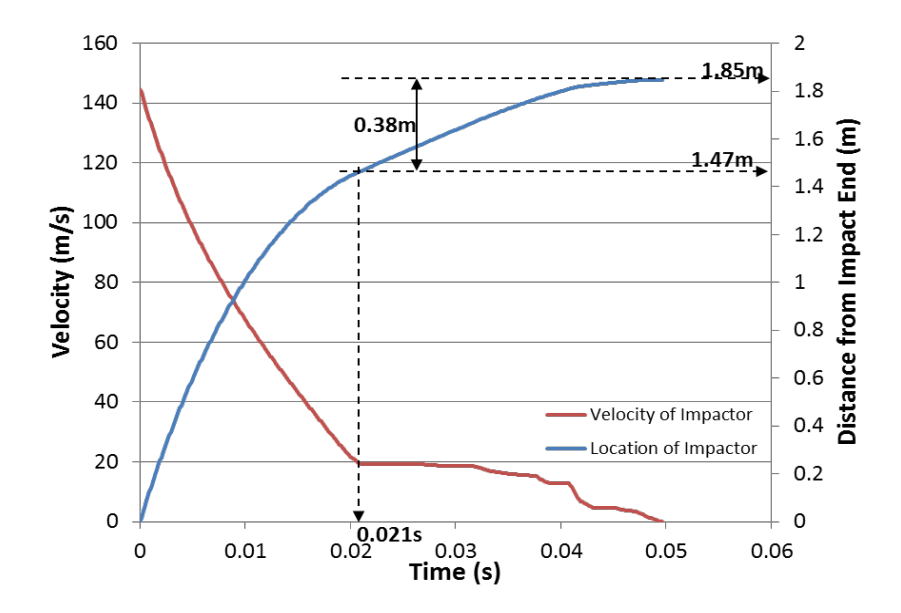


Figure 5-55: Velocity-time curve of the impactor in 20mTL model, together with the distance travelled by the impactor (with impact velocity of 145 m/s)

On the other hand, the use of model with 2 m target length will likely to result in shorter distance travelled by the impactor. Figure 5-56 presents the velocity-time curve, as well as the distance travelled by the impactor in 2mTL model. The end boundary condition for this model was assumed with full rigidity, by defining complete restraint in the impact direction for the target's end nodes.

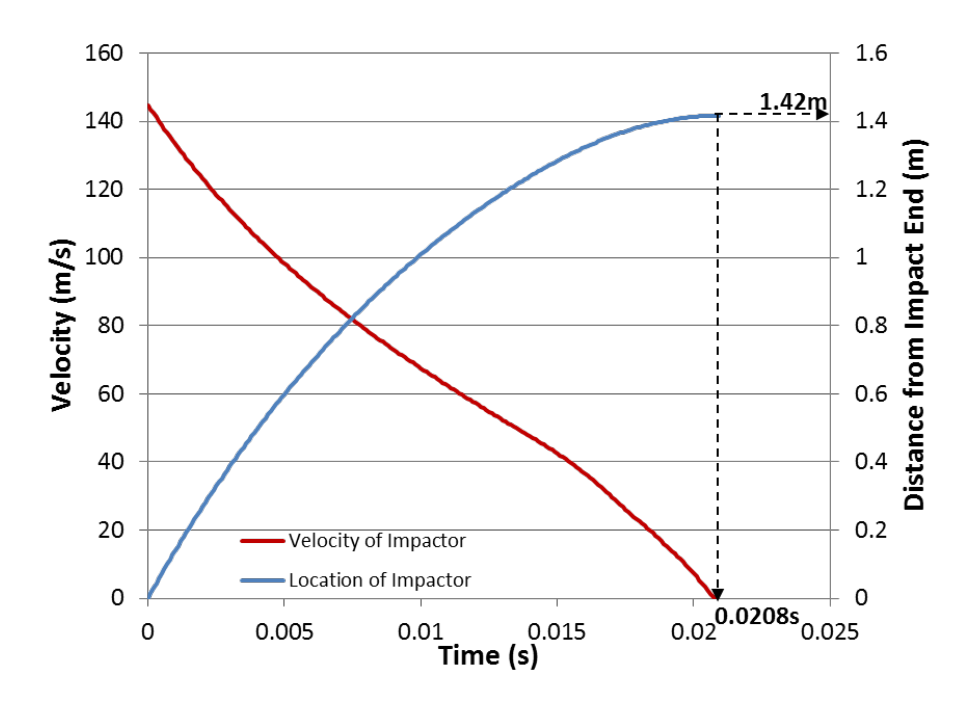


Figure 5-56: Velocity-time curve of the impactor in 2mTL model, together with the distance travelled by the impactor (with impact velocity of 145 m/s)

To take a closer look into the response (i.e. in terms of effective stresses) of target, together with the velocity-time curve of impactor, Figure 5-57 combines target's effective stress (for Element 1-200) and impactor's velocity in one single time history plot for the numerical model with 20mTL, under impact velocity of 145 m/s. The red solid line indicates velocitytime curve. It can be evidently seen that there are two distinct velocity time response regimes; (i) response under plastic and elastic wave propagation (termed as higher velocity time response regime); and (ii) response under elastic wave propagation (termed as lower velocity time response regime). The higher response regime involves propagation of both plastic shock and elastic wave, in which motion of debris is predominately governed by the plastic shock wave. Upon reaching near the elastic velocity of about 24.77 m/s, the plastic shock wave terminates. This also implies that the ending for the crushing of elements induced by the shock wave propagation. In the lower response regime, horizontal plateaus of velocity can be observed to occur with negligible level of effective stresses within the target elements. During these horizontal plateaus, there are no crushing of elements to dissipate the energies from the impactor and hence, resulted an almost constant velocity-time profile. This also implies that the impactor is moving at the same velocity as the target elements. Occasionally, slight decelerations of impactor can still be observed with accompanying stress build-up within the target elements. The occurrences of these localised decelerations are likely to be attributed by the elastic wave propagation.

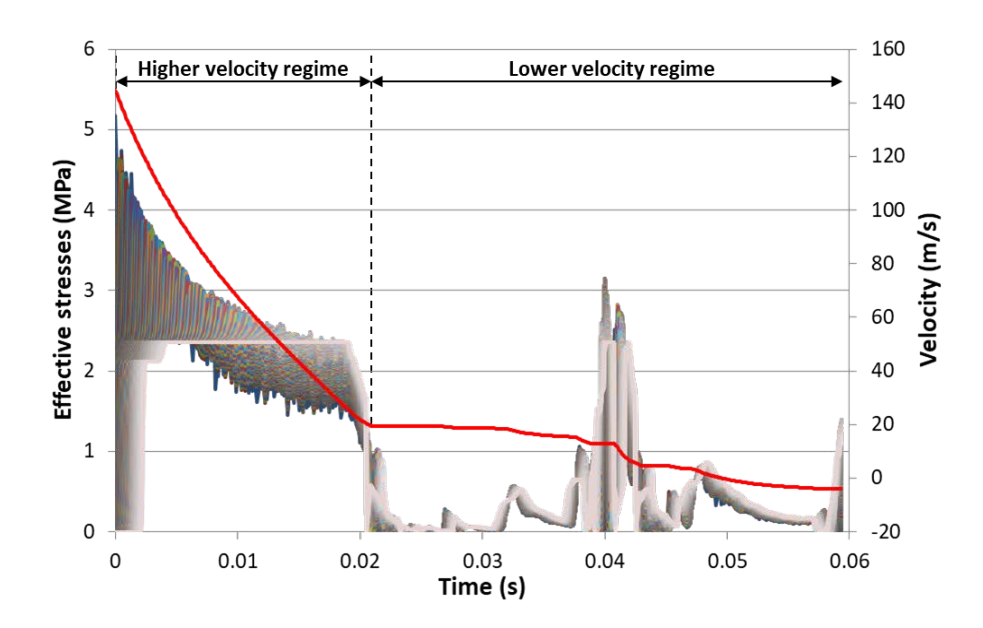


Figure 5-57: Combined plot of velocity-time curve and effective-time histories of target elements for 20mTL model

It appears that in the case of numerical model with 2 m target length, there exists no clear transition from higher to lower velocity time response regime as illustrated in Figure 5-58.

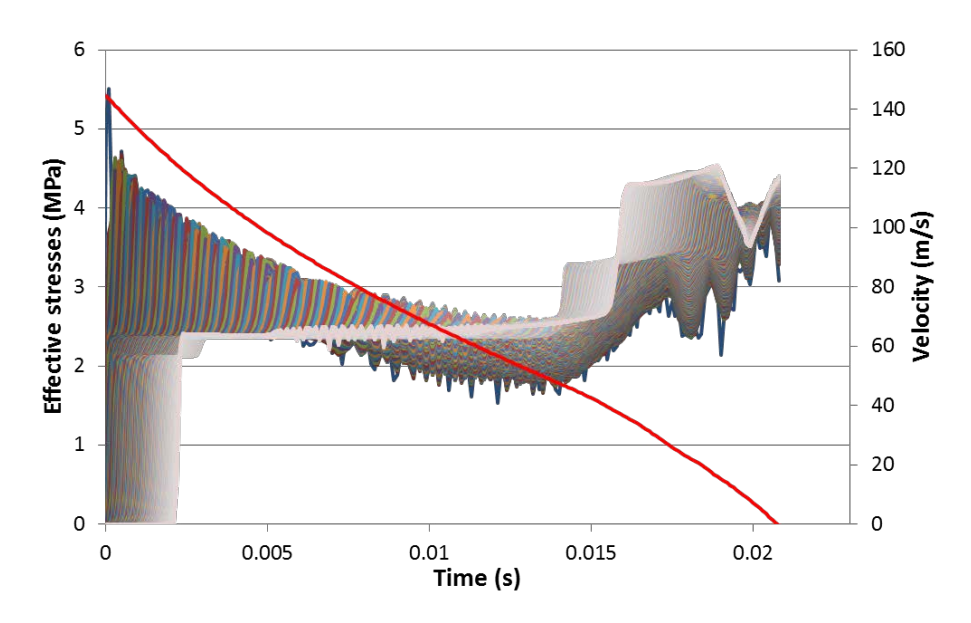


Figure 5-58: Combined plot of velocity-time curve and effective-time histories of target elements for 2mTL model

In conclusion, for the numerical model with 20 m target length, two velocity response regimes can be observed for all three impact velocities, since the end boundary effects kick-in at a later timing such that these do not affect the termination of plastic shock wave in higher velocity regime. But for the model with 2 m target length, both regimes can be seen only for the case with lower impact velocity of 50 m/s. Table 5-6 summarizes the distance of impactor covered under the respective regimes.

	M	odel with 2m	ΓL	Model with 20mTL			
Impact	Distance travelled by impactor (m)						
Velocity	Higher velocity regime	Lower velocity regime	Total	Higher velocity regime	Lower velocity regime	Total	
50m/s	0.17	0.10	0.27	0.17	0.40	0.57	
100m/s	0.78	-	0.78	0.73	0.45	1.18	
145m/s	1.42	-	1.42	1.47	0.38	1.85	

Table 5-6: Impactor's distance for model with 2mTL and 20mTL respectively

5.4.8 End Boundary Support Reaction

The end boundary support reaction forces can be extracted from the numerical model with 2m target length. Figure 5-59 presents the total global reaction forces-time histories in the X-direction (i.e. along impact direction), under different impact velocities.

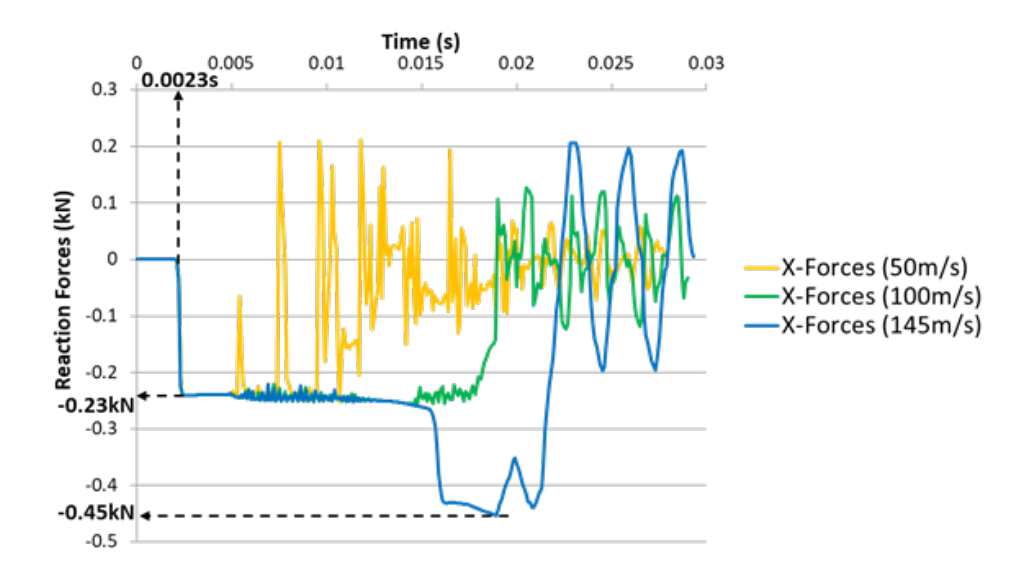


Figure 5-59: Total reaction force-time history plots for 2mTL models with different impact velocities

At approximately time t=0.0023 s, the precursor elastic stress wave induced by the wall debris impact will likely to reach the end boundary support of soft-catcher. The linear speed of elastic stress wave is determined as 866 m/s (See Equation (4.13)), having to travel a distance of 2m. This results a corresponding initial jump in reaction forces in the negative X-direction as shown in Figure 5-59. Given the elastic yielding stress of 2.36 MPa for the foam material, the total amount of force (in positive X-direction) exerted by the elastic wave onto the end boundary of this 2D model is computed as 0.236 kN, considering a surface area at end boundary of 10^{-4} m² (i.e. for element size of 0.010 m). The same amount of reaction forces of approximately 0.23 kN is observed in this initial jump for all the models, regardless of the impact velocity.

For the model with impact velocity of 50 m/s, the maximum negative total reaction force is observed to remain as the initial peak forces of 0.23 kN (i.e. resultant force due to the initial impact of elastic stress wave). For the other models with higher impact velocities, higher maximum negative total reaction force can be identified at later time. This subsequent increase in total reaction forces are likely to be caused by the presence of plastic shock wave hitting against the end support boundary. The highest total reaction force recorded for model with impact velocity of 145 m/s is about 0.45 kN in the negative X-direction. As time increases, the total reaction force in the positive X-direction reaches a maximum value of about 0.21 kN. This positive reaction forces acting in positive X-direction are induced as a result of wave reflection at the end boundary support. Furthermore, irregular and higher frequencies of stress oscillations can be seen for models with lower impact velocities. This phenomenon is likely to associate with the elastic responses for soft-catcher materials near the end support region. For the models with lower impact velocities (e.g. 50 m/s), crushing of materials is unlikely to occur near the support end which implies that these materials are still in elastic state. On the contrary, the higher impact velocities will have resulted plastic responses of materials near the support end due to larger extent of crushing zone.

5.4.9 Further Mesh Sensitivity Study

So far, the smallest element size considered in the previous modelling is 0.010 m. A further mesh sensitivity study involving element sizes of 0.005 m, 0.0025 m and 0.001 m is performed to examine possible convergence of numerical results. Figure 5-60 presents the velocity-time histories of numerical models with different element sizes. It is observed that for both cases with impact velocities of 100 m/s and 145 m/s, the decreasing rates of velocities seem to be consistent. In contrary, the numerical models with lower impact velocity (i.e. 50 m/s) appear to be more sensitive to the decrease in element sizes, though the results obtained from model with element size of 0.001 m look dubious to be valid. Table 5-7 shows the distances travelled by the impactors in the various models.

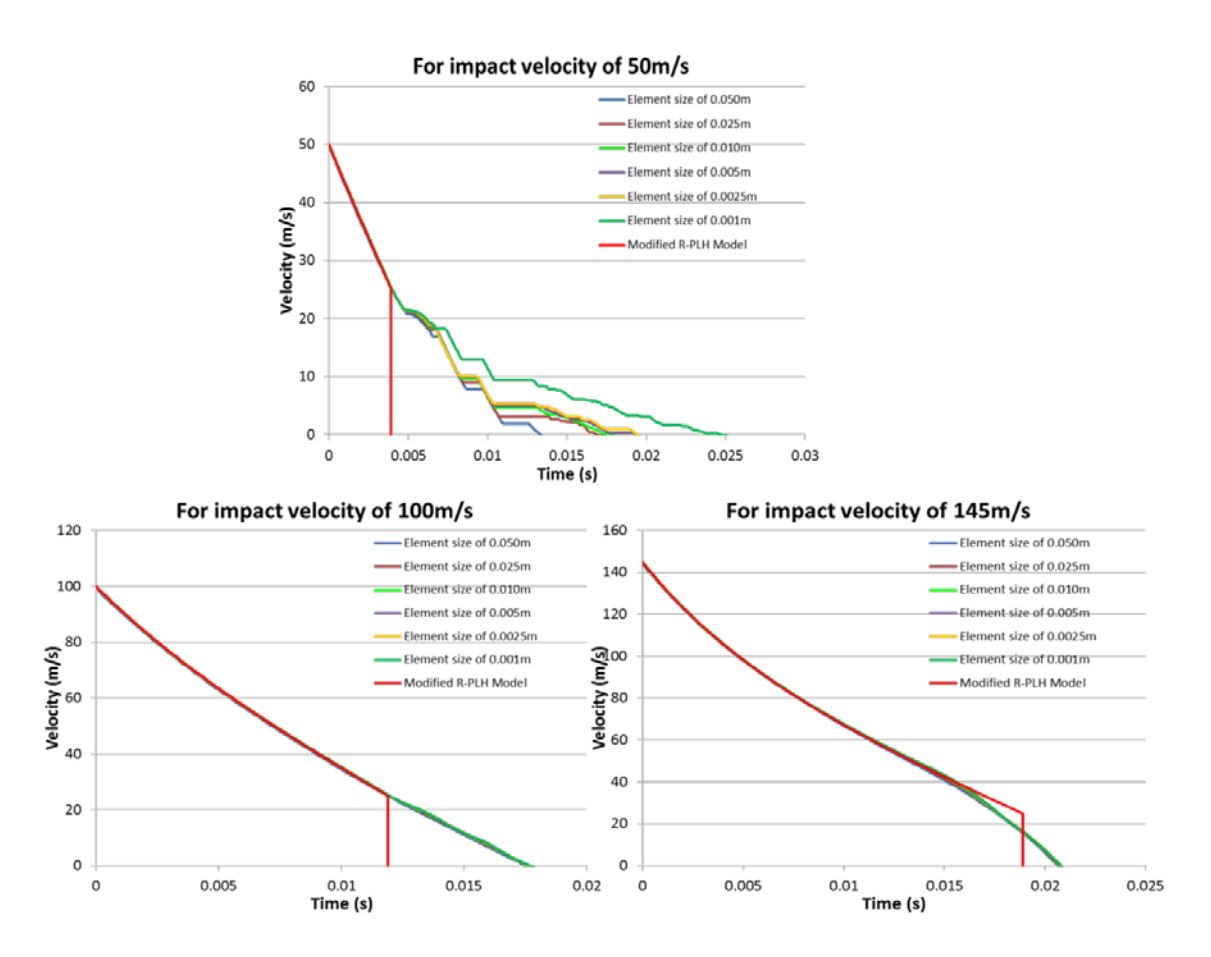


Figure 5-60: Velocity-time history plots of numerical models with different element sizes

		Distance travelled by impactor (m)					
Impact Velocities	Analytical Prediction	Numerical Prediction - Element sizes					
(m/s)	(Modified R- PLH Model)	0.050m	0.025m	0.010m	0.005m	0.0025m	0.001m
50	0.149	0.246	0.260	0.269	0.273	0.277	0.330
100	0.707	0.768	0.774	0.778	0.779	0.780	0.781
145	1.425	1.400	1.410	1.416	1.418	1.420	1.421

Table 5-7: Travelled distances of impactors in models with different element sizes

Likewise, the peak stresses from various numerical models with different element sizes, in relation to the Modified R-PLH Model's predictions, are presented and plotted in Table 5-8 and Figure 5-61. Note that for comparison to be representative, these peak stresses of elements are obtained at the same position (i.e. 0.025 m from the impactor's end) where the integration point of 1st element in model with element size of 0.050 m are located. It is evidently shown that convergence of numerical results is achieved with element size of 0.010 m or smaller.

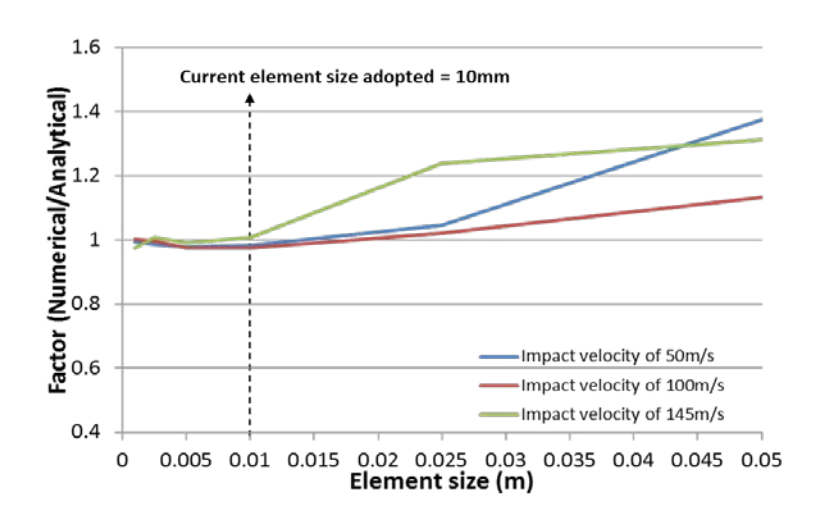


Figure 5-61: Ratio of numerical over analytical stresses, with change in element sizes

	Initial Shock Stress (MPa)						
Impact Velocities	Analytical Prediction	Numerical Prediction - Element sizes					
(m/s)	(Modified R- PLH Model)	0.050m	0.025m	0.010m	0.005m	0.0025m	0.001m
50	2.484	3.417	2.596	2.441	2.429	2.448	2.466
100	3.299	3.733	3.364	3.212	3.212	3.292	3.309
145	4.601	6.039	5.699	4.637	4.564	4.641	4.480

Table 5-8: Peak stresses of elements in comparison with Modified R-PLH Model's predictions

Likewise, Figure 5-62 and Table 5-9 show the comparisons for the volumetric strain. Convergence of numerical results can be observed with element size of 0.010 m or smaller.

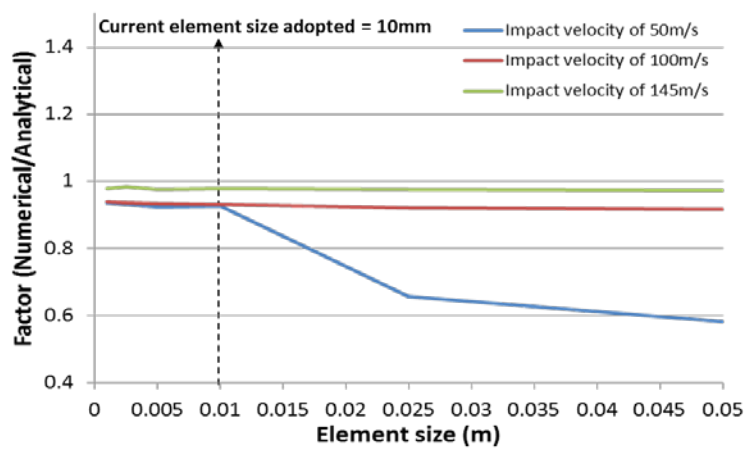


Figure 5-62: Ratio of numerical over analytical strain, with change in element sizes

		Initial S	Shock Stra	ain (Volum	netric strai	in)	
Impact Velocities (m/s)	Analytical Prediction	Numerical Prediction - Element sizes					
((Modified R- PLH Model)	0.050m	0.025m	0.010m	0.005m	0.0025m	0.001m
50	0.593	0.345	0.39	0.549	0.548	0.552	0.555
100	0.691	0.633	0.636	0.644	0.645	0.647	0.649
145	0.738	0.718	0.721	0.722	0.721	0.725	0.723

Table 5-9: Volumetric strain of elements in comparison with Modified R-PLH Model's predictions

5.4.10 Concluding Remarks

For cases where higher impact velocities are involved, the velocity-time curve from the model with 2 m target length (2mTL) is observed to deviate from the other model with 20 m target length, at some point of time (i.e. before or at the elastic velocity). Before this timing of deviation, the peak effective stresses of elements for both 2mTL and 20mTL model relate fairly well, which also attributes to the consistencies in velocity-time curve. Beyond this timing, the elements experience surge in stresses that associate well with the increase in deceleration of impactor.

The presence of end boundary condition may to certain extent influence the plastic wave propagation, especially when higher impact velocities are involved. This implies that a clear transition between two different velocity time response regimes may no longer exist. This two distinct response regimes can be identified from the velocity-time curve of impactor; response under plastic and elastic wave propagation (termed as higher velocity time response regime) and response under elastic wave propagation (termed as lower velocity time response regime). For the 20mTL model, both regimes can be observed under all three impact velocities. But for the 2mTL model, only the case with 50 m/s experiences both regimes, while the cases with higher impact velocities experiences no clear transition between these two velocity regimes.

To conclude, the use of maximum "first" peak stress for Element 1 in either model of 2mTL or 20mTL remain valid as parameter to check against the residual strength of debris, since this particular peak stress remain the highest upon first instance of impact. Nonetheless, slight increases in these initial peak stresses are observed for models with different impact velocities. In contrast, the total distance travelled by the impactor (i.e. also referred as the penetration distance of debris) can be affected by the overall length of target, due to presence of lower velocity regime as identified earlier. Therefore, the total distances of impactor obtained from the 2mTL model will be more appropriate to consider as the design parameters for the soft-catcher. Table 5-10 compares the analytical and numerical predictions for the soft-catcher design parameters.

The effects of change in element sizes are observed to be more evident in numerical models with low impact velocity of 50 m/s. The use of element size of 0.010 m or smaller appears to

achieve convergence of results, particularly the peak stresses and strains. The two-dimensional numerical models of debris-soft catcher system in the upcoming sections will be developed with element size of 0.010 m.

Outputs	R-PLH Model	Modified R-PLH Model	Numerical Model (2m target length)			
For impact velocity of 50m/s						
Maximum stress on debris (MPa)	2.783	2.484	2.637			
Debris penetration distance (m)	0.190	0.149	0.270			
Time of penetration (ms)	7.94	4	17.4			
For impact velocity of 100m/s						
Maximum stress on debris (MPa)	3.893	3.299	3.326			
Debris penetration distance (m)	0.692	0.707	0.780			
Time of penetration (ms)	15.89	11.95	17.6			
For impact velocity of 145m/s						
Maximum stress on debris (MPa)	5.417	4.600	5.504			
Debris penetration distance (m)	1.316	1.425	1.420			
Time of penetration (ms)	23.04	19.1	20.7			

Table 5-10: Analytical and numerical predictions of soft-catcher design parameters

5.5 2D Numerical Model of Soft-Catcher

The previous section demonstrates the differences of results obtained by comparing between a simple 1D numerical model which considers the effects of end boundary restraint and the modified 1D analytical model. The upcoming discussions will focus on the effects of the debris-soft catcher interaction in a two-dimensional space, highlighting the influences coming from material failure resistances. However, these sections will specifically examine material responses that influence the eventual design of soft-catcher. These refer to the penetration distance of wall debris, impact stresses on wall debris and support reaction forces on the lateral and end boundary restraints.

5.5.1 2D Model - With Tensile and Shear Resistances

This 2D model takes into account of the lateral support restraints, which implies that tearing resistance based on foam material's failure stresses will be incorporated into the numerical analysis. Normally under this circumstance, the wall debris along the impact direction will encounter additional motion resistance due to the tensile and shearing effect. However, there are uncertainties in the overall responses of soft-catcher that need to be investigated, as more foam material directly above the material crushing zone will influence the plastic/elastic wave propagation within the soft-catcher. The development of material stresses and strains over

time will likely to deviate from the phenomenon observed in the 1D model. The numerical results (i.e. target material stresses and strain; impactor's velocity and travelling distance; support reactions) obtained will be compared against 1D numerical and analytical model. This is to examine the significance of the target material failure along the pre-defined tearing line within the soft-catcher. Furthermore, support reaction forces will be extracted to facilitate future design of the soft-catcher system. The top and front views of the impact scenario are illustrated in Figure 5-63.

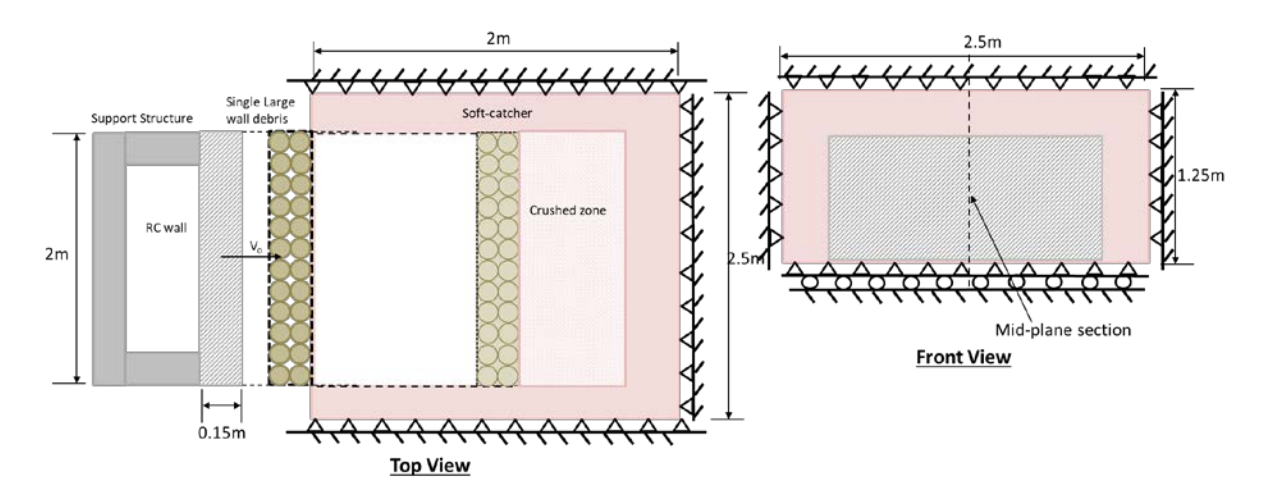


Figure 5-63: Top and front view of debris-soft catcher scenario

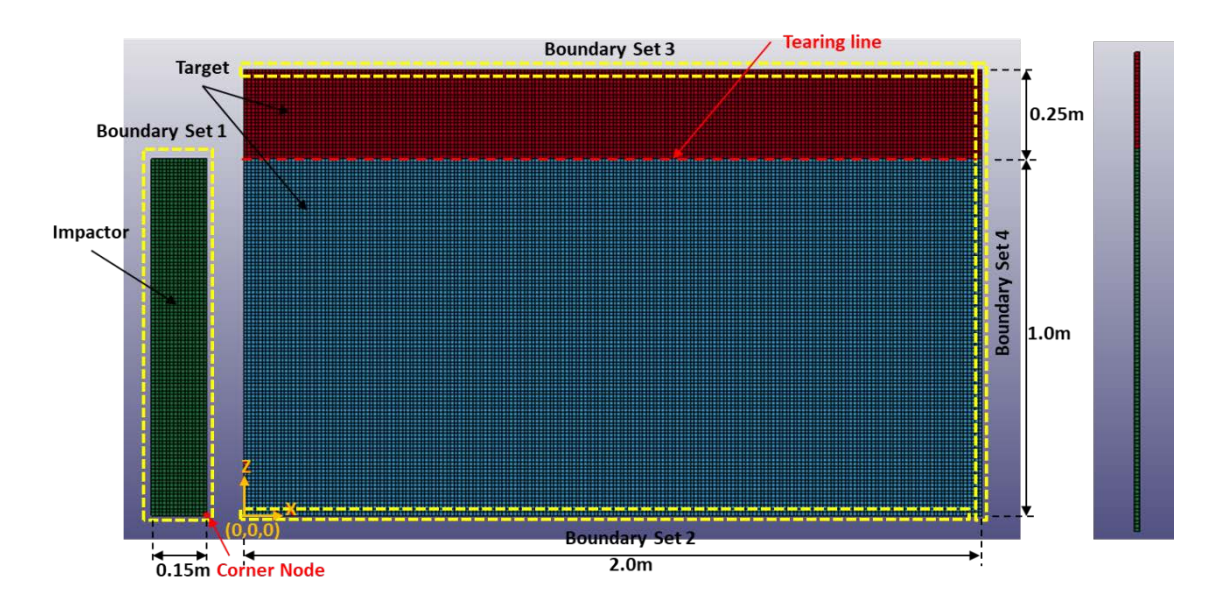


Figure 5-64: Elevation and front view of 2D model with specified boundary conditions

The 2D model as shown in Figure 5-64 shall essentially represents the response of the soft-catcher at the mid-plane section (See Figure 5-63). The overall length of the soft-catcher is limited to 2m, with a height of 1.25 m. The thickness of both the wall debris and soft-catcher in the 2D model is defined by the element size of 0.010 m in the y-direction. The relevant boundary conditions are defined as shown in Figure 5-64. The translational restraints for the respective boundary sets are listed in Table 5-11. No rotational restraints are prescribed.

Boundary	T	Translational restraints			Rotational restraints		
Set	X	Y	Z	X	Y	Z	
1	No	Yes	Yes	No	No	No	
2	No	Yes	Yes	No	No	No	
3	Yes	Yes	Yes	No	No	No	
4	Yes	Yes	Yes	No	No	No	

Table 5-11: Boundary conditions defined for the 2D model

Similar set of input cards previously used for 1D numerical models are considered for this 2D model. The use of segment-based contact search (i.e. CONTACT-AUTO-SURFACE-TO-SURFACE) for penetration provides a better option over the nodal-based contact search, especially when the impact scenario involves sharp corners of different PARTs. To enable processing of the global forces from the end boundary conditions, keyword cards; DATABASE-NODFOR and DATABASE-NODAL-FORCE-GROUP are included.

An additional contact algorithm known as CONTACT-AUTO-SURFACE-TO-SURFACE-TIEBREAK in LS-DYNA is utilized to account the tearing resistances arising from the foam material's shear and tensile failure stresses. To achieve this, the soft-catcher is modelled with two different PART IDs, in order to allow the insertion of the contact interface along the predefined tearing line. This contact option will be further discussed in the next subsection. Furthermore, to evaluate the contact stresses (e.g. interface shear and normal stresses) along the pre-defined tearing line, a set of interface database can be called upon by including keyword cards; DATABASE-BINARY-INTFOR and DATABASE-EXTENT-INTFOR, and set MPR and SPR in the *CONTACT card to 1. Setting MPR and SPR to 1 allow the extraction of contact database for the master and slave component respectively. However, an additional line "s=filename" will need to be written in the LS-DYNA execution line for the database to be generated.

Finally, the following list shows the set of input cards required for the 2D (actual) models, with the additional cards highlighted in blue.

CONTROL_TERMINATION
CONTROL_TIMESTEP
DATABASE_NODFOR
DATABASE_NODAL_FORCE_GROUP
DATABASE_BINARY_INTFOR
DATABASE_EXTENT_INTFOR
DATABASE_EXTENT_INTFOR
DATABASE_BINARY_D3PLOT
BOUNDARY_SPC_SET
SET_NODE
CONTACT_AUTO_SURFACE_TO_SURFACE
CONTACT_AUTO_SURFACE_TO)_SURFACE_TIEBREAK
CONTACT_INTERIOR

PART
SECTION_SOLID
MAT_RIGID
MAT_CRUSHABLE FOAM
HOURGLASS
INITIAL_VELOCITY
ELEMENT_SOLID
NODE
SET_PART_COLUMN

5.5.1.1 Tie-Break Contacts

Tie-break contact options in LS-DYNA allow the modelling of interface between different entities such that compressive and tensile stresses can be transmitted with optional built-in failure criterions. The resisting tie forces between the slave and master components defined along the contact interface are formulated through linear contact spring, in which the contact penalty stiffness is internally computed. Once the stress failure criterion is reached, the tensile coupling effect is removed and the nodes or segments between slave and master components are separated. Upon failure, traditional surface to surface contact algorithm kicks in. Note that the frictional resistance is not taken into account in the modelling.

In this 2D numerical model, the CONTACT-AUTO-SURFACE-TO-SURFACE-TIEBREAK is activated with response parameter OPTION 2. This response option generally allows the definition of stress-based failure criterion. The failure envelope and criterion are shown in Figure 5-65. The user-defined parameters include the NFLS, which refers to the tensile failure stress and the SFLS, which refers to the shear failure stress. According to the experimental work done by Arezoo in [22], the tensile and shear stress to failure for the material of interest are 2.17 MPa and 1.86 MPa respectively. The part of soft-catcher that remains uncrushed is defined as the master component while the other crushing part is defined as the slave component.

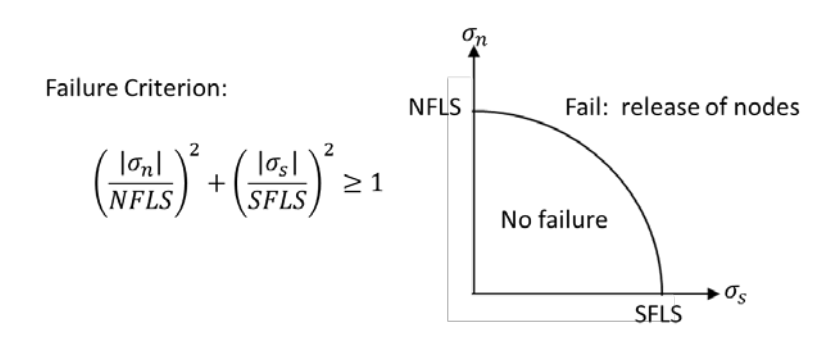


Figure 5-65: Failure criterion and failure envelope of tie-break connection (with response OPTION 2)

The use of this tie-break contact option vastly simplifies the modelling of failure mechanism within the soft-catcher. This approach assumes that the foam material predominately fails along the pre-defined tearing line. In contrast, the use of element erosion technique (i.e. continuum-based material failure) will likely to give a more realistic material response of the soft-catcher. However, one shall be aware that using element erosion technique tends to

increase the risk of model inaccuracies especially when severe deformations of elements in soft material are expected. Error terminations of analyses can occur due to negative volumes of highly distorted elements.

Realistically, crushing of foam material can also occur within the overlying region above the tearing line, as the wall debris cloud expands further. This will influence the interaction between the debris and soft-catcher. Considering that the crushing failure of foam material will predominately localised within the impact region (i.e. below the tearing line), it is reasonable to assume tearing line failure. On the other hand, with further increases in the overlying thickness of soft-catcher (i.e. more than 0.25 m), the inaccuracies due to this simplification of tearing line failure may become more significant.

5.5.1.2 Velocity-Time History of Wall Debris

The velocity-time history in X-direction for bottom right corner node of impactor in this 2D model as identified in Figure 5-64, are plotted in Figure 5-66, against both the 1D numerical and analytical model previously presented in Section 5.4 under different impact velocities. It can be seen that during the initial phase of impact duration, the decelerations of debris in all 2D models relate fairly well with the 1D model predictions. In the 2D models with impact velocities of 50 m/s and 100 m/s, debris decelerations appear to slow down towards the later phase of the impact process. There are two arguments that can possibly support this observation. First, in 1D model, the elastic waves propagate only in the X-direction (i.e. along the impact direction). However, the 2D model allows elastic waves to propagate in both X and Z-direction, which implies that vertical stress waves are likely to weaken the horizontal stress waves that oppose the debris motion. Second, the opening that forms along the tearing interface in 2D model allows vertical translations of nodes within the soft-catcher. With multiple elastic waves reflection in the 2D space domain, losses in contact between debris and frontal face of soft-catcher can occur and result in further reduction of compressive stresses (i.e. in the X-direction) within the soft-catcher that resist the debris motion. However, it is apparent to see that the differences between velocity-time curves of these models reduce as the initial impact velocity of debris increases. The 2D model with higher impact velocity of 145 m/s shows a rather similar deceleration profile with the 1D numerical model. The resultant travelling distances of the wall debris in the 2D models are presented in Table 5-12, in comparison with the 1D numerical and analytical model predictions.

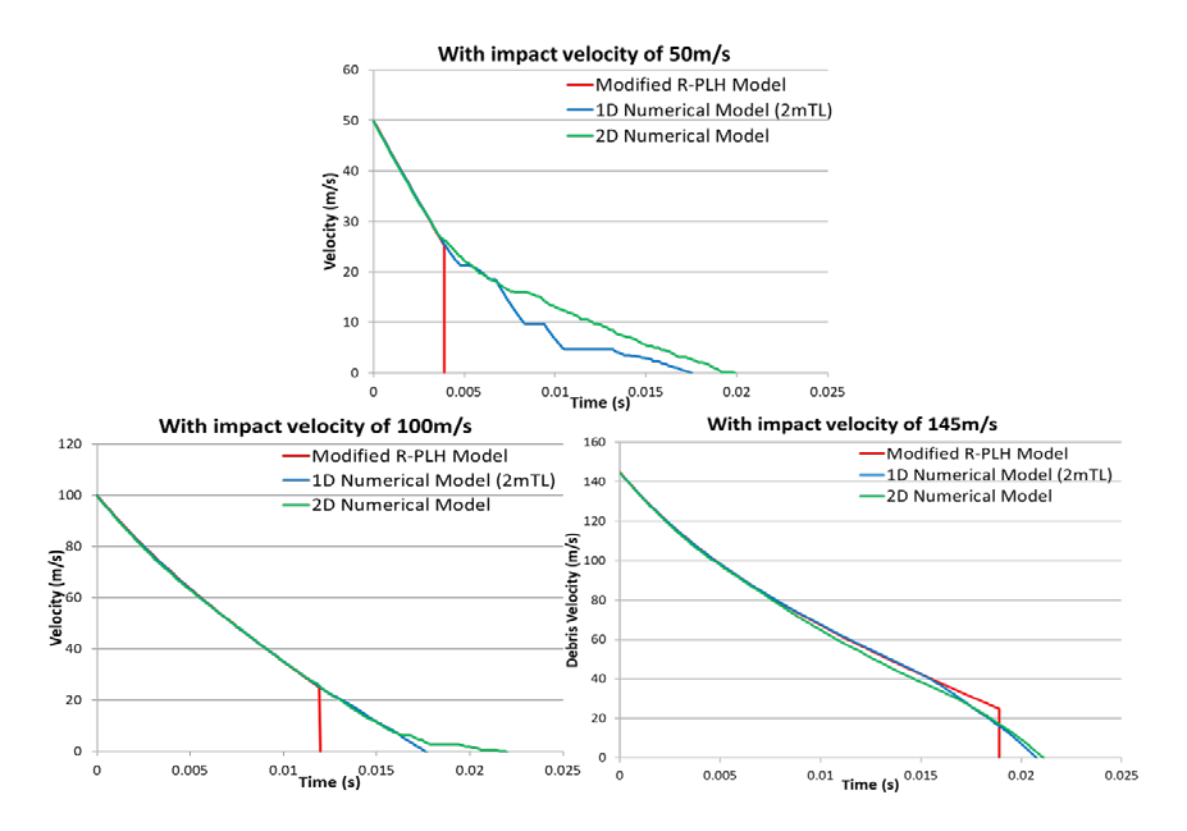


Figure 5-66: Comparison of velocity-time curves of impactors in 2D, 1D numerical and analytical model

	Distance travelled by impactor (m)					
Impact Velocities (m/s)	Analytical Prediction	Numeric	al Prediction			
(,	(Modified R-PLH Model)	1D	2D			
50	0.149	0.269	0.318			
100	0.707	0.780	0.785			
145	1.425	1.420	1.390			

Table 5-12: Comparison of overall distance travelled by impactors in 2D, 1D numerical and analytical models

5.5.1.3 Material Stresses of Soft-Catcher

From Figure 5-66, it can be clearly seen that the debris in models with impact velocities of 50 m/s and 100 m/s experience noticeable decrease in decelerations, as compared to the impactor in 1-D numerical models. These decreases in debris deceleration are associated with compressive stress-time histories of elements along the front face of soft-catcher.

With reference to the models with impact velocities of 100 m/s, Figure 5-67 compares the averaged compressive-stress time histories of all elements located at the impact end of soft-catcher, with the stresses of Element 1 in 1D numerical model. It is found that the elements in 2D Model experience larger stress oscillations during the penetration process. These

consequently result in lesser momentum transfers from the debris and hence, decrease in debris deceleration.

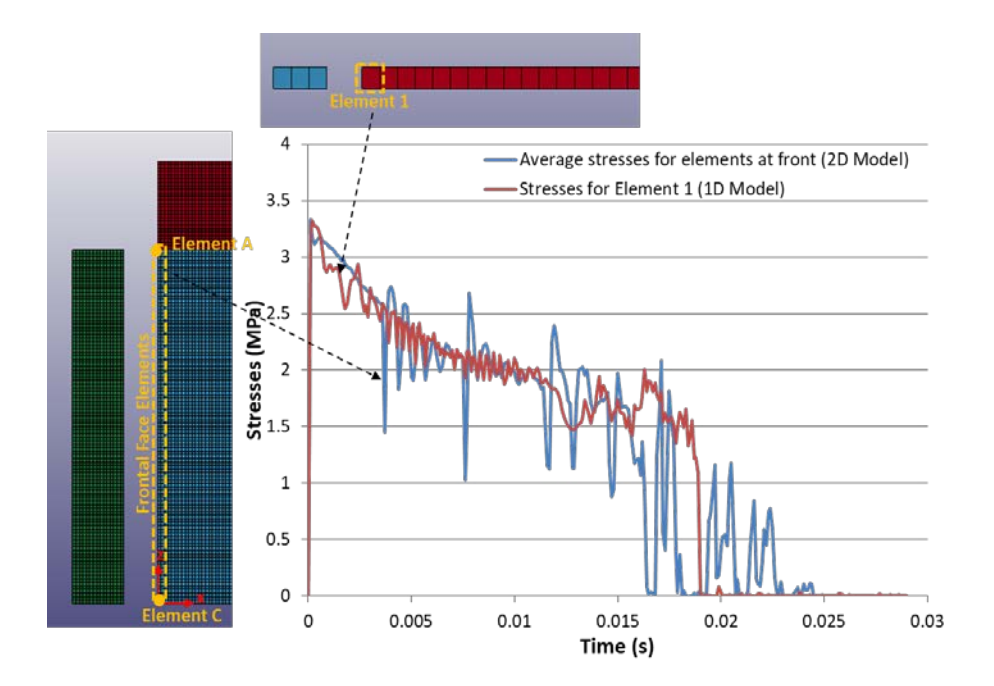


Figure 5-67: Compressive stresses-time histories of front elements in 2D and 1D Model (with impact velocity of 100 m/s)

There are few possible reasons that can justify the occurrence of stress oscillations observed in the 2D Model. These include sudden losses of connectivity of nodes along the tearing interface due to material failure, or losses of contact at front interface between debris and soft-catcher. Figure 5-68 compares the stresses-time histories of selected elements in 2D Model, with the differences in nodes' coordinates in X-direction. The positive differences in nodes' coordinates indicate losses in contact between debris and soft-catcher. Indeed, the sharp reductions in stresses of elements can be related to the losses in contact between debris and soft-catcher at front interface.

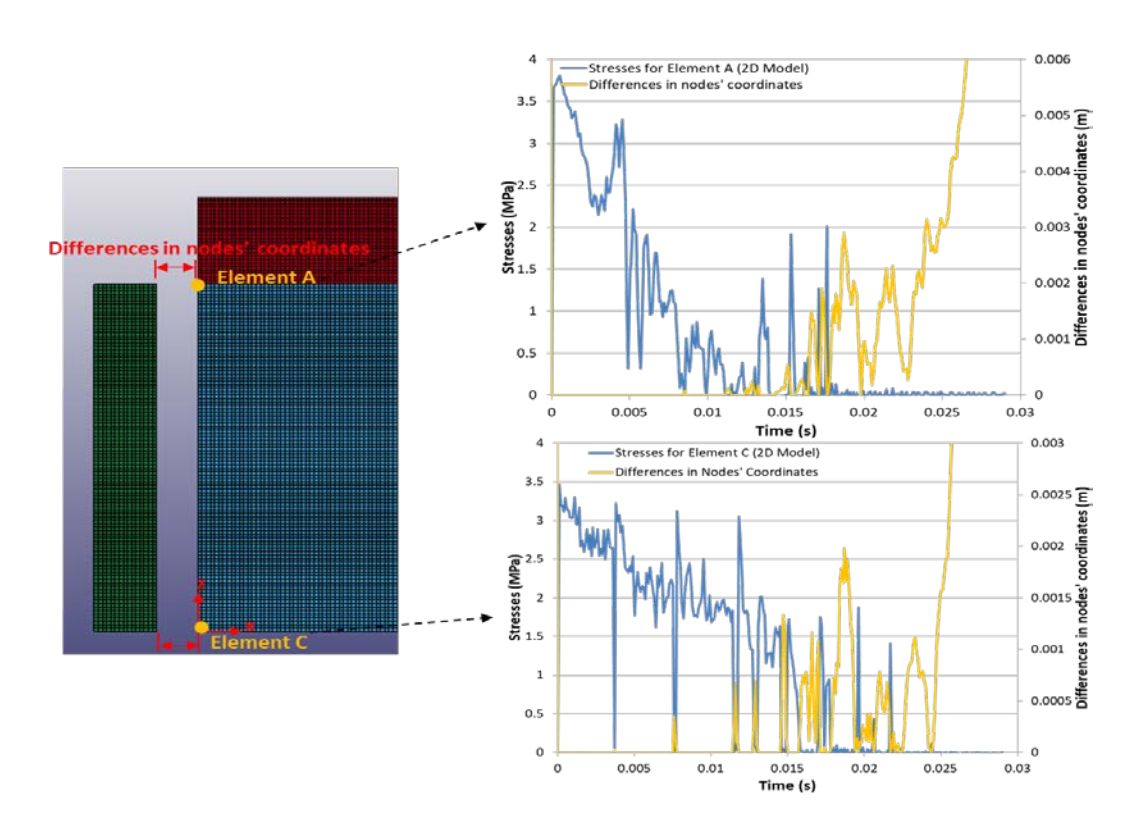


Figure 5-68: Compressive stress-time histories of elements in 2D Model (with impact velocity of 100 m/s), with indications of contact losses at selected locations

Figure 5-69 further substantiates these findings by presenting the similar comparison for the case of 1D numerical model.

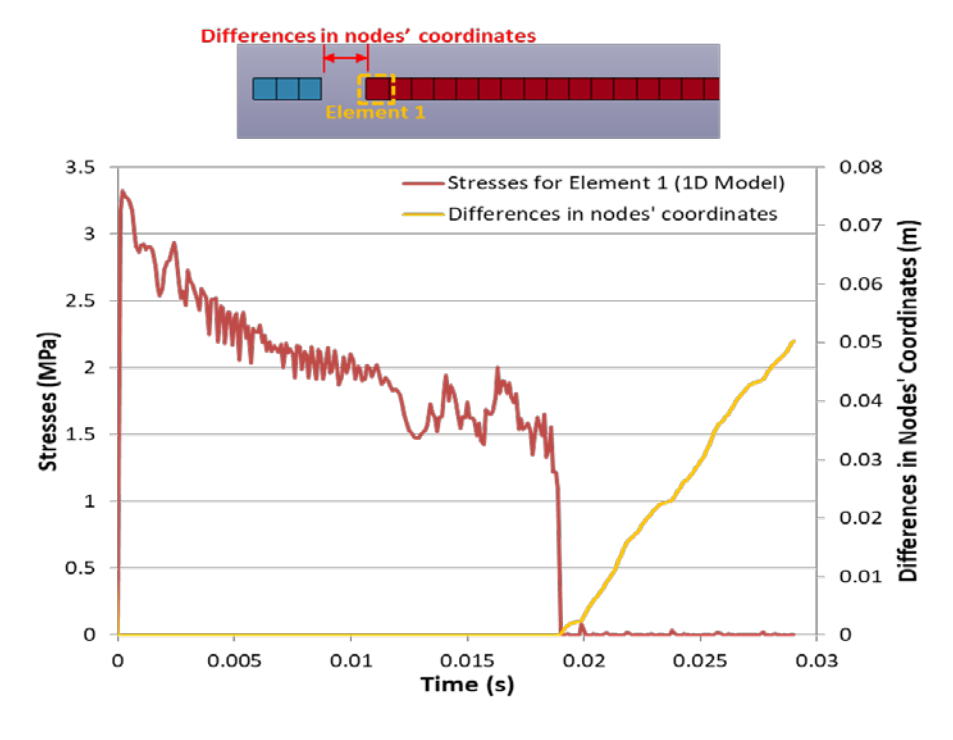


Figure 5-69: Compressive stress-time histories of elements in 1D Model (with impact velocity of 100 m/s), with indications of contact losses at impact end

To evaluate the impact stresses acting on the debris, it is relevant to examine the compressive stress-time histories of elements located over the frontal face of the soft-catcher. As such, the stress-time histories of selected elements along the frontal face of the soft-catcher in 2D Model are plotted against the Element 1 in 1D numerical model, under different impact velocities as shown in Figure 5-70, Figure 5-71 and Figure 5-72.

It can be seen that the 1D model prediction of impact resistance is apparently lower than the one obtained from the 2D model. It is visibly noted that regardless of impact velocities, the stresses for Element A (as identified in Figure 5-68) appear to give the highest magnitude, as compared to the Element C. This could be attributed to the fact that Element A, which is located right at the tearing edge of the soft-catcher, experiences the highest amount of shear resistance against the motion of wall debris. Furthermore, the development of stresses for models with lower impact velocities (i.e. 50 m/s and 100 m/s) exhibit more drastic oscillations as compared to the model with higher impact velocity of 145 m/s. This phenomenon is related to the losses in contact between debris and soft-catcher at frontal interface.

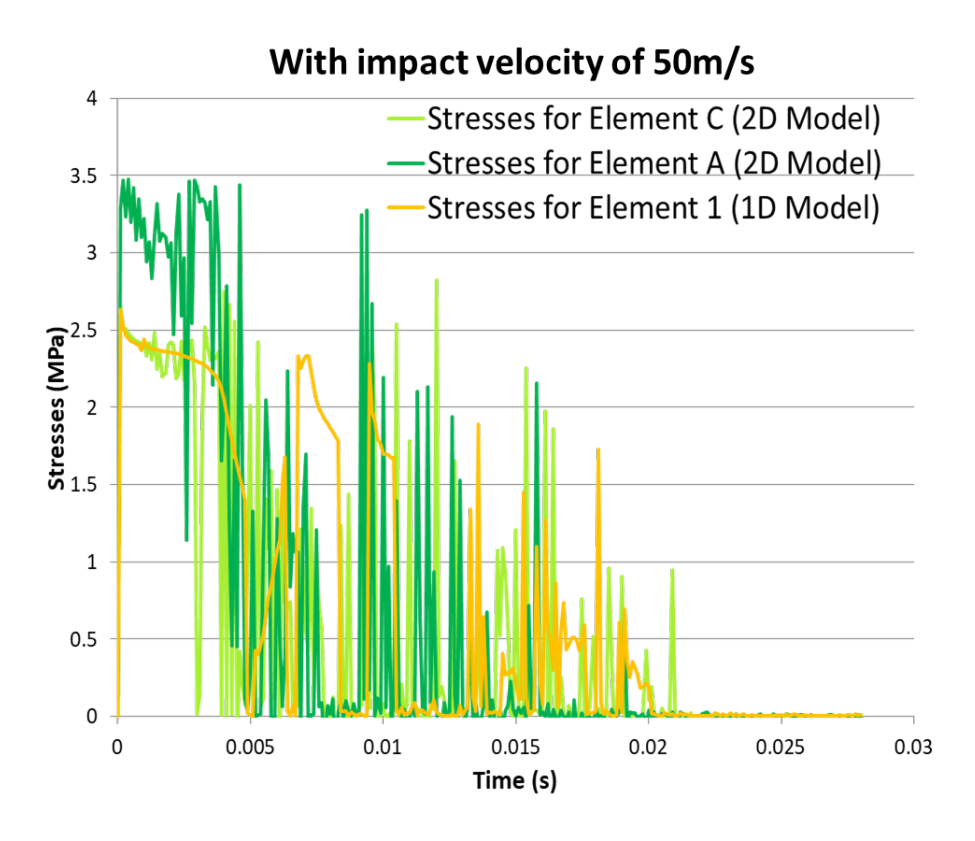


Figure 5-70: Compressive stress-time histories of selected elements over the height of impactor end, in comparison with corresponding element in 1D numerical model (for impact velocity of 50 m/s)

With impact velocity of 100m/s Stresses for Element C (2D Model) Stresses for Element A (2D Model) 3.5 Stresses for Element 1 (1D Model) 3 2.5 Stresses (MPa) 2 1 0.5 0 0.025 0.005 0.03 0 0.01 0.015 0.02 Time (s)

Figure 5-71: Compressive stress-time histories of selected elements over the height of impactor end, in comparison with corresponding element in 1D numerical model (for impact velocity of 100 m/s)

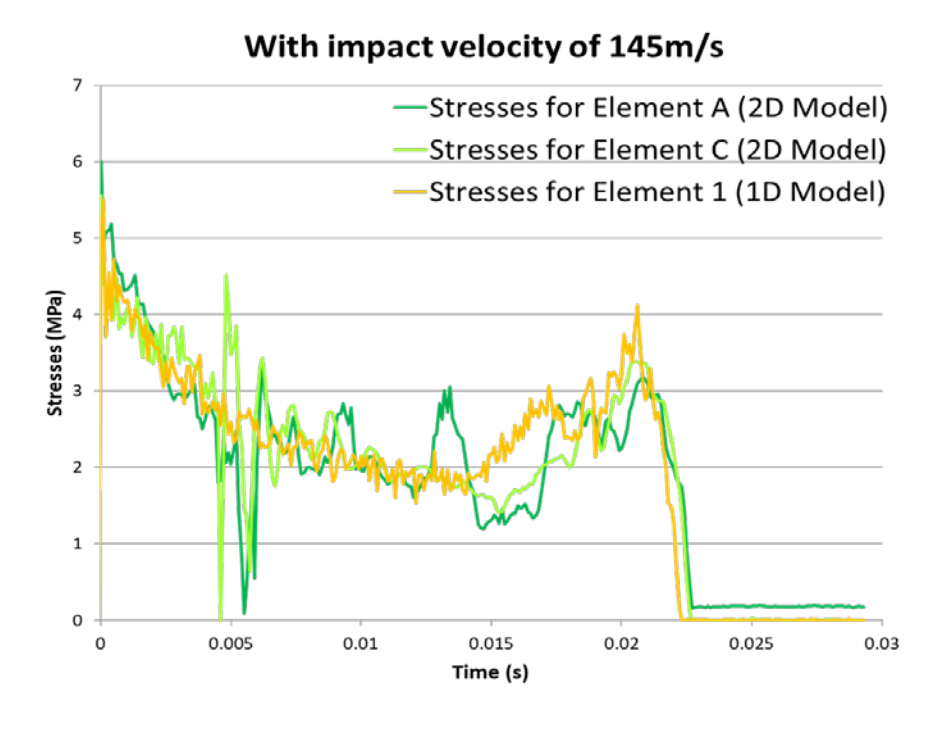


Figure 5-72: Compressive stress-time histories of selected elements over the height of impactor end, in comparison with corresponding element in 1D numerical model (for impact velocity of 145 m/s)

To emphasize that the tensile stress development in 2D model is one key aspect that differs from 1D model, Figure 5-73, Figure 5-74 and Figure 5-75 present the contour plots of maximum principal (tensile) stresses for models under various impact velocities, at penetration termination time (i.e. equivalent to the time when velocity of debris reaches zero). It can be clearly seen that the region closer to the lateral support restraint experiences higher tensile stresses.

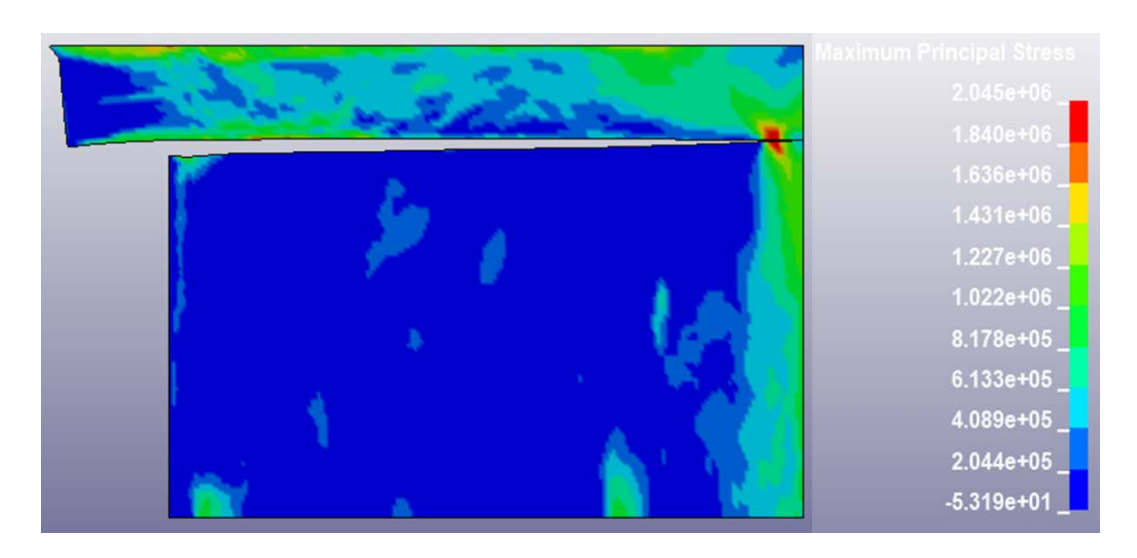


Figure 5-73: Contour plot of maximum principal stresses (tensile) for model with impact velocity of 50 m/s (at time t = 0.0199 s)

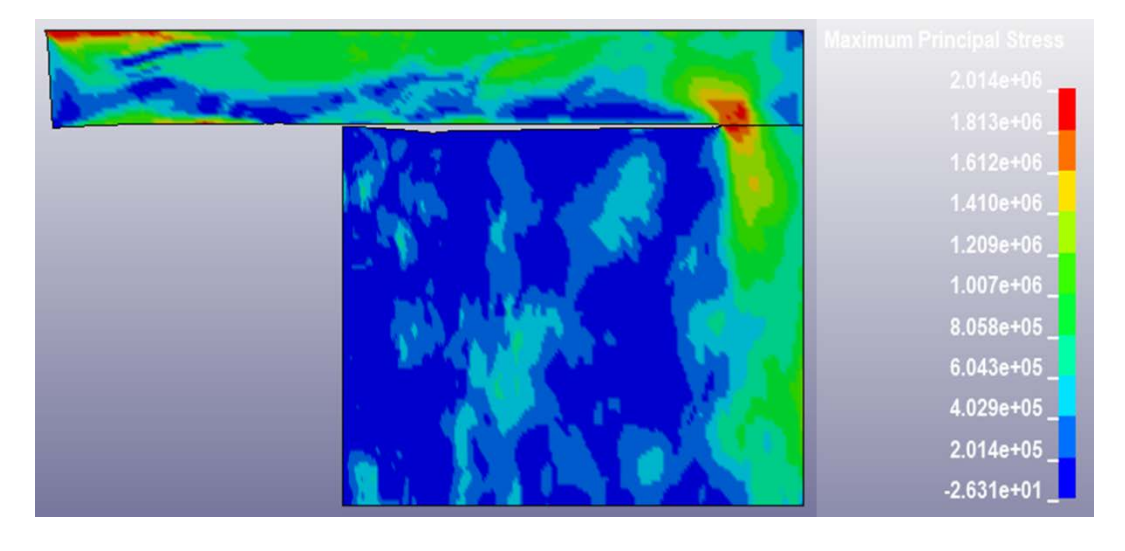


Figure 5-74: Contour plot of maximum principal stresses (tensile) for model with impact velocity of 100 m/s (at time t = 0.022 s)

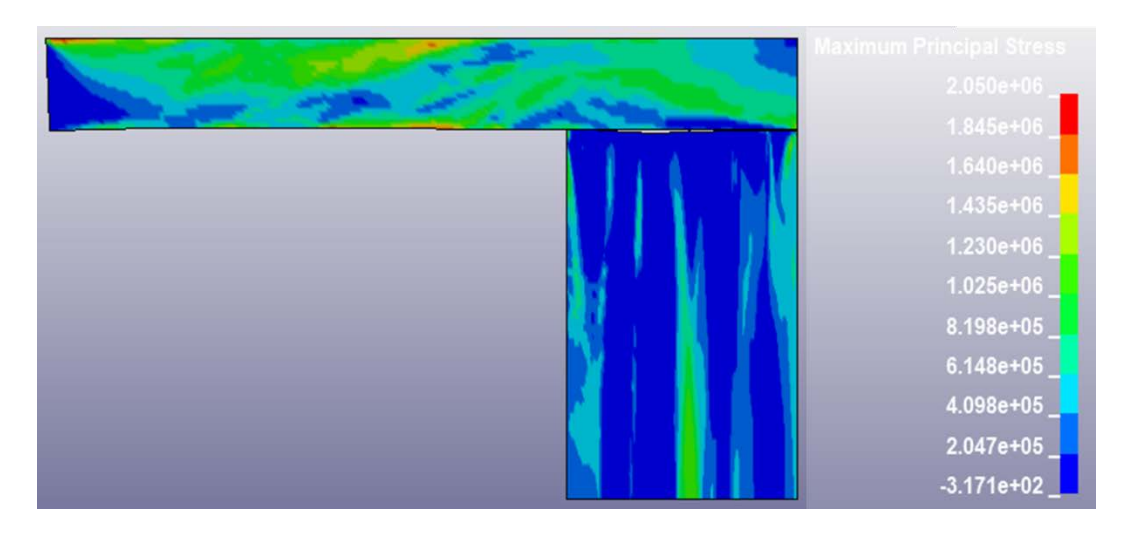


Figure 5-75: Contour plot of maximum principal stresses (tensile) for model with impact velocity of 145 m/s (at time t = 0.0211 s)

5.5.1.4 Material Strains of Soft-Catcher

According to D. Zenkert [23], the tensile strain to failure for brittle foam such as Rohacell (PMI) type is typically between 2% to 3%. Hence, by assuming that the tensile failure strain is set at 2.5%, Figure 5-76, Figure 5-77 and Figure 5-78 highlight the part (in magenta color) of the soft-catcher in which the effective plastic strain exceeds 0.0247. The effective plastic strain of 0.0247 corresponds to the volumetric strain of -0.025 (tensile failure strain). These figures give an approximated indication of the locations in which tensile failure of soft-catcher is likely to occur at the end of termination time.

The material failure for soft-catcher above the tearing line can occur as long as the overlying region plays a significant role in influencing the debris penetration phenomenon. However, as discussed previously, with the general assumption of material failure that occurs only along the pre-defined tearing line in the contact tiebreak approach, this predicted material failure response will likely to differ from the actual scenario.

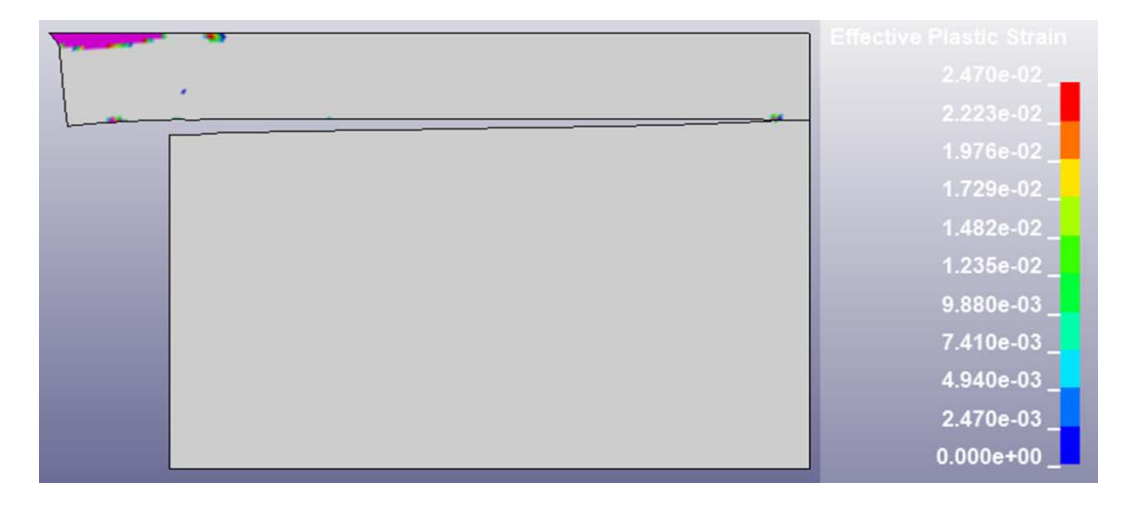


Figure 5-76: Location of tensile strain failure in soft-catcher for impact velocity of 50 m/s (at time t = 0.0199 s)

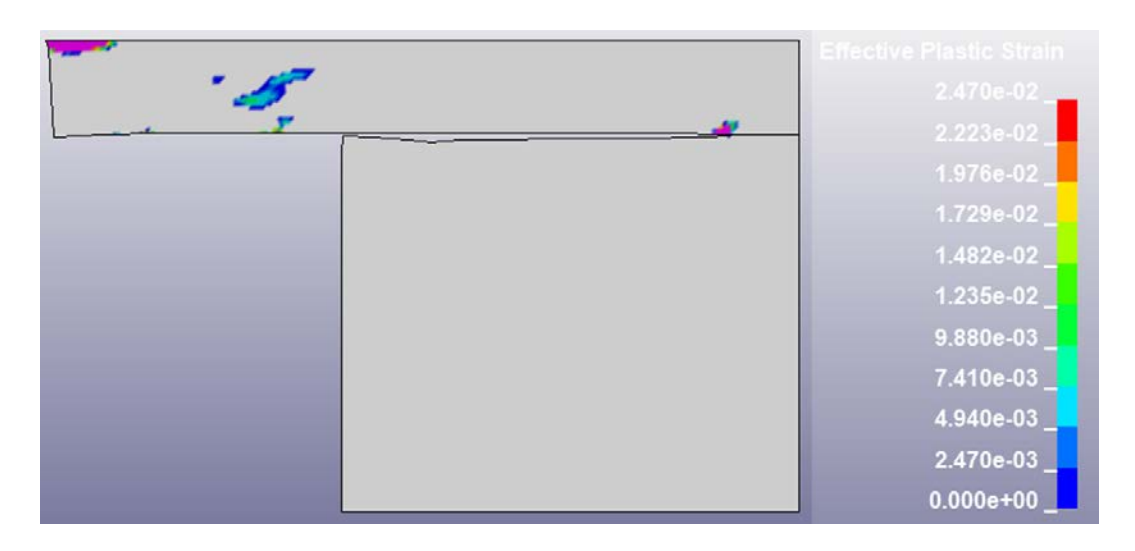


Figure 5-77: Location of tensile strain failure in soft-catcher for impact velocity of 100 m/s (at time t = 0.022 s)

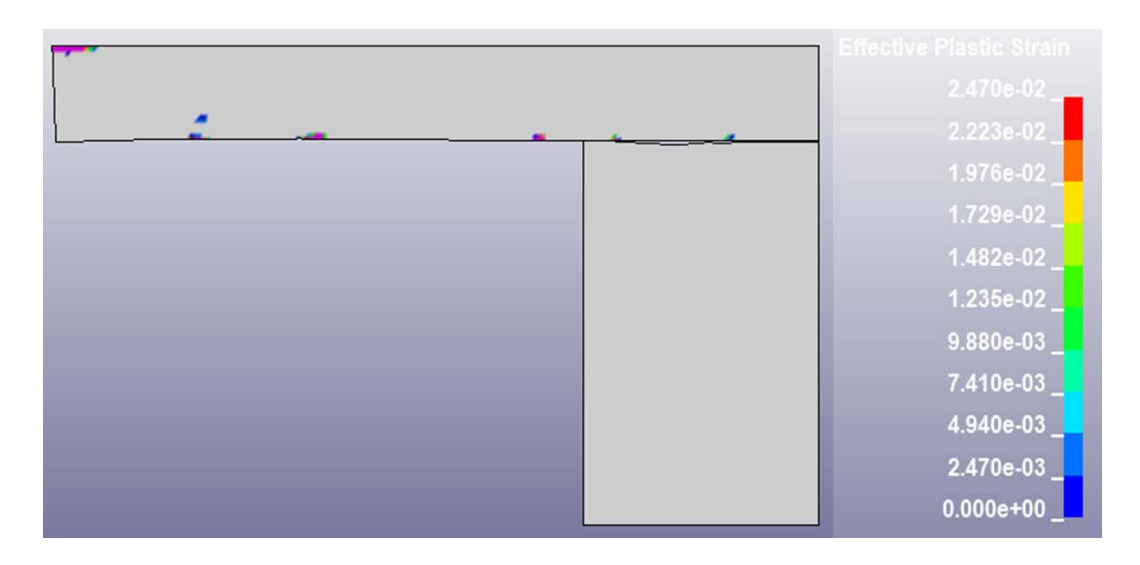


Figure 5-78: Location of tensile strain failure in soft-catcher for impact velocity of 145 m/s (at time t = 0.0211 s)

On the other hand, Figure 5-79, Figure 5-80 and Figure 5-81 illustrate the part of soft-catcher in which the effective plastic strains go below -0.0349, which implies that the material strain exceeds compressive elastic limit. This effective plastic strain value of -0.0349 corresponds to the volumetric strain of 0.0343 (i.e. observed elastic yield strain in numerical model). Obviously, higher compressive strain value can be noted for the models subjected to higher impact velocities.

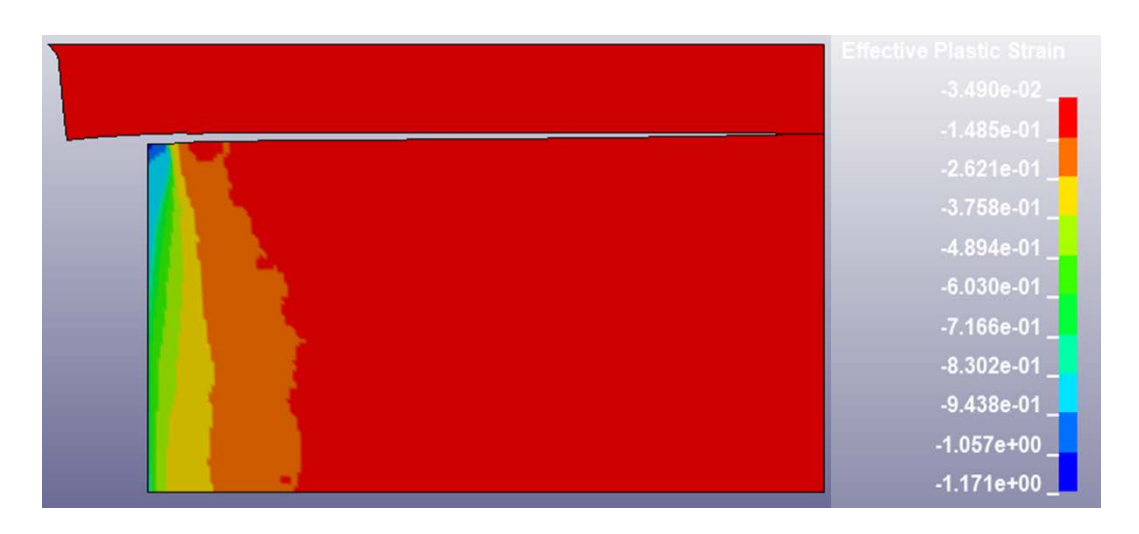


Figure 5-79: Contour plot of compressive strains in soft-catcher for impact velocity of 50 m/s (at time t = 0.0199 s)

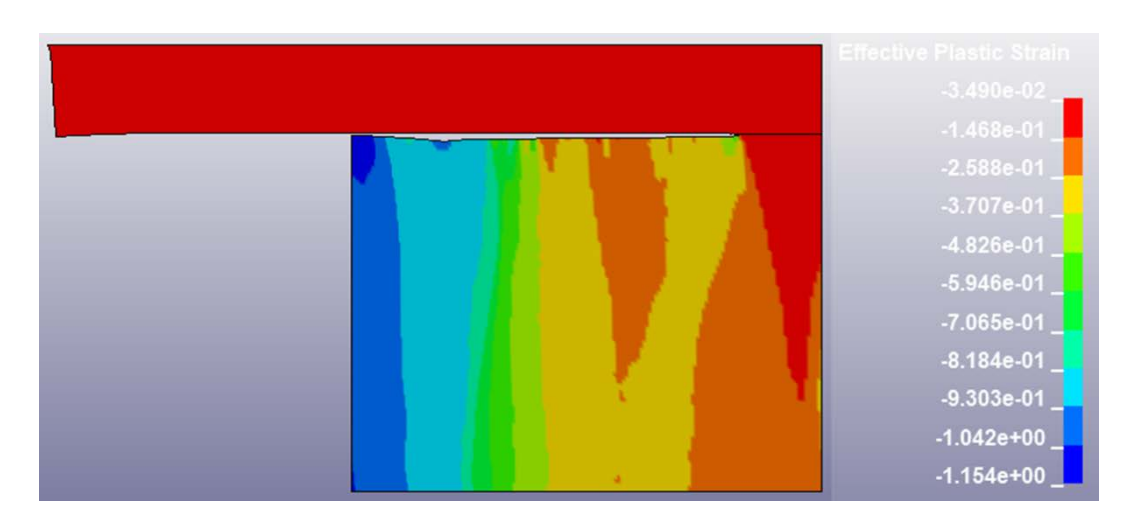


Figure 5-80: Contour plot of compressive strains in soft-catcher for impact velocity of 100 m/s (at time $t=0.022~\mathrm{s}$)

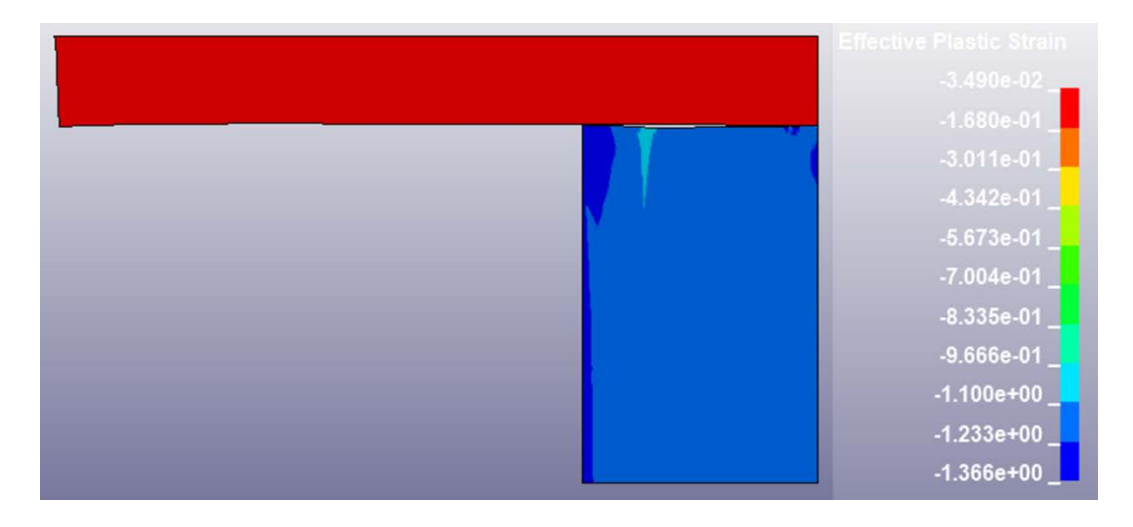


Figure 5-81: Contour plot of compressive strains in soft-catcher for impact velocity of 145 m/s (at time t = 0.0211 s)

5.5.1.5 Support Reactions at Boundaries

The earlier discussions on the 1D numerical model (i.e. with 2 m target length) have highlighted the significance of elastic stress wave on developing reaction forces at the end boundary of soft-catcher. In this section, similar plots of total reaction forces at respective boundary ends, as well as the distribution of maximum forces along the supports will be presented.

Figure 5-82 depicts the total resultant support force-time histories of the lateral restraint (see Boundary Set 3 in Figure 5-64), for models with various impact velocities. Except in the Y-direction, noticeable reaction forces are built-up in both negative-X and positive-Z direction. The reaction forces in the negative-X direction indicate resistance against motion of wall debris. It is interestingly noted that for model with lower impact velocities, the initial peak total reaction forces in negative-X direction is found to be higher. This implies that the models with lower impact velocities are affected in greater extent, by the presence of lateral boundary restraint. As time increases, it is expected that these reaction forces in negative-X direction will decrease with the deceleration of wall debris.

The total reaction forces acting in the positive-Z direction signify that the foam materials near the lateral support restraint are subjected to tensile stresses during the impact duration. Similarly, higher reaction forces are observed for models with lower impact velocities. These observations appear to be consistent with the development of principal tensile stresses within the overlying region. With the opening along the tearing interface, the nodes within the overlying region of the soft-catcher are able to displace vertically and hence, these reaction forces in positive-Z direction are gradually reduce to close zero as time increases. However, one shall note that these build-ups of positive-Z reaction forces may not be realistic to consider, as the bonding between the soft-catcher and the lateral containment wall is close to zero.

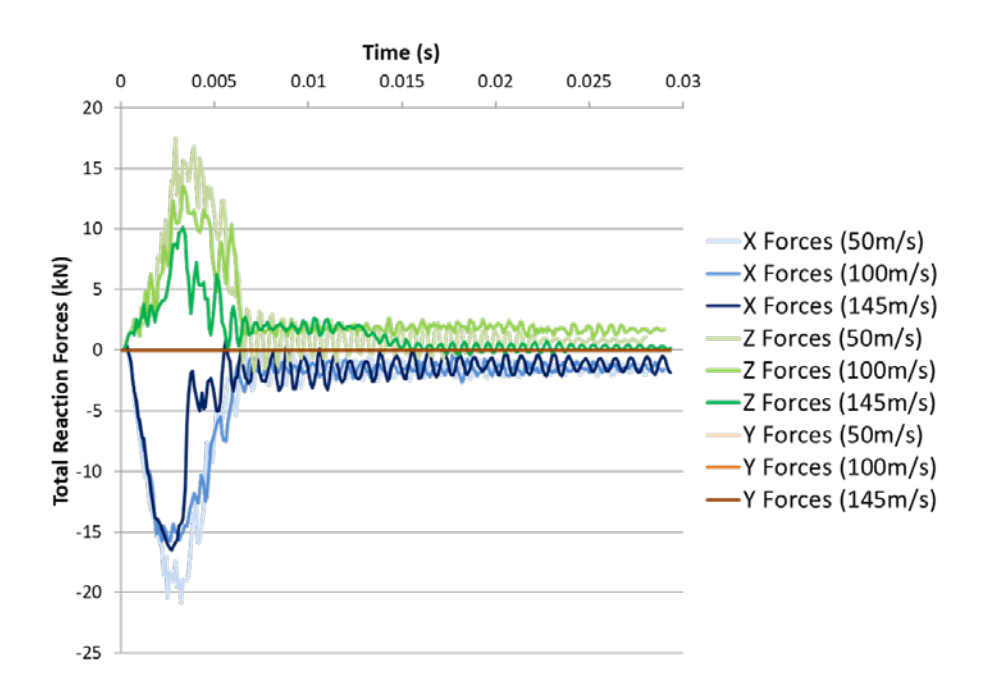


Figure 5-82: Total resultant reaction force-time histories plots for lateral support restraint

Figure 5-83 presents the distribution of maximum reaction forces in X and Z-direction that occur along the length of the lateral boundary restraint for models with various impact velocities. Higher magnitude of maximum reaction forces in the negative-X direction can be observed in models with lower impact velocities, which is in good agreement with the observation in Figure 5-82.

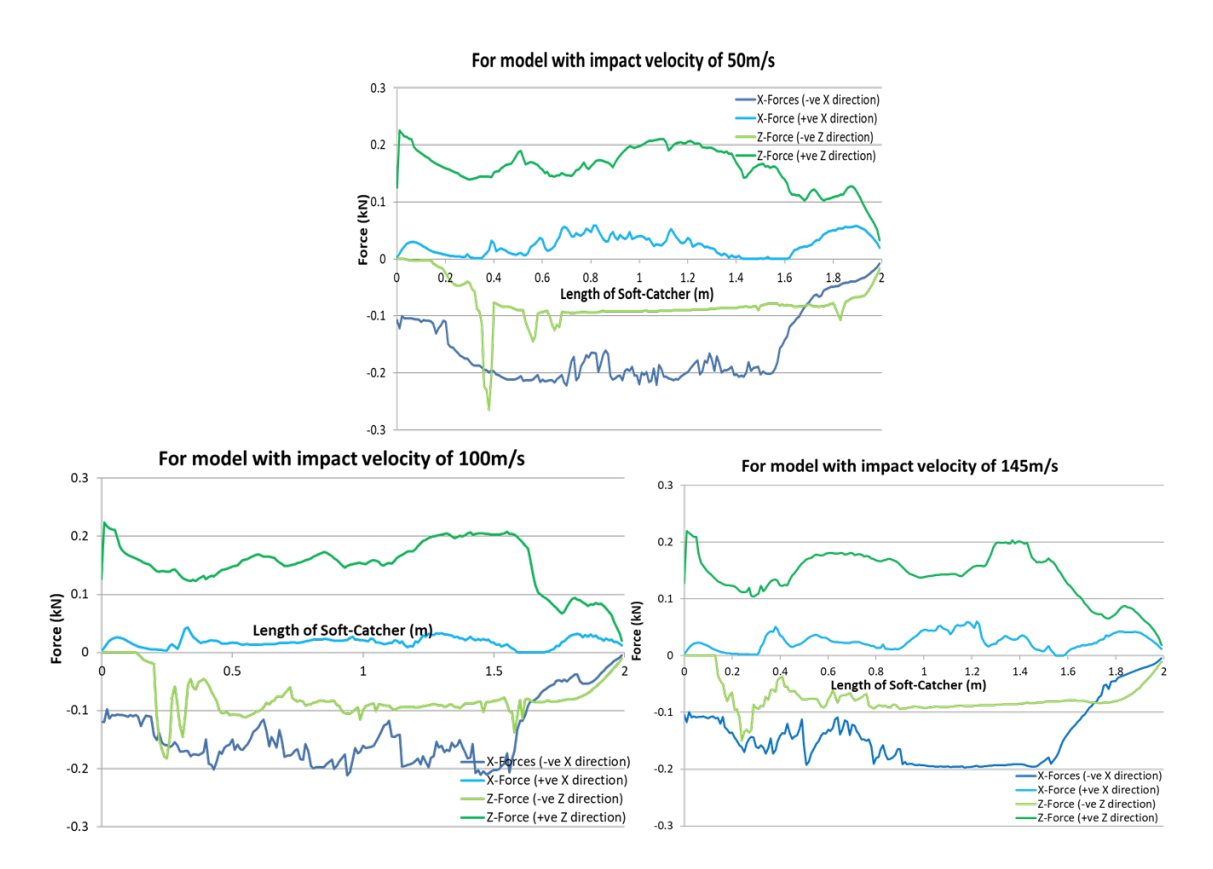


Figure 5-83: Distribution of maximum reaction forces (X and Z-direction) induced along the lateral support restraint for models with different impact velocities

Similarly, Figure 5-84 depicts the total resultant support force-time histories of the end boundary restraint (see Boundary Set 4 in Figure 5-64) in X and Z-direction, for models with various impact velocities. As mentioned in the results discussion for 1D numerical model (i.e. 2mTL model), the onsets of end support reaction forces in negative-X direction occur at the time that corresponds to the elastic stress wave reaching the end of soft-catcher (i.e. approximately 0.0023s for a linear sound speed of stress wave, 866.025m/s to travel a distance of 2m). However, it appears that the initial peak total reaction forces (i.e. due to incidental elastic wave) in the 2D model are found to be lower than the 2mTL model. For the model with impact velocity of 145m/s, higher total reaction forces of approximately 40kN are observed at a later time. This is attributed by the plastic shock wave impacting against the end support. The total resultant forces in Y direction are negligible.

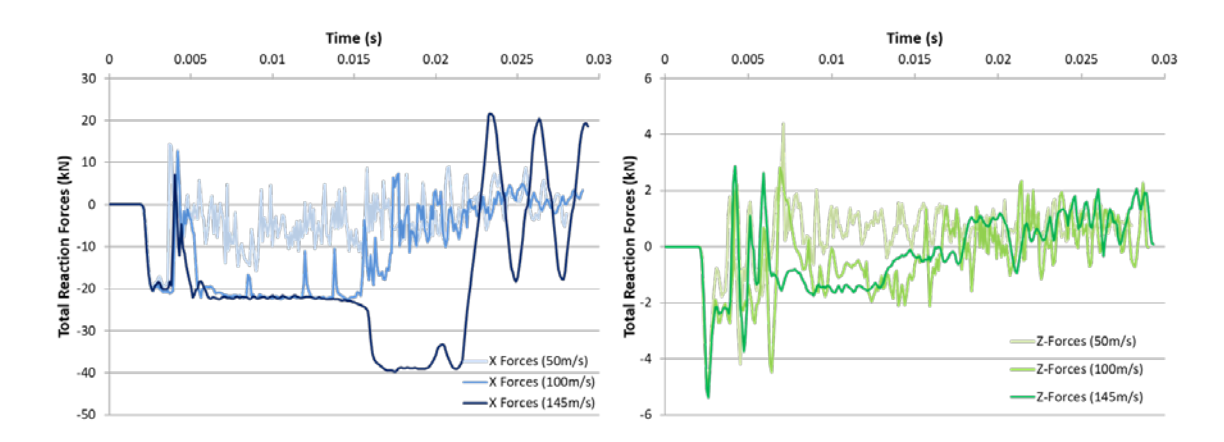


Figure 5-84: Total resultant reaction force-time histories plots for end support restraint

Figure 5-85 presents the distribution of maximum reaction forces that occur along the height of the soft-catcher for models with various impact velocities.

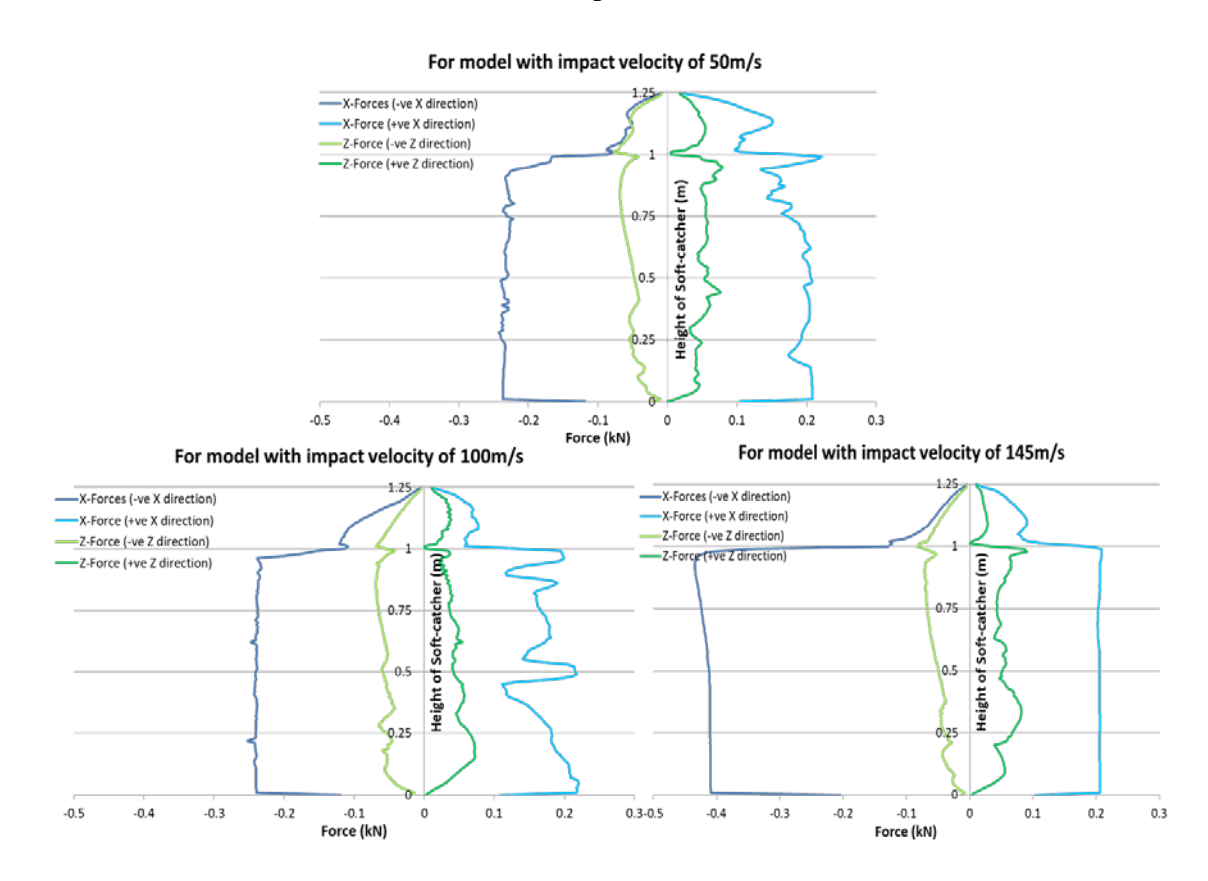


Figure 5-85: Distribution of maximum reaction forces (X and Z-direction) induced along the end support restraint for models with different impact velocities

5.5.2 Sensitivity Study of Shear and Tensile Failure Stress

The previous sections have extensively discussed the responses of soft-catcher under combined shear and tensile failure mode. It is therefore of particular interest to investigate the sensitivity of increasing the shear and tensile resistance over certain output parameters. In this section, a series of numerical analyses are executed by either increasing the shear failure

stress and keep the tensile failure stress at base value, or vice versa. The base values for shear and tensile failure stress are 1.86 MPa and 2.17 MPa respectively. The 2D Model with impact velocity of 100 m/s is considered.

Penetration Distance of Wall Debris

Figure 5-86 presents the influence of increasing shear and tensile failure stresses over the final debris penetration distances. It clearly shows that shear resistance plays a significant role over decelerating the debris motion, as compared to tensile failure stress.

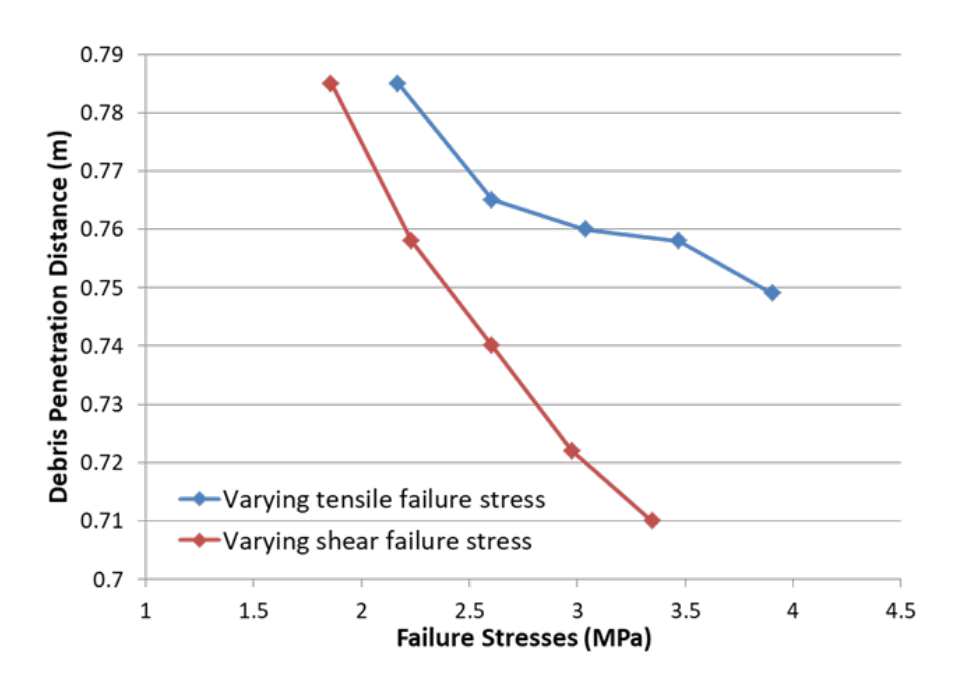


Figure 5-86: Debris penetration distance of 2D Model, under the influence of increasing shear and tensile failure stresses

To understand better on why shear failure stress influence more than the tensile failure stress on the debris penetration distance, it is good to evaluate the interface shear and normal (tensile) stresses induced over the tearing line. Figure 5-87 shows that the increases in shear failure stress resulted corresponding increases in maximum shear stresses induced over the length of tearing interface. SFS_1.8 indicates model with shear failure stress of 1.8 times the base value of 1.86 MPa, while NFS_1.8 indicates model with tensile failure stress of 1.8 times the base value of 2.17 MPa. On the other hand, the increases in tensile failure stress do not affect the magnitude of maximum shear stresses. This observation seems to contradict with the plot in Figure 5-86 that shows decreases in penetration distances over the increases in tensile failure stress. Nevertheless, it is subsequently discovered that by increasing the tensile failure stresses, more energies are dissipated over the shear stresses induced along the tearing interface. Figure 5-88 illustrates the interface shear stress-time history plots for selected segments along the tearing line.

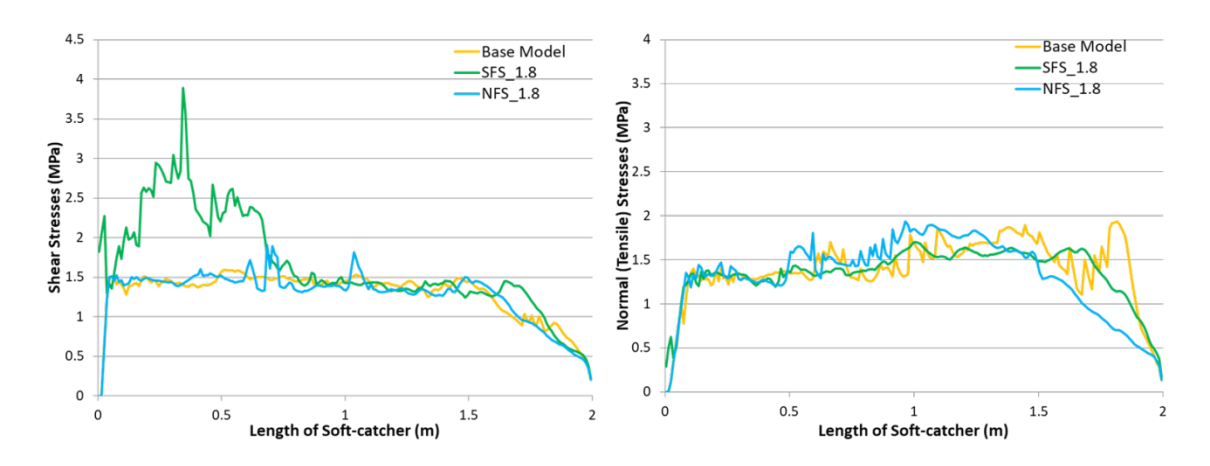


Figure 5-87: Maximum interface shear and normal (tensile) stresses induced in 2D Model, over the length of soft-catcher

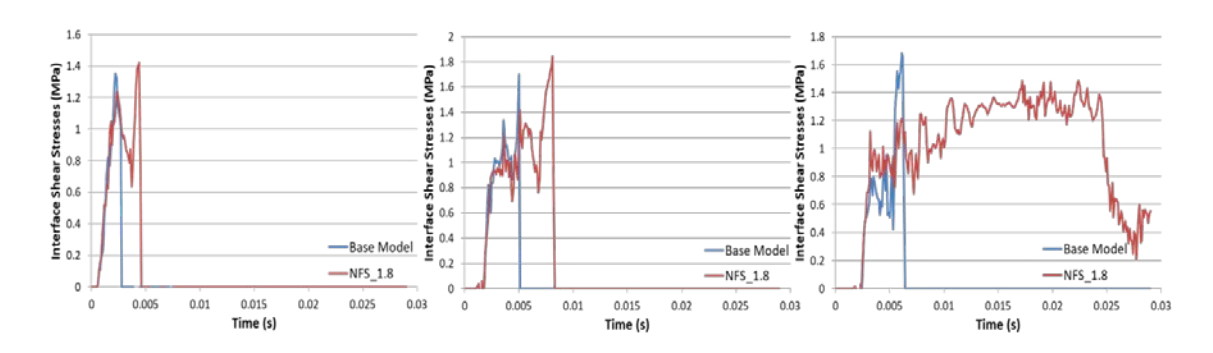


Figure 5-88: Shear stress-time history plots of selected segment over the tearing interface

Maximum Stresses on Wall Debris

The "first" peak compressive stresses of Element A in the 2D Model, with increasing shear or tensile failure stresses are plotted in Figure 5-89. As expected, the increases in shear resistance will also result a corresponding increase in compressive stresses of Element A. Conversely, increases in tensile failure stress have no effects over the compressive stresses of Element A.

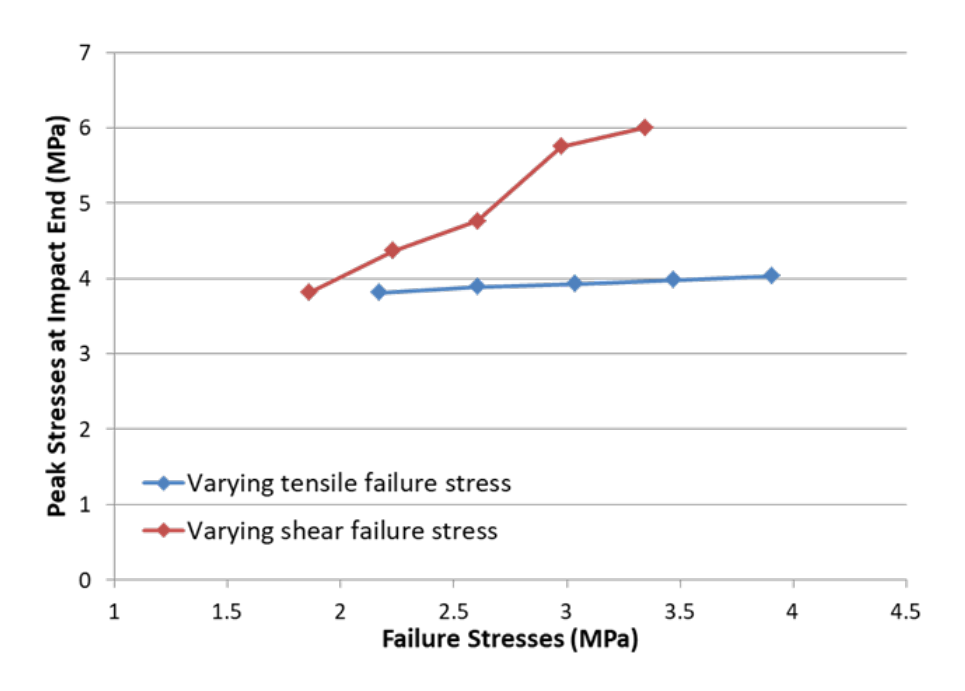


Figure 5-89: Peak compressive stresses of Element A in 2D Model, under the influence of increasing shear and tensile failure stresses

Support Reaction

Figure 5-90 illustrates the peak total reaction forces at respective boundary supports, under the influence of increasing shear and tensile failure stresses. Apparently, the increases of either tensile or shear failure stresses indicate marginal influence over the development of peak total reaction forces at both lateral and end boundary support. This is mainly due to the fact that the magnitudes of reaction forces at boundary end primarily depend on the elastic yielding stress of the soft-catcher material.

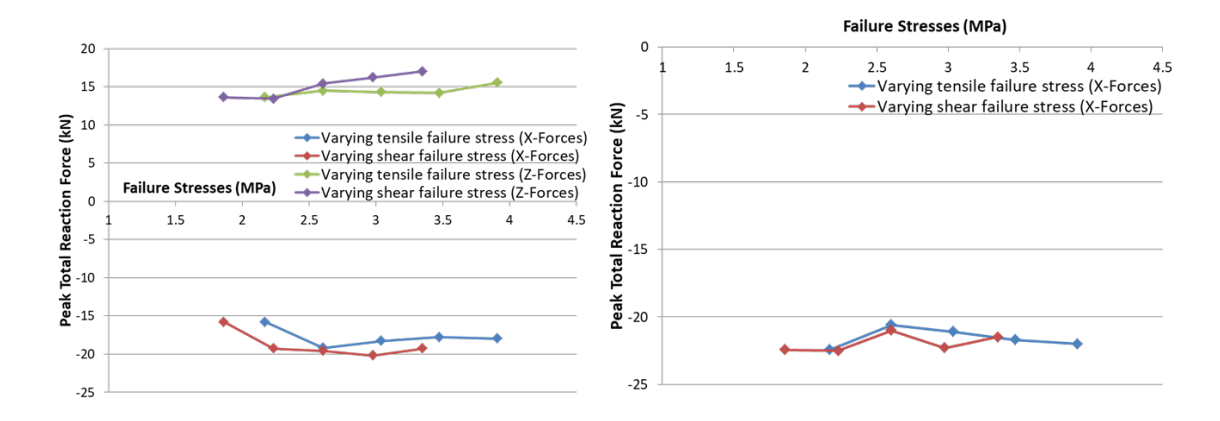


Figure 5-90: Peak total reaction forces at boundary supports, under the influence of increasing tensile and shear failure stresses

5.5.3 Concluding Remarks

The inclusion of tearing resistances within the soft-catcher in the 2D models has evidently displayed some deviations in predictions over soft-catcher's responses, as compared to 1D

model. The 2D models have shown decreases in debris decelerations, particularly in the later phase of the impact duration, which are more significant in scenarios with impact velocities of 50 m/s and 100 m/s. Both these scenarios predict longer debris penetration distances. These decreases in debris decelerations are mainly attributed by the reduction in momentum transfer due to drastic stress oscillations in the 2D models. These stress oscillations are found to associate with the losses of contact between the debris and frontal face of soft-catcher, during the penetration process.

The impact stresses acting on the debris are evaluated by examining the compressive stresstime histories of soft-catcher at its impact end. The highest impact stresses usually occur at the first instance of debris impact. Higher stresses are built-up along the frontal face of softcatcher, in particular, near the tearing interface. These high stresses are in 2D model are induced due to the presence of shear and tensile resistance along the tearing interface. It is apparent that 1D models under-predicts these impact stresses acting on the debris.

Interestingly, it is found that models with lower impact velocities have induced slightly higher reaction forces in the negative-X and negative-Z direction along the lateral support restraint. These observations seem reasonable; considering that the extent of material failure along the tearing interface will be lesser in models with lower impact velocities, which implies that more stresses can be transferred into the overlying region of soft-catcher. Tensile stresses in the soft-catcher region above the tearing line has also resulted reaction forces acting in the positive-Z direction.

With the presence of lateral support restraint in the 2D models, slight reductions in peak total reaction forces (negative-X direction) for the end support restraint can be seen for models with impact velocities of 50m/s and 100m/s. However, for the model with impact velocity of 145m/s, higher peak reaction forces due to plastic shock wave are more or less close to the one obtained in the 1D numerical (2mTL) model.

Sensitivity study of shear and tensile failure stress

Increasing the shear resistance along the tearing interface has a more apparent influence over the debris penetration distance and the peak compressive stresses of soft-catcher at its impact end. However, the increases of either tensile or shear failure stresses indicate relatively less influences over the development of peak total reaction forces at both lateral and end boundary support.

5.6 Design Consideration for Soft-catcher

So far, only three debris launch velocities have been considered in the evaluation of the soft-catcher responses; 50 m/s, 100 m/s and 145 m/s. In view of facilitating ease of soft-catcher design with more data points, additional models are run to create design charts. These other debris launch velocities include 25 m/s, 75 m/s and 125 m/s. Figure 5-91 presents the predictions of debris penetration distances in various models, over the range of debris launch velocities.

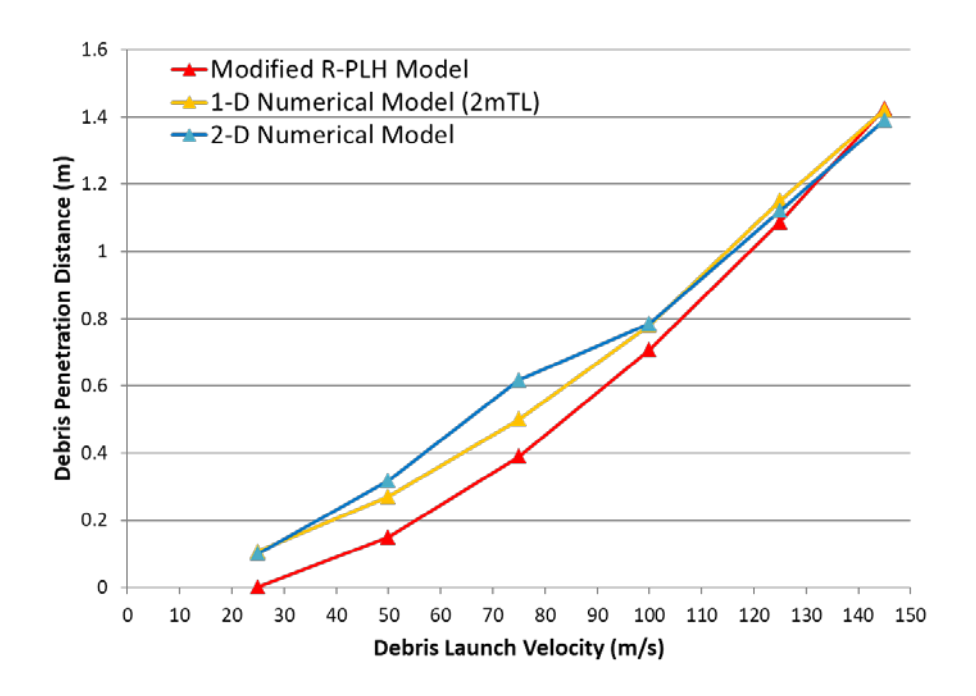


Figure 5-91: Debris penetration distance (m) over a range of debris launch velocities

It is observed that Modified R-PLH Model predicts shorter debris penetration distances as compared to the numerical predictions. This is due to the simplified approach by assuming an abrupt termination of the constant initial particle velocity when the shock wave terminates. However, the debris penetration distances predicted by Modified-R-PLH Model and the rest of the 1D and 2D numerical models are relatively close, when debris launch velocity reaches near 145 m/s. One usually expects that the 1D numerical model will give conservative prediction of the debris penetration distance, considering that the only failure mechanism to dissipate kinetic energies is through 1D crushing of material. However, it is found that the 2D Models predict longer debris penetration distances, especially for models with impact velocities of 50 m/s, 75 m/s and 100 m/s. This phenomenon can be possibly explained by the reduction of momentum transfers from the debris motion, due to drastic compressive stress oscillations experienced by the elements within the 2D models (See Section 5.5.1.3).

The left plot of Figure 5-92 shows that both Modified-R-PLH Model and 1D numerical models do not account for the increases in impact stresses on debris, arising from the material's failure resistances along the tearing interface. As such, the 2D Model predicts a higher impact stresses, especially near the tearing interface along the front face of soft-catcher. However, the differences in predicting these impact stresses on debris reduces when comparing with the average compressive stresses over the frontal face of soft-catcher in the 2D models (See the right plot of Figure 5-92). As 2D Model realistically accounts for both tensile and shear failure stresses, and that these highest impact stresses occurs at first instance of impact, it is preferable to consider the 2D Model's predictions (in right plot of Figure 5-92) as the governing design parameters.

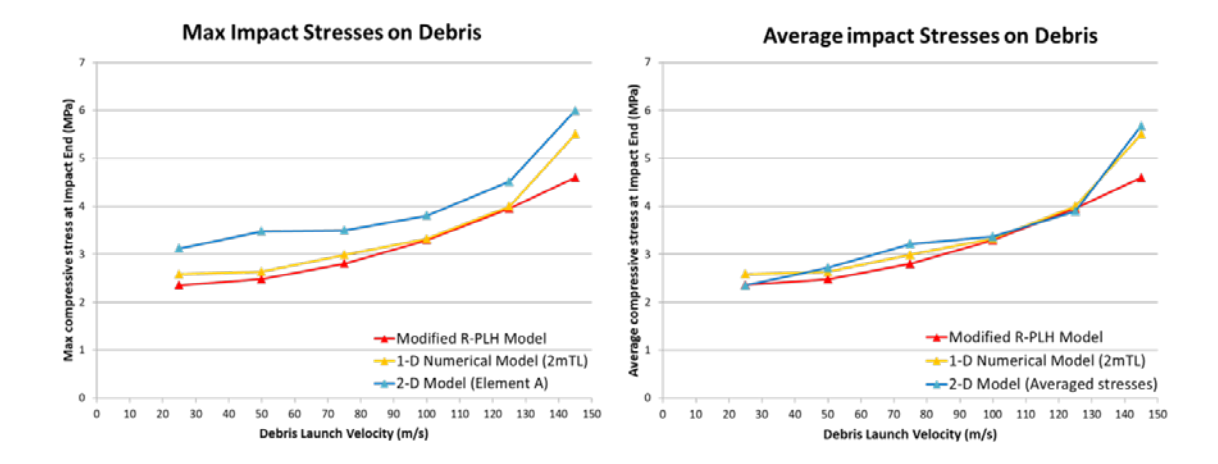


Figure 5-92: Predictions of maximum impact stresses (left plot) and average impact stresses (right plot) on debris over a range of launch velocities

In view of not inducing additional damage to concrete debris during the soft-catching process, it is vital to ensure that the impact stresses acting on the debris must not exceed the residual strength of concrete debris. In 2013, NTU conducted experimental investigation to quantify damage levels of chamfered concrete specimens, with cube size of 100 mm, in accordance to crack-surface to volume ratio. In which, three different damage levels are defined using three concrete cube specimens;

- 100% of peak load
- 86.5% of peak load in post-peak regime
- 73.1% of peak load in post-peak regime

With the design concrete strength of 35 MPa, the respective residual concrete strengths for different damage levels are identified in Figure 5-93. The lowest ultimate strength (i.e. loading stress when concrete disintegrate) was found to be approximately 15 MPa, according to the NTU test specimens. Based on the 2D model prediction with highest debris launch velocity of 145 m/s, the maximum impact stress reaches 6.0 MPa, which is much lower than the damage levels and the lowest ultimate loading stresses of these concrete specimens.

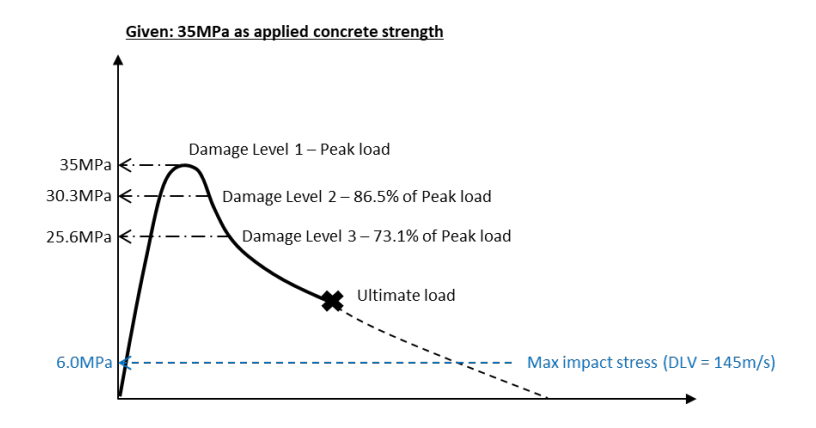


Figure 5-93: Maximum impact stresses for 2-D model with DLV of 145 m/s, in comparison with residual concrete strengths for damage level 1, 2 and 3 for an applied concrete strength of 35 MPa

Figure 5-94 presents the total reaction forces at lateral and end boundary supports. It can be observed that as the impact velocities increases, lower peak total reaction forces are induced along the lateral boundary support. This can be associated to the increasing extent of material failure along the tearing interface as the impact velocities increase. At the end boundary support, it appears that 1D numerical model generally provides conservative predictions on the total reaction forces as compared to the 2D model.

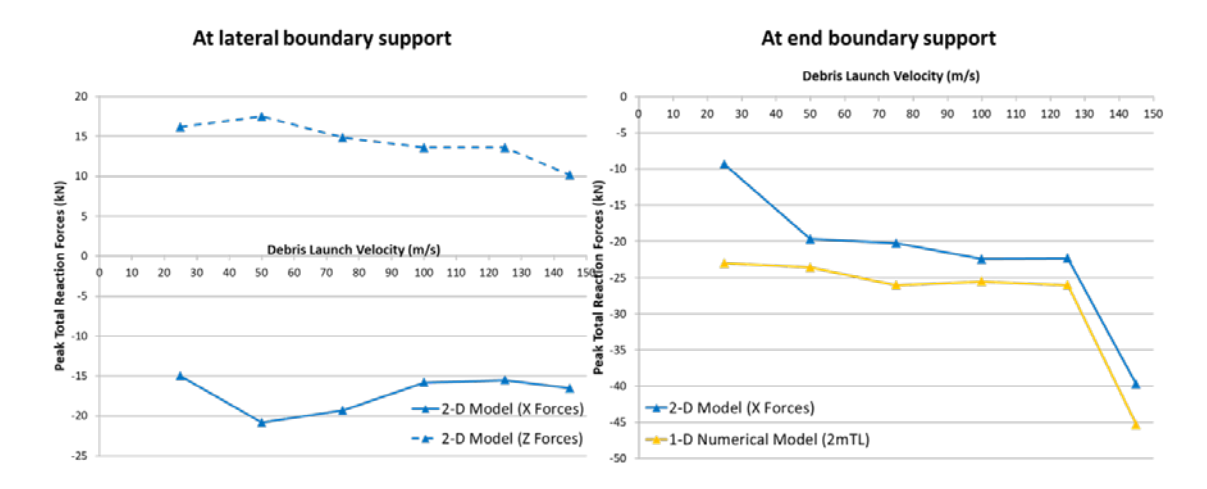


Figure 5-94: Predictions of total reaction forces at lateral boundary support (left plot) and at end boundary support (right plot) over a range of launch velocities

6 Conclusion and Recommendation

A feasibility study of using elasto-plastic foam material to soft-catch explosively-damaged concrete debris was performed in this Master thesis work. This forms part of the overall effort to obtain debris data arising from an internal explosion of a KASUN structure. The focus of this thesis report is to study in details, the interactions between concrete debris and soft-catcher; and identify key parameters for future detailed design of soft-catcher. Considering the needs to ensure no additional damages to debris during penetration, and to effectively decelerate and stop the debris within a short distance (i.e. 2 m), the rigid polymethacrylimide foam, known as Rohacell 110WF, is chosen as the benchmark material for the soft-catcher.

Several simple shock wave models that follow Rankine-Hugoniot's theory to predict responses of cellular material upon one-dimensional impact are briefly introduced. Recognising the ability to incorporate time-dependent variables (e.g. strains, velocity jumps) into formulating the shock wave responses, the rigid-power law hardening (R-PLH) model is chosen as the base model for analytical prediction. Following then, modifications to existing R-PLH model are proposed to include the effect of nose shape geometry of debris and frictional resistance. Furthermore, changes to material states pertaining to incidental elastic stress wave propagation are incorporated in the modifications as well. The analytical predictions are performed using both R-PLH Model and Modified R-PLH Model, following which the preliminary design of soft-catcher is established using the Modified R-PLH Model. An impact scenario of the large wall debris is evaluated with three different initial debris launch velocities; 50 m/s, 100 m/s and 145 m/s. It is evaluated that the Modified R-PLH Model exhibits reductions in shock-induced stresses and strains, as compared to R-PLH Model. Consequently, the Modified R-PLH Model predicts slower deceleration of debris motion. In predicting the overall debris penetration distances, the Modified R-PLH Model makes two assumptions on how the particle velocity induced by the elastic stress waves terminates when debris velocity reaches elastic velocity. However, the assumption of constant particle velocity during the penetration time is subsequently validated to be more appropriate by numerical analyses. Moving on, it is necessary to emphasize that these analytical model predictions consider 1D shock wave propagation and assume infinite thickness of cellular materials. Also, the reflections and interactions of stress waves are not accounted for.

Numerical modelling and simulations using LS-DYNA are then carried out to verify various assumptions made in the analytical models. Firstly, simple numerical cell tests are performed to establish the responses of selected material model (MAT_63 CRUSHABLE FORM) under tensile and compressive loadings. To verify 1D analytical model's assumptions, numerical models are initially set up with 20m target length (20mTL), in order to minimise end boundary effects. Mesh sensitivity studies are concurrently performed with various element sizes. It is discovered that the approach to assume constant particle velocity induced by the elastic waves appears to give a more consistent results with the numerical outputs, by evaluating the velocity-time curves. It is further established that this consistency of debris velocity is due to close predictions of shock-induced stresses. However, it remains invalid for analytical model to assume constant shock stresses across spatial domain within the crushed region (i.e. behind shock wave front). The numerical analyses have shown that as time increases, lower shock stresses are induced at the impact end, as compared to those directly behind the wave front. Nevertheless, this resulted marginal differences between the analytical and numerical model, in predicting deceleration of debris motion.

It is crucial to emphasize that the consistencies between the Modified R-PLH Model and the 20mTL numerical model are mainly observed in the higher velocity time response regime (i.e. debris velocity ranging from initial impact velocity to near elastic velocity). This is also equivalent to the duration of penetration whereby the debris deceleration mechanism is largely dominated by the plastic shock wave propagation. In the lower response regime (i.e. debris velocity lower than the elastic velocity) when significant change in velocity rate is observed, it is determined that only elastic waves are in existence. Horizontal plateaus can be identified within this lower velocity time response regime. These plateaus occur when the debris moves at the same velocity as the foam material ahead, and that no crushing of foam material is taking place. In this lower response regime, debris deceleration is governed by the elastic wave propagation. Hence, the final debris penetration distance will increase as the length of target increases. Taking this finding into consideration, it will be inappropriate to use the 20mTL numerical model, when the actual length of soft-catcher is limited to 2m.

With the element size selected to be 0.010m, the impactor-target numerical model with 2m target length (2mTL) is constructed. In this model, the effects of end boundary condition are examined. The presence of end boundary condition at close proximity to the impact front of soft-catcher may influence the plastic wave propagation, especially when higher impact velocities are involved. Slight increases of the initial peak stresses of Element 1 are observed for the 2mTL model, in comparison with the 20mTL model. Though, the use of this initial peak stress as the design parameter to check against the residual strength of debris remains valid. Further mesh sensitivity studies involving smaller element sizes (e.g. 0.005m, 0.0025m and 0.001m) have shown that convergence of numerical results can be achieved with element sizes of 0.010m or smaller.

Having to verify 1D analytical model and study the effects of boundary end condition due to the soft-catcher's length of 2m, the focus is now shifted to explore the effects of soft-catcher's tearing resistance to influence the overall interactions between the debris and soft-catcher. The 2D numerical model is set-up to include an overlying region above the impact zone within the soft-catcher. Instead of using sophisticated element erosion techniques, a simplified method to simulate the lateral resistance via contact tiebreak option in LS-DYNA is adopted. A contact interface (i.e. pre-defined tearing line) specified with stress-based failure criterion is modelled along the debris penetration path (upper edge of the impact zone) within the softcatcher. Decreases in debris deceleration are observed in the 2D models during the late phase of the impact duration, in particular for models with lower impact velocities (i.e. 50 m/s and 100 m/s), as compared to both 1D analytical and numerical models. This phenomenon is resulted from the losses of contact between debris and the frontal face of soft-catcher. Localised increases in compressive stresses of soft-catcher can be observed at the tearing interface between the frontal edge of the soft-catcher and the wall debris. This thus implies that both 1D analytical and numerical model under-predicts the stress resistances acting on the debris. Reaction forces induced over the lateral and end boundary supports are also evaluated. Along the lateral boundary support, higher reaction forces (in particular, negative-X and positive-Z direction) are observed in 2D models with lower impact velocities. Conversely, at the end boundary support, higher total reaction forces (in negative-X direction) due to plastic shock wave are obtained in model with impact velocity of 145m/s.

From the sensitivity study of tensile and shear failure stresses over the soft-catcher's responses (i.e. penetration depth, impact stresses on debris, support reaction forces), it is

concluded that shear resistance plays an influential role over debris penetration distance and the peak compressive stresses induced over the impact end of soft-catcher.

Table 6-1 consolidates and compares predictions on debris penetration and impact resistances from 2D numerical models and both 1D numerical and analytical models. Design charts are also created to provide correlations of the various soft-catcher design parameters, with a range of debris launch velocities.

Outputs	Modified R- PLH Model	1D Model (2mTL)	2D Model
Impact Velocity of 50m/s			
Maximum stress on debris (MPa)	2.484	2.637	3.480
Debris penetration distance (m)	0.149	0.270	0.318
Impact Velocity of 100m/s			
Maximum stress on debris (MPa)	3.299	3.326	3.810
Debris penetration distance (m)	0.707	0.780	0.785
Impact Velocity of 145m/s			
Maximum stress on debris (MPa)	4.600	5.504	6.000
Debris penetration distance (m)	1.425	1.420	1.390

Table 6-1: Comparison of analytical and numerical (1D and 2D) model predictions of softcatcher design parameters

Moving forward, some possible research areas can be identified to follow up with this thesis work, with an aim to improve overall prediction capabilities:

The analytical predictions of debris motion using Modified R-PLH Model can be further improved, particularly in the lower velocity time response regime (i.e. debris velocity lower than the elastic velocity). The current approach assumes instantaneous drop of absolute debris velocity to zero once the relative velocity of debris (i.e. with reference to the particle elastic velocity induced by the precursor elastic waves) reaches zero. This assumption may not be valid, with the observations made in the numerical models. A more practical approach can be adopted by assuming linear decrease of debris velocity within the lower velocity time response regime. The rate of velocity decrease can follow the velocity gradient observed in the higher velocity time response regime.

Considering single large wall-sized debris, the frictional resistance between the debris and the soft-catcher is assumed to be insignificant in this current thesis work. However, future work

can include relevant frictional coefficients, especially when the specific surface area of debris increases.

The current approach of pre-defining a tearing line to simulate the failure response of soft-catcher will not be realistic. Having investigated the tensile stress development within the 2D model and examined possible locations of tensile strain failure, it is very likely that tearing failure of soft-catcher can occur within the overlying layer above the pre-defined tearing line. With the occurrences of these tensile failures, the overall interaction between the debris and soft-catcher can be affected. In this respect, it is believed that the 2D numerical models considered in this thesis work may be conservative in predicting the overall debris penetration distance. This is mainly due to the fact that if failure criterions are incorporated for elements within the overlying layer, much more energies from the debris motion will be released by material failure, in which can result in further deceleration of debris motion. With this in mind, effect of different thicknesses of the overlying layer on the failure phenomenon can also be evaluated. Therefore, the use of continuum-based approach (i.e. element erosion technique) can be a better option to consider.

Based on the ballistic phenomenon of debris moving at same initial launch velocity upon breakup due to explosion, the current thesis simplifies the consideration by assuming single large debris with size of the concrete wall. As a result, the shape coefficients defined in the Modified R-PLH Model are 1.0. However, different shape coefficients, depending on the probable sizes of individual wall debris, can be evaluated to better represent a more realistic scenario. This is especially the case when debris cloud expands further. The 1-D analytical models can be used to study the impact of individual debris with lower specific mass (i.e. thickness less than 0.15 m) and reduced shape coefficients of less than 1.0. Numerical simulation can be performed to further validate the current Modified R-PLH Model, on the aspects of these shape coefficients. The numerical analyses can account for effects under multiple debris hits scenario, under spatial and time domain.

Even though the internal blast loading can be attenuated through adequate venting and breakup of concrete structures, numerical simulation can be carried out to account for the residual blast loading onto the soft-catcher, which will improve the prediction accuracy of the debris penetration phenomena. Depending on the time of arrival for the shock wave to reach the soft-catcher, the blast pressure loading can be applied onto the frontal face of the soft-catcher to consider the combined effects of blast and debris impact. With the additional surface loading, the foam material will be further densified, which can lead to higher initial impact stresses onto the debris and affect the overall debris penetration distance. Higher reaction forces can be expected to induce at the end support boundary.

Lastly, effects of other mechanical properties of soft-catcher (i.e. elastic modulus, yielding stress, initial density of foam etc.) on the overall material responses can be investigated. This can eventually work towards delivering a more economical and effective solution for design consideration.

Bibliography

- [1] M. Van der Voort, "Recent Developments of the KG software," in *34th DoD Explosives Safety Seminar DDESB*, Portland, Oregon, 2010.
- [2] K. Kang, Y. Koh and H. Lim, "Modelling the Debris Throw from a Reinforced Concrete Ammunition Storage Magazine," *DSTA Horizon 2013*, 2013.
- [3] H. Lim, "Response of reinforced concrete slab to explosive," MSc thesis Delft University of Technology, 2005.
- [4] L. J. Gibson and M. F. Ashby, Cellular solids structure and properties, 2nd Ed, Cambridge: Cambridge University Press, 1997.
- [5] S. Reid and C. Peng, "Dynamic Unaxial Crushing of Wood," *Int. J. Impact. Engrg Vol.* 19 Nos. 5-6, pp. 531-570, 1997.
- [6] P. Tan, S. Reid, J. Harrigan, Z. Zou and S. Li, "Dynamic compressive strength properties of aluminium foams. Part I Experimental data and observations," *Journal of the Mechanics and Physics of Solids 53*, pp. 2174-2205, 2005.
- [7] P. Tan, S. Reid and J. Harrigan, "On the Dynamic Mechanical Properties of Open-cell Metal Foams A re-assessment of the "simple-shock theory"," *Int. J. of Solids and Structures*, pp. 2744-2753, 2012.
- [8] S. Lopatnikov, B. A. Gama, M. J. Haque, C. Krauthauser and J. W. Gillespie Jr, "High-velocity plate impact of metal foams," *Int. J. of Impact Engrg Vol. 30*, pp. 421-445, 2004.
- [9] S. L. Lopatnikov, B. A. Gama, M. Jahirul Haque, C. Krauthauser, J. W. Gillespie Jr, M. Guden and I. W. Hall, "Dynamics of metal foam deformation during Taylor cylinder-Hopkinson bar impact experiment," *Composite Structures*, vol. 61, pp. 61-71, 2003.
- [10] Z. Zheng, Y. Liu, J. Yu and S. Reid, "Dynamic crushing of cellular materials: Continuum-based wave models for the transitional and shock modes," *Int. J. of Impact Engrg*, vol. 42, pp. 66-79, 2012.
- [11] S. Pattofatto, I. Elnasri, H. Zhao, H. Tsitsiris, F. Hild and Y. Girard, "Shock enhancement of cellular structures under impact loading: Part II analysis," *Journal of the Mechanics and Physics of Solids*, vol. 55, pp. 2672-2686, 2007.
- [12] J. Harrigan, S. Reid and A. Seyed Yaghoubi, "The correct analysis of shocks in cellular material," *Int. J. of Impact Engrg*, vol. 37, pp. 918-927, 2010.
- [13] Z. Zheng, Z. Yu, C. Wang, S. Liao and Y. Liu, "Dynamic crushing of cellular materials: A unified framework of plastic shock wave models," *Int. J. of Impact Engrg*, vol. 53, pp. 29-43, 2013.
- [14] P. Tan, J. Harrigan and S. Reid, "Inertia effects in uniaxial dynamic compression of a closed cell aluminium alloy foam," in *Materials Science and Technology Vol 18*, 2002, pp. 480-488.
- [15] Y. Chen, H. Chen and B. Shen, "Depth of penetration prediction for closed-cell aluminium foam experiencing impact of different shape projectiles," *Journal of the Chinese Institute of Engineers*, vol. 36, no. 7, pp. 856-869, 2013.
- [16] Q. Li, I. Magkiriadis and J. Harrigan, "Compressive strain at the onset of densification of cellular solids," *Journal of Cellular Plastics*, vol. 42, pp. 371-392, 2006.

- [17] M. Avalle, G. Belingardi and R. Montanini, "Characterisation of polymeric structural foams under compressive impact loading by means of energy-absorption diagram," *Int. J. of Impact Engrg*, vol. 25, pp. 455-472, 2001.
- [18] S. Jones and W. Rule, "On the optimal nose geometry for a rigid penetrator, including the effects of pressure-dependent friction," *Int. J. of Impact Engineering*, vol. 24, pp. 403-415, 2000.
- [19] X. Chen and Q. Li, "Deep penetration of a non-deformable projectile with different geometrical characteristics," *Int. J. of Impact Engrg*, vol. 27, pp. 619-637, 2002.
- [20] J. Van Doormaal, A. Dorr and F. R, "Debris Launch Velocity Program DLV," in 11th International Symposium on the Interaction of the Effects of Munitions with Structures, 2003.
- [21] A. Slobbe and J. Weerheijm, "Numerical Simulations of the Reinforced Concrete Kasun Structure under Internal Blast and Fragment Loading," TNO Draft Report, 2016.
- [22] S. Arezoo, V. Tagarielli and N. Petrinic, "The mechanical response of Rohacell foams at different length scales," *J Master Sci*, pp. 6863 6870, 2011.
- [23] D. Zenkert and M. Burman, "Tension, Compression and Shear Fatigue of a Closed Cell Foam," in *16th International Conference on Composite Materials*.
- [24] Z. Zheng, J. Yu and J. Li, "Dynamic crushing of 2D cellular structures: A finite element study," *Int. J. of Impact Engrg*, vol. 32, pp. 650-664, 2005.
- [25] Z. Zheng and Y. J, "Dynamic crushing of 2D cellular metals: microstructure effects and rate-sensitivity mechanisms," *Acta Mechanica Soilda Sinica*, December 2010.
- [26] Y. Sun, Q. Li, S. McDonald and P. Withers, "Determination of the constitutive relation and critical condition for the shock compression of cellular solids," in *Mechanics of Materials*, Elsevier Ltd., 2016, pp. 26-36.
- [27] Q. Li and E. Flores-Johnson, "Indentation into polymeric foams," *Int. J. of Soilds and Structures*, vol. 47, pp. 1987-1995, 2010.
- [28] LS-DYNA Keyword User's Manual Volume 1 LS-DYNA R8.0, Livermore Software Technology Corporation (LSTC).
- [29] LS-DYNA Keyword User's Manual Volume 2 Material Models LS-DYNA R8.0, Livermore Software Technology Corporation (LSTC).
- [30] "LS-DYNA Support," LSTC, [Online]. Available: http://www.dynasupport.com/.